INL/EXT-06-11832

Measurement and Modeling of Sorption-Induced Strain and Permeability Changes in Coal

Eric P. Robertson

October 2005

The INL is a U.S. Department of Energy National Laboratory
operated by Battelle Energy Alliance

INL/EXT-06-11832

Measurement and Modeling of Sorption-Induced Strain and Permeability Changes in Coal

Eric P. Robertson

October 2005

Idaho National Laboratory
Idaho Falls, Idaho 83415

Prepared for the
U.S. Department of Energy
Through the INL LDRD Program
Under DOE Idaho Operations Office
Contract DE-AC07-05ID14517

A thesis submitted to the Faculty and Board of Trustees of the Colorado School of Mines in partial fulfillment of the requirements for the degree of Doctor of Philosophy (Petroleum Engineering).

Golden, Colorado
Date: October 26, 2005

Signed: _____
Eric P. Robertson

Approved: _____
Dr. Richard L. Christiansen
Thesis Advisor

Golden, Colorado
Date: October 31, 2005

_____
Dr. Craig W. Van Kirk
Professor and Head
Department of Petroleum Engineering

ABSTRACT

Strain caused by the adsorption of gases was measured in samples of subbituminous coal from the Powder River basin of Wyoming, U.S.A., and high-volatile bituminous coal from the Uinta-Piceance basin of Utah, U.S.A. using a newly developed strain measurement apparatus. The apparatus can be used to measure strain on multiple small coal samples based on the optical detection of the longitudinal strain. The swelling and shrinkage (strain) in the coal samples resulting from the adsorption of carbon dioxide, nitrogen, methane, helium, and a mixture of gases was measured. Sorption-induced strain processes were shown to be reversible and easily modeled with a Langmuir-type equation. Extended Langmuir theory was applied to satisfactorily model strain caused by the adsorption of gas mixtures using the pure gas Langmuir strain constants. The amount of time required to obtain accurate strain data was greatly reduced compared to other strain measurement methods.

Sorption-induced changes in permeability were also measured as a function of pressure. Cleat compressibility was found to be variable, not constant. Calculated variable cleat-compressibility constants were found to correlate well with previously published data for other coals. During permeability tests, sorption-induced matrix shrinkage was clearly demonstrated by higher permeability values at lower pore pressures while holding overburden pressure constant. Measured permeability data were modeled using three different permeability models from the open literature that take into account sorption-induced matrix strain. All three models poorly matched the measured permeability data because they overestimated the impact of measured sorption-induced strain on permeability. However, by applying an experimentally derived expression to the measured strain data that accounts for the confining overburden pressure, pore pressure, coal type, and gas type, the permeability models were significantly improved.

TABLE OF CONTENTS

LIST OF FIGURES

LIST OF TABLES

ACKNOWLEDGMENTS

I would like to express my sincere appreciation to Dr. Richard Christiansen, my academic advisor, for his friendship, kindness, encouragement, and intelligent direction throughout this work.

I would also like to thank the members of my thesis committee: Dr. John Fanchi, Petroleum Engineering; Dr. Rod Eggert, Economics and Business; Dr. Mike Batzle, Geophysics; and Dr. John Curtis, Geology and Geological Engineering for their helpfulness and support.

A large portion of my time while working on this research was funded by the Idaho National Laboratory (INL) through the Laboratory Directed Research Development program and I would like to acknowledge that without that support, I never could have undertaken the effort. I wish to express appreciation to Bruce Reynolds and Greg Stormberg, who were my immediate managers at INL, for their support and encouragement to continue my education.

I also express gratitude to Mike Glasson of Andalex Resources and Greg Gannon of Kennecott for help in the collection of the coal samples.

CHAPTER 1. INTRODUCTION

Coal beds in the United States (U.S.) contain an estimated 703 trillion standard cubic feet (Tcf) of natural gas and 141 Tcf of recoverable natural gas resources, or 12% of the total recoverable natural gas in the U.S. [1], making coal beds a major contributor to the energy security of the U.S. Besides being highly productive natural gas reservoirs, coal beds throughout the world have a huge potential to store carbon dioxide (CO_2). If coal seams were viewed purely as potential CO_2 sinks and not tied to commercial production of methane, the worldwide CO_2 sequestration potential in unmineable coal may be 380 billion tons of CO_2 [2]. For comparison, a typical, modern coal-fired power plant producing 300 megawatts (MW) of electricity would output roughly 1.3 million tons of CO_2 per year [3].

Unlike conventional gas reservoirs, methane in coal is not stored as free gas but rather as adsorbed gas, at near-liquid densities on the internal surface area of the microporous coal [4], which can range from 30 m^2/g to 300 m^2/g [5, 6]. Besides methane, other gases are present in coal; carbon dioxide, nitrogen (N_2), and higher molecular weight hydrocarbon gases (C_2^+) are usually present. The coal gas in the San Juan Basin can contain up to 10% CO_2 and 13% C_2^+ [7]. In the Powder River Basin, adsorbed gas composition is typically about 90% methane (CH_4), 8% CO_2, and 2% nitrogen [8].

1.1 Fluid Flow through Coal

As reservoir pressure is lowered during coalbed methane (CBM) production operations, gas molecules are desorbed from the coal's internal surfaces and travel through the matrix to the cleat (natural fracture) system where they are conveyed to producing wells. Figure 1.1 is a diagram showing the movement of gas molecules through the matrix to the

fracture system. Because matrix permeability is typically eight orders of magnitude lower than the permeability of the cleat system [9], fluid movement in the coal matrix is best modeled by Fick's Law of diffusion and flow through the fracture system is described by Darcy's Law. Coal seams are, therefore, treated as fractured reservoirs with respect to fluid flow and permeability of the matrix blocks is neglected.

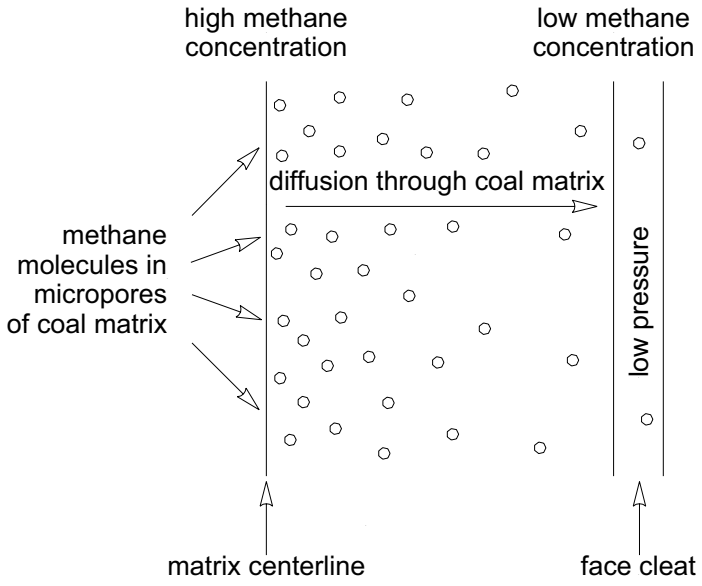

Figure 1.1. Diagram showing the movement of gas molecules through matrix of coal block towards cleat system.

In most coalbed methane (CBM) reservoirs, the cleat system is initially filled with water. Producing water from the cleats causes the reservoir pressure to decrease and causes the gas to desorb from the coal matrix at the matrix-cleat interfaces. This creates a methane concentration gradient across the coal matrix causing the gas to diffuse through the matrix and then to be released into the cleat system where it flows to the production well.

1.2 Gas Storage in Coal

The capacity of the coal matrix to store gas as a function of pressure is described by the Langmuir adsorption isotherm [10, 11]:

$$V = \frac{V_L p}{p_L + p} \quad \text{..... (1-1)}$$

where V is the volume of gas adsorbed per unit mass in the coal matrix and p is the pressure of the system. V_L is the Langmuir volume constant and represents the maximum volume of gas per unit mass a coal can adsorb onto the matrix surface area. The Langmuir pressure constant, p_L, is the pressure at which the storage capacity of the coal is equal to one-half the Langmuir volume V_L. The constants in the Langmuir adsorption isotherm equation are determined by fitting desorption data obtained in the laboratory and are specific for any given coal and gas ensemble. Figure 1.2 shows a typical methane sorption isotherm for coal from the San Juan Basin [4].

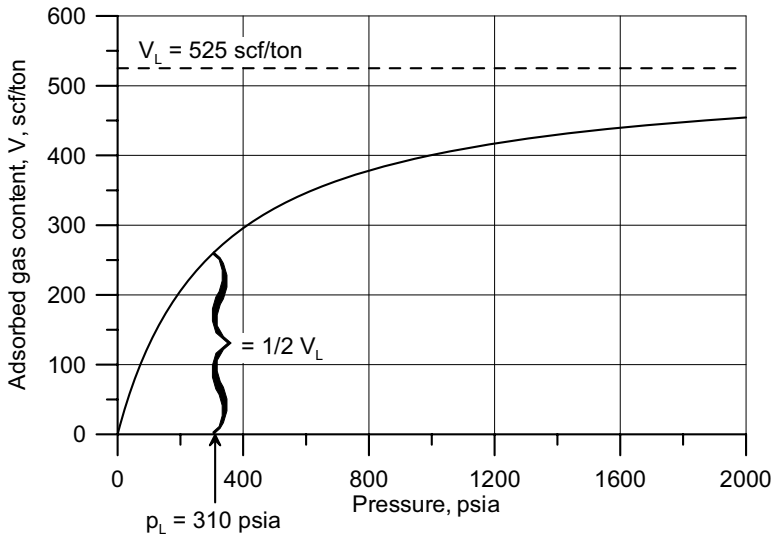

Figure 1.2. Example of an adsorbed gas isotherm showing relationship of fit parameters V_L and p_L from Eq. (1-1).

1.3 Gas Production from Coal Beds

Methane production from coal beds can be enhanced by injecting other gases to displace or strip the methane from the coal and accelerate production of methane without lowering reservoir pressure. This process is called enhanced coalbed methane (ECBM) production. About twice the amount of CO_2 can be adsorbed in the microporosity of the coal matrix as CH_4, while N_2 is less adsorbing than CH_4. Figure 1.3 compares sorption isotherms for CO_2, CH_4, and N_2 as a function of pressure for a sample San Juan Basin coal [12]. The mechanism of N_2-ECBM is called inert gas stripping and is primarily the result of reducing the partial pressure of CH_4 in the cleat system. As N_2 is injected, the partial pressure of CH_4 is reduced and methane is desorbed from the coal even at high total cleat pressure [4], which can greatly accelerate the recovery of the methane from the coal bed and reduce after-wellhead compression costs [13].

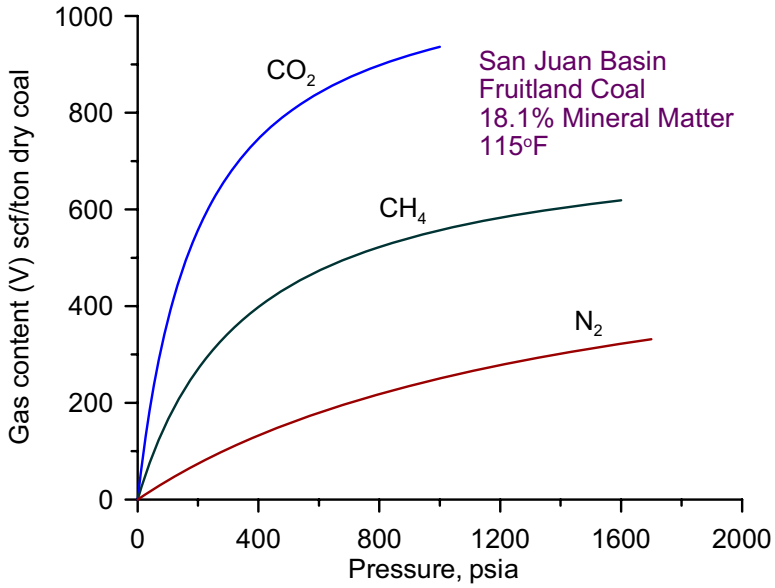

Figure 1.3. Example of sorption isotherms for different gases.

The mechanism for CO_2-ECBM is called displacement desorption because the CO_2 is strongly adsorbed onto the coal as it is injected and displaces the methane in the matrix. If the coal seam is relatively homogeneous and the diffusion rate into the coal matrix is sufficient, CO_2 is not expected to break through to the production wells until the bulk of the coal bed is swept of methane [14]. Because CO_2 is strongly adsorbed onto the coal matrix, coal beds throughout the world have a huge CO_2 storage potential. When viewed as commercial CO_2-ECBM projects, the total worldwide potential for CO_2 sequestration may be 7.8 billion tons while producing 68 Tcf of methane, and if viewed purely as a non-commercial CO_2 sequestration technology, the worldwide potential may be 50 times greater [2].

1.4 Gas Mixtures in Coal Beds

During normal primary recovery of natural gas from coal beds, the gas does not consist of a single pure gas, but is truly a mixture of a number of components. Besides methane, other gases, such as carbon dioxide, nitrogen, and higher molecular weight hydrocarbon gases are also usually naturally present. The coal gas in the San Juan Basin can contain up to 10% CO_2 and 13% C_2^+ [15]. In the Powder River Basin, sorbed gas composition is typically about 90% methane, 8% CO_2, and 2% nitrogen [16]. In fact, in recent years the term coalbed methane (CBM) has begun to be replaced with other more accurate terms such as coalbed natural gas (CBNG) or natural gas from coal (NGC).

Because coal has the capacity to adsorb from 2 to 5 times as much CO_2 as methane [51], coal beds would be an excellent target for CO_2 sequestration, while at the same time enhancing the production of desirable methane. The injection of CO_2 or N_2 to enhance production of natural gas from coal further increases the presence of non-methane gases within the coal bed.

Tiffany project (operated by BP) in the San Juan Basin, Colorado was the first commercial demonstration of enhanced methane recovery by gas injection [17]. The Tiffany

Field project consisted of 38 producer and 10 injector wells. During the enhanced recovery phase of this project (from February 1998 to April 2001), N_2 was injected into the field to accelerate methane recovery. Reservoir simulation efforts for this project found problems associated with the permeability changes during the enhanced production stage [18], which could have resulted from an inadequate model of the strain-permeability relationship.

The Allison Unit CBM project (operated by Burlington Resources) located in San Juan County, New Mexico, in close proximity to the border with Colorado consisted of 16 producing wells, 4 CO_2 injectors, and one pressure observation well [19]. The Unit originally began primary production in 1989, with CO_2 injection beginning in 1995 and ending in August 2001 to evaluate the results. Clear evidence was found of significant coal permeability reduction with CO_2 injection, which compromised the CO_2 injectivity, reduced incremental methane recoveries, and lowered project economics.

Under the direction of the Alberta Research Council micropilot tests of ECBM and CO_2 sequestration were done near the towns of Fenn and Big Valley in Alberta, Canada [20]. Two wells, completed in the Medicine River Coal seams were used to study how CO_2 and mixtures of CO_2/N_2 reacted during injection, soak, and production phases. Among other things, they found that their permeability model for the injection phase was deficient in predicting permeability changes that actually took place.

1.5 Stress-Dependent Permeability in Coal

Cleats are generally regarded as having a uniform geometry representative of the coal as a whole. The cleat system consists of two or more sets of sub-parallel fractures oriented nearly perpendicular to the bedding plane [21]. Face cleats are more dominant, while butt cleats, generally oriented perpendicular to face cleats, are less dominant, and connect face cleats. Although it treats face and butt cleats equally, matchstick-type ge-

ometry (see Figure 1.4) is often chosen as an appropriate analogy to model the cleat system [22].

Cleat permeability is directly dependent on the width of the cleats and the cleat frequency. Cleat frequency is generally assumed to be constant, but cleat width is dependent on the in situ stress, the coal properties, and the gas content of the coal. The in situ stress is equivalent to the net pressure in the coal seam and is equal to the overburden pressure minus the fluid pressure in the cleat system (horizontal stresses are expected to be negligible in the field [23]).

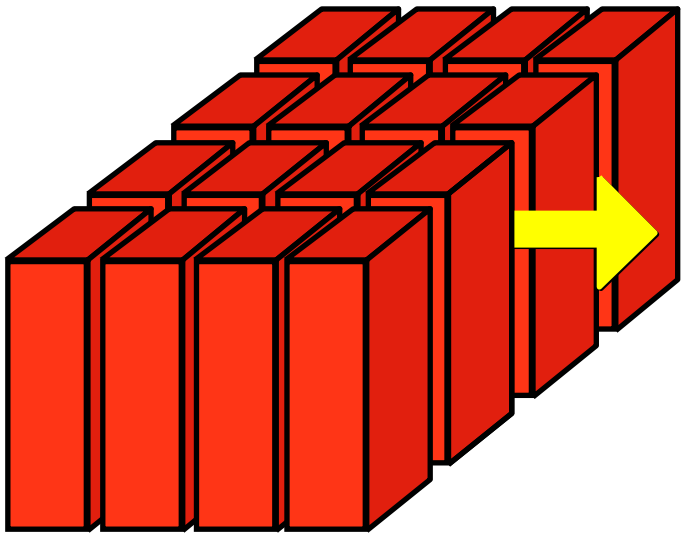

Figure 1.4. Depiction of flow through matchstick-type fractured media.

During CBM production operations, overburden pressure at a given depth remains constant, but as the cleat pressure decreases due to the production of water and gas, the cleat width will decrease depending on the elastic moduli of the coal matrix. These moduli (Young's modulus, bulk modulus, Poisson's ratio, and constrained axial modulus) can be used to calculate the cleat compressibility of any fractured media [24] – including

coal. Coal, however, has another property that contributes to a change in cleat width as pressure is drawn down that most other fractured media do not have – it contains adsorbed gas that is released as pressure is lowered (see Figure 1.2). As this gas is desorbed from the coal, the matrix blocks shrink, which increases the cleat width as well as permeability. The matrix shrinkage (volumetric strain) due to the release of the adsorbed gas can be modeled with a curve analogous to the adsorbed gas isotherm [25]. The model used to fit the sorption-induced strain data is called the Langmuir strain curve.

Figure 1.5 shows an example of the combined effects of the coal's elastic moduli and the matrix shrinkage on the change in permeability of coal as pressure is drawn down. When pressure in the cleat system is high, the associated sorption-induced strain accompanying a change in pressure is relatively small and the dominant strain acting on the coal is matrix expansion due to the elastic properties of the coal; accordingly, the cleat width would decrease as would permeability. However, as the total pressure continues to drop and the cleat pressure becomes small, the associated sorption-induced strain accompanying a change in pressure can be relatively large and the dominant strain acting on the coal is matrix shrinkage due to the gas desorption, causing cleat width to increase along with permeability.

1.6 Objectives of Research

The first objective of this research is to measure sorption-induced strain in coal not only for pure gases, but for gas mixtures as well. The second objective is to measure permeability of coal for pure gases and mixtures. The final objective is to assess the performance of models for calculating permeability as a function of sorption-induced strain for pure gases and mixtures.

This thesis will discuss the development of a new strain measurement apparatus that greatly reduces the time required to obtain sorption-induced strain data in coal. New strain data induced by the sorption of three pure gases and a gas mixture will be presented

for two coals of different ranks. The strain induced by the sorption of the gas mixture will be modeled using extended Langmuir theory based on the strain curves induced by the sorption of the pure gas components of the mixture.

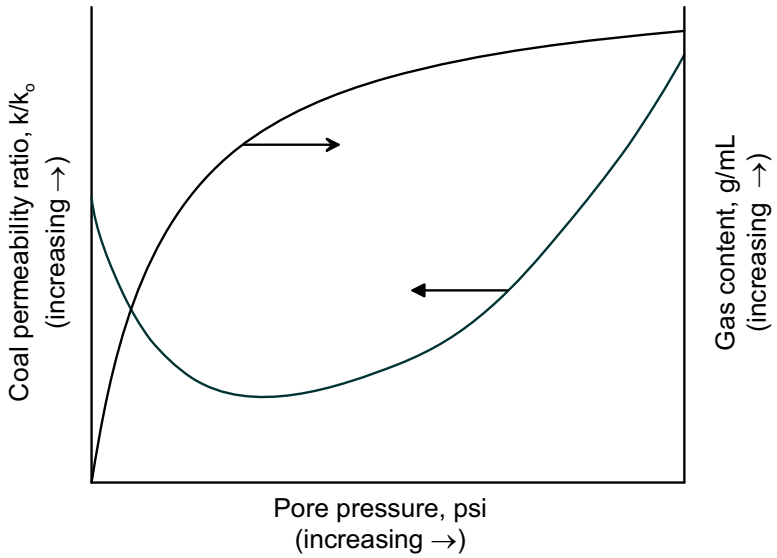

Figure 1.5. Conceptualized behavior of permeability rebound in coal and gas desorption curve as pressure becomes small.

The effect of sorption-induced strain on coal permeability will be presented. Permeability will be measured as different gases are sorbed using automated data-collection software. The methodology for core preparation, data manipulation, and experimentation will also be discussed.

Selected permeability models based on Langmuir strain curve data will be used to model laboratory permeability data. The models will also be expanded to account for the sorption of mixed gases by incorporating extended Langmuir theory into the permeability equations. It is anticipated that if strain parameters associated with mixed-gas adsorption were incorporated into these equations, field permeability changes could be better mod-

eled. The resulting expanded permeability models could be incorporated into reservoir simulators to better predict permeability decline and rebound during traditional CBM production operations. However, results of this research may be even more applicable during simulation of N_2- or CO_2-enhanced methane recovery from coal beds, as well as for CO_2-sequestration in coal beds.

CHAPTER 2. LITERATURE REVIEW

In this chapter, previous work done by other researchers will be reviewed leading up to the current work reported in this thesis. Specifically, the methodology, equipment used, and drawbacks of sorption-induced coal strain will be reviewed along with past efforts to model permeability changes in coal induced by sorption of gases.

2.1 A Review of Previous Measurement of Strain Isotherms in Coal

Measurement of sorption-induced strain was an integral part of this research. Strain data were to be collected using pure and mixed gases and at least two different coals. The pure gas strain data were to be used to predict the strain behavior of the coals under mixed gas conditions. A methodology to measure strain was needed and a review of the literature found that there were some drawbacks to the most common method of obtaining this data. This section describes the most common method for collecting strain data and suggests improvements that could be made.

The measurement of sorption-induced strain in coal has been reported by relatively few researchers. Gray [26] reported that strain varied linearly with gas pressure for both CO_2 and CH_4, but did not include any details about how those values were obtained. Harpalani and Schraufnagel [27] showed that sorption-induced coal strain was not necessarily a linear function of gas pressure, but might be non-linear with decreasing gas pressure. They were also among the first researchers to relate sorption-induced strain in coals to permeability changes during the production of methane from coal seams. Using a procedure suggested by the International Society of Rock Mechanics, they attached strain gauges to the surfaces of a cylindrical coal specimen – one each for axial and radial strains, 180° apart. The coal specimen, measuring one and one-half inches in diameter

and three inches in length, was then placed into a pressure cell. The strain gauges were connected to the strain indicators outside the cell by passing the connecting wires through O-rings used to seal the pressure cell. Other researchers have used this same basic experimental design and employed strain gauges attached to blocks of coal of the same relative size to study sorption-induced coal strain [28, 29, 30]. Figure 2.1 is a drawing of a coal sample with typical dimensions showing the configuration of attached strain gauges used to measure sorption-induced strain.

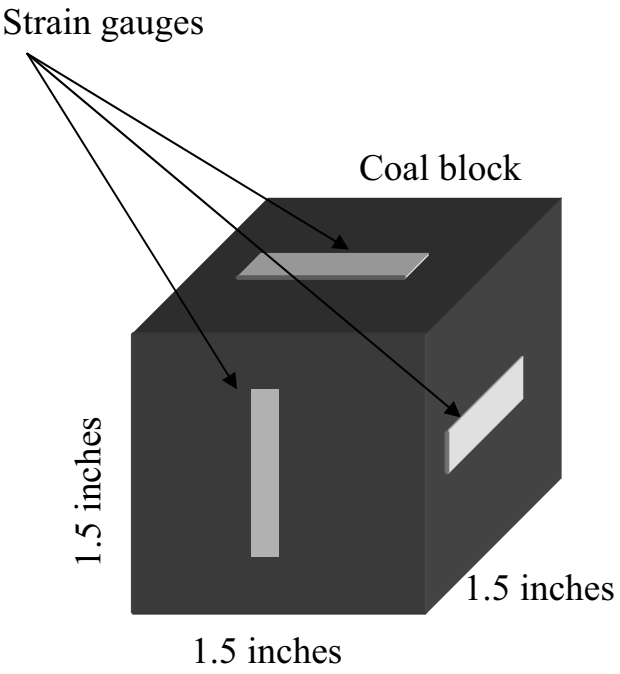

Figure 2.1. Drawing of typical dimensions of coal block used with strain gauges to measure sorption-induced strain.

Typical sorption-induced strain experiments are done in two phases: adsorption, where strain is measured as gas pressure is increased; and desorption, where strain is measured as gas pressure is decreased. In these experiments, the initial gas pressure sur-

rounding the coal samples is typically set at a low pressure or under vacuum and the initial strain gauge readings are noted indicating zero strain. Next, a specified gas is introduced and held at a given pressure while the strain readings are monitored. When the strain becomes constant at that pressure, the strain is noted and the gas pressure is then increased to the next desired value. This process is repeated until some maximum pressure is reached over a period of five or six pressure steps. During desorption, pressure can either be stepped down, or it can be released all in one step.

There have been a number of problems associated with obtaining sorption-induced strain data using attached strain gauges. These problems are discussed in the following paragraphs.

Levine [29] noted that there were "few reliable measurements available for strains caused by gas sorption/desorption in coal. The lack of data is due to the difficulty of making these measurements and too few such studies have been conducted. Much more data are needed to document this phenomenon." Permeability models for coal beds require the use of sorption-induced strain data. Accurate and rapid generation of strain data is necessary if permeability models are to be correctly formulated and applied to different fields.

Harpalani and Schraufnagel [27] noted that "desorption [was] an extremely slow process and it took a long time for the readings on the strain indicator to stabilize." The slow process of strain stabilization is presumably due to the slow diffusion rate coupled with the size of the samples. The samples are necessarily no less than three cubic inches in order to accommodate the adhesion of the strain gauges. Seidle and Huitt [28] also measured coal strain using strain gauges glued to coal samples and reported that it took nearly three months for the coal matrix strains to stabilize during the adsorption phase at each pressure step. Zutshi and Harpalani [31] report equilibration times of over 75 days during the gas adsorption phase.

Conservatively assuming that if 50 days were required for strain equilibration at each pressure step and that five pressure steps were planned for the adsorption phase and five

more for the desorption phase, the entire experiment for one sample of coal could take over 16 months to complete! In addition, any measurement errors caused by insufficient time allowed for strain equilibration would yield strain measurements lower than reality. Of course, smaller samples should require shorter equilibration times, owing to the shorter diffusion pathways, but sample size is limited by the dimensions required by the strain gauges.

Harpalani and Schraufnagel [27] reported a hysteresis between increasing and decreasing gas pressures, which could be explained by possible errors in their strain measurements caused either by insufficient equilibration time or by abnormal deformation of the strain gauges themselves. Seidle and Huitt [28] found that the most challenging part of their strain experiments was getting the glue to adhere to the coal for the very long times required for completion of the strain tests. They also noted that the strain gauges experienced some irreversible strain at the end of each leg of their experiments, which complicated the analyses.

Chikatamarla and Bustin [30] also recently reported strain measurements using strain gauges and although they do not mention the amount of time needed for equilibration, they did report problems with gas reacting with the strain gauges forcing an early termination of some experiments.

Table 2.1 summarizes some coal strain data collected using resistance-type strain gauges as reported by previous researchers. The strain reported in this table is not all directly comparable because different gases were used and different pressures were reported. However, these data do show that sorption-induced strain is generally higher for carbon dioxide than for methane and that strains measured with strain gauges are about 1.0% for carbon dioxide and about 0.3% for methane. A discussion of longitudinal strain and volumetric strain appears in Section 4.2.5 later in this work; but briefly, longitudinal strain is generally ⅓ the value of volumetric strain.

Table 2.1. Coal strain values as reported by previous researchers.

Author	Sorbed gas	Strain		Pressure, psi
		Type of strain	Value	
Gray, 1987	CO_2	Longitudinal	1.0%	800
	CH_4	Longitudinal	0.06%	800
Harpalani and Schraufnagel, 1990	CH_4	Volumetric	0.6%	1000
Seidle and Huitt, 1995	CO_2	Longitudinal	0.8%	800
	CH_4	Longitudinal	0.1%	1000
Levine, 1996	CO_2	Longitudinal	0.5%	750
	CH_4	Longitudinal	0.2%	1000
Zutshi and Harpalani, 2004	CO_2	Volumetric	1.1%	750
	CH_4	Volumetric	0.5%	1000
Chikatamarla and Bustin, 2004	CO_2	Volumetric	2.41%	800
	CH_4	Volumetric	0.49%	1000

Most of the sorption-induced strain data for coals has been for pure gases as noted previously. Massaratto [32] identified a need for mixed-gas strain isotherms because of the rather large difference between the CO_2 and the CH_4 strain isotherms. Law [33] argued that during primary CBM production, matrix shrinkage might be adequately modeled using pure gas (methane) strain measurements; however, during ECBM CO_2-sequestration activities, mixed-gas strain isotherms would become essential in order to adequately model permeability changes. Even though there is a need for mixed-gas strain isotherm, these measurements have not been found in the open literature.

Measuring sorption-induced coal strain using strain gauges could be very time consuming, fraught with equipment malfunctions, and result in difficult-to-interpret data. Therefore, it was thought that a more rapid method, not reliant on the use of strain gauges, was needed to meet the needs of this research and to generate data for future projects. In light of the rapid development of coalbed methane plays in the U.S. and the

world, and the potential for CO_2 storage in unmineable coal seams, there appears to be a need for more sorption-induced strain for use in reservoir simulators. Relatively few pure-gas strain isotherms and no mixed-gas strain isotherms have been reported in the open literature perhaps because of the difficulties associated with resistance-type strain gauges and the length of time required for equilibration of the samples.

2.2 A Review of Previous Coal Permeability Modeling Efforts

Knowledge of how the adsorption or desorption of gases affects coal permeability is important not only to operations involving the production of natural gas from coal beds, but is also important to the design and operation of projects to sequester greenhouse gases in coal beds [34].

Sorption-induced strain of the coal matrix causes a change in the width of the cleats or fractures that must be accounted for when modeling permeability changes in the system. A number of permeability-change models for coal have been proposed that attempt to account for the effect of sorption-induced strain. In 1987, Gray [26] explained that permeability fluctuations in coal beds during pressure depletion production were not solely a relative permeability effect, but rather a result of the opposing effects of effective stress increase with fluid pressure reduction and shrinkage of the coal due to gas desorption. His model assumes that strain isotherms are linear with respect to pressure; however, sorption-induced strain can be better modeled using a Langmuir-type equation instead of a linear relationship as discussed previously and shown later in this current work.

The permeability model described by Sawyer et al. [35] in 1990 assumed that strain was proportional to gas adsorption. The proportionality constant that equates the strain and adsorption isotherms, however, was left undefined and was used to calibrate the permeability equation by matching measured data. The Pekot and Reeves model [36] used in the commercial CBM reservoir simulator, COMET, is based on the Sawyer et al. model.

In 1995, Seidle and Huitt [28] presented a permeability model designed to demonstrate the potential for drastic permeability increases due to gas desorption. Their model ascribed all matrix strain to gas desorption and neglected the matrix compressibility based on the elastic properties of the coal. This model, therefore, is limited to specific conditions where sorption-induced strain dwarfs the effect of the elastic properties of the coal with changes in pressure.

In 1998, Palmer and Mansoori [23] published a permeability model incorporating the combined effect of coal's elastic properties and gas sorption on the matrix strain. The Palmer-Mansoori theory of permeability changes during CBM production includes a permeability loss term (due to an increase in effective stress), and a permeability gain term due to matrix shrinkage as gas desorbs from the coal This model has been the basis of other models such as that presented by Chikatamarla and Bustin [30] in 2004. However, some concerns have been raised regarding the broad applicability of this model in that field permeability cannot always be matched without neglecting the permeability loss term associated with an increase in effective stress [37, 38].

Shi and Durucan [39] presented yet another coal permeability model in 2003, which included both stress-dependent permeability and matrix shrinkage terms. They were able to match field data [40] and obtained initial porosities generally similar to those obtained using the Palmer-Mansoori model [37]. In addition, they found that if initial reservoir pressure is high enough, a theoretical permeability rebound should occur, but if it is not high enough, a permeability rebound might not occur, just an increase of permeability with depletion right from the start.

The phenomenon of increasing permeability as pressure becomes small, which can only be caused by sorption-induced strain, has been clearly demonstrated in the field [37], but efforts to adequately match field results using coal permeability models have been largely unsuccessful without large changes to measured parameters [23]. In the field, the produced gas is typically a mix of CH_4, CO_2, N_2, and lesser quantities of heavier hydrocarbons; and the adsorbed gas typically has a higher content of the heavier

molecules such as CO_2 and C_2^+. Although models for coal permeability changes induced by pure gas adsorption have been presented as discussed earlier, the applicability of these models to mixed-gas systems is unknown.

CHAPTER 3. COAL DESCRIPTION, COLLECTION, HANDLING, AND STORAGE

Because most coals are sensitive to oxidation and because exposure of freshly mined coal to air at ambient temperatures for as little as a few days can adversely affect some properties such as heating value and tar yield [41, 42], care was exercised during the collection of the coal to limit exposure to air and to ensure that the samples remained as pristine as possible. A short description of the coal is provided in this chapter along with a narrative of how it was collected and stored until used.

3.1 Coal Description

High-volatile bituminous coal from the Uinta-Piceance basin was collected from the Aberdeen seam, the Gilson seam, and the lower Sunnyside seam of the Book Cliffs coal field from underground mines near Price, Utah. Additionally, subbituminous coal from the Powder River basin was collected from the Anderson and Canyon seams from an open pit coal mine near Gillette, Wyoming. At the Wyoming mine location, the Anderson and Canyon seams were each over 100 ft thick and there was about 150 feet of rock separating these coal seams. Proximate, ultimate, and heating value analyses were subsequently done on samples of the collected coal and are shown in Table 3.1. Values obtained from the open literature for both the Wyoming coal [43] and the Utah coal [44] are also shown in Table 3.1 for comparison. Additional coal information can be found in an Argonne National Laboratory study [45] using a Utah coal collected from a mine adjacent to the coal used in this study.

Table 3.1. Properties of coal samples collected and used in this research as ascertained from various analyses on an "as received" basis.

	Powder River basin, subbituminous		Uinta-Piceance basin, high-volatile bituminous		
	Anderson	Canyon	Gilson	Sunnyside	Aberdeen
Proximate Analysis wt%:					
Moisture	26.60	20.36	7.52	4.61	3.71
Ash	6.18	24.50	2.99	19.30	3.38
Volatile Matter	30.99	24.46	37.42	31.14	41.49
Fixed Carbon	36.23	30.68	52.07	44.95	51.42
Total	100.00	100.00	100.00	100.00	100.00
Ultimate Analysis wt%:					
Moisture	26.60	20.36	7.52	4.61	3.71
Hydrogen	2.08	1.83	3.86	3.68	4.56
Carbon	50.57	41.96	71.66	62.38	75.74
Nitrogen	0.43	0.34	1.36	0.80	1.60
Sulfur	0.27	0.54	0.49	1.37	0.59
Oxygen	13.87	10.47	12.12	7.86	10.42
Ash	6.18	24.50	2.99	19.30	3.38
Total	100.00	100.00	100.00	100.00	100.00
Heating Value, Btu/lb					
Measured	8,514	6,939	12,437	10,788	13,685
Literature values	8,220 [43]	—	12,000 [44]	—	12,300 [44]
Vitrinite Reflectance	0.24	0.28	0.53	0.62	0.54

3.2 Coal Collection and Sample Storage

Coal samples of about one cubic foot in size were collected from the coal seams listed in Table 3.1. The Utah coal samples were taken from the conveyer belt carrying recently mined coal out of the underground mine within one-half minute of first exposure to limit degradation of the sample by oxygen. Immediately after being taken from the conveyer, each sample was double wrapped in plastic bags and sealed by tape. Transporting the sample from the mine face to the surface took from 5 to 20 minutes depending on the collection site. Upon reaching the surface, the samples were removed from the bags and placed under de-ionized (DI) water inside containers for transport back to Idaho National Laboratory (INL) in Idaho Falls, Idaho. One coal sample was taken from the Aberdeen mine (Aberdeen seam), one from the Centennial mine (Gilson seam), and two from the West Ridge mine (Sunnyside seam). Figure 3.1 is a photograph of one of the coal blocks collected from the Sunnyside seam that was not used in the experimentation. The Wyoming coal was collected from an open pit mine from mine walls exposed earlier in the day. Large boulders several feet in diameter were broken open to expose fresh coal inside. Samples of roughly one cubic foot were then taken from this fresh area and immediately placed under water in sealed containers for transport to INL where they were either cut and drilled or stored in sealed containers under DI water.

Figure 3.1. Photograph of the block of coal collected from the Sunnyside seam.

CHAPTER 4. DEVELOPMENT OF NEW OPTICAL STRAIN MEASUREMENT APPARATUS

In this chapter, evolution of the apparatus design, test procedures, and development of the optical strain measurement apparatus is described. Direct strain measurement using an optical method was pursued as a possible alternative to the use of strain gauges. It was believed that smaller samples could be used with this type of approach, which would speed up the strain experiments and also eliminate the equipment problems associated with strain gauges.

4.1 Strain Measurement Apparatus – Version 1

The first effort at developing an optical strain measurement apparatus was to use a fine-scale video system connected to a video screen to monitor changes in the length of coal samples placed inside a transparent pressure cell [46]. A pressure cell commonly used as a sight glass[1] for determining fluid levels in high pressure reactors was used in the initial coal strain experiments. The off-the-shelf pressure cell was manufactured with thick glass walls on opposite sides to allow for the direct viewing of the contents inside and to contain pressures of up to 5000 psia.

A long, skinny piece of coal, on the order of ⅛-inch by ⅛-inch by 1-inch, small enough to fit through the pressure cell end ports would be used with this apparatus. A video camera with a high-magnification lens was mounted to a tripod and focused on the coal sample inside the pressure chamber. The magnified image was viewed on a video monitor attached to the video camera.

The pressure cell was inclined to a 45-degree angle to seat the coal sample against the bottom of the cell by gravity to permit the measurement of linear strain from a common reference point as the sample elongated. Figure 4.1 is a photograph of Version 1 of the strain measurement apparatus and shows the pressure cell, the placement of the video camera attached to the tripod, as well as the monitor used to view the video image. In this photograph, the rectangular end of the coal sample can be seen on the left in the image on the monitor.

Figure 4.1. Photograph of Version 1 of the strain apparatus.

---

[1] Model 17T40, Jerguson Gage and Valve Company, 16633 Foltz Industrial Pkwy, Strongsville, OH 44149

4.1.1 Operation of Apparatus – Version 1

A proof-of-principle experiment was designed solely to demonstrate the possibility of measuring sorption-induced coal strain using an optical system. For this experiment, the strain of the coal sample induced by CO_2 adsorption was determined by measuring the travel of the end of the coal sample across the video monitor. Because this experiment was done before the collection of the coal described in the previous section, a small sample of coal was cut from a larger coal block of unknown origin (thought to have come from a mine near Price, Utah) and placed in the pressure cell. The use of a weathered coal of unknown origin was deemed appropriate in this case because the experiment was designed solely as a test of the apparatus and not to obtain any reportable strain data on coal.

After focusing the video image on the end of the sample, the video monitor‘s field of view (screen size) was calibrated to a standard length. Using this calibration value, and knowing the number of pixels across the screen, the length corresponding to each pixel of the monitor was calculated. Then, the growth of the coal sample was calculated by converting the number of pixels the end of the sample moved during the adsorption of carbon dioxide to its change in length.

Figure 4.2 is a close up view of the pressure cell and video camera lens. Inside the pressure cell, the ends of a piece of 1/8-inch stainless steel tubing (left) and a piece of coal (right) can be seen.

4.1.2 Strain Measurements and Problems

Version 1 of the strain measurement apparatus for optically measuring coal strain without strain gauges was a qualified success, but also uncovered some problems that would need to be addressed in subsequent versions of the apparatus. Measured strain was on the order of ½ percent at 770 psig CO_2 and 70° F, which was in line with measure-

ments made by previous researchers using strain gauges (see Table 2.1). Encouragingly, equilibration time using the small coal sample was much less than the equilibration time using the larger samples required for strain gauges; less than 24 hours compared to greater than one month. The problems of long equilibration times, strain gauge hysteresis, and glue failure were eliminated with this new system, but other problems were encountered that had to be fixed in order to use the system reliably, which are described in the following paragraphs.

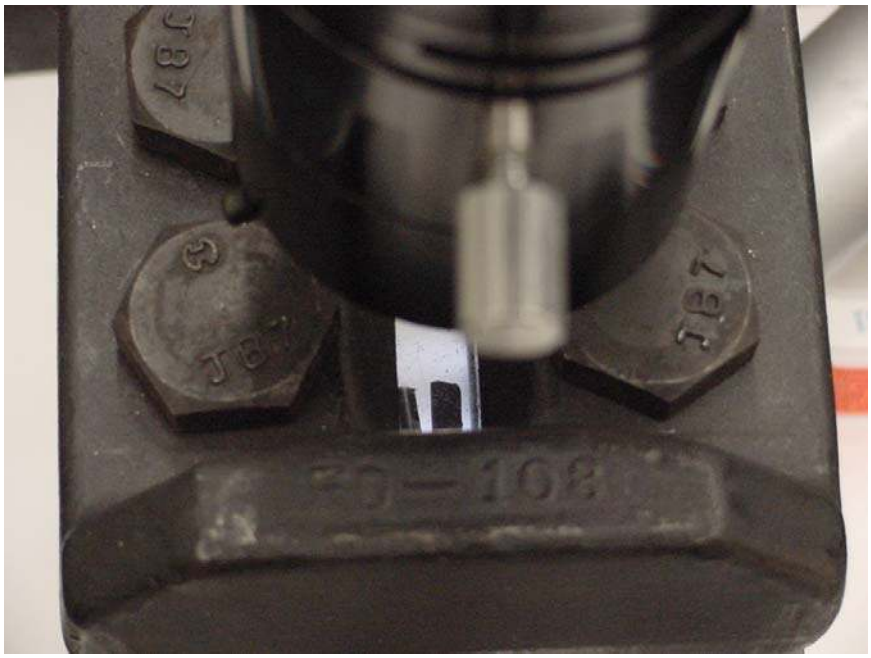

Figure 4.2. Close up view of the pressure cell and video camera lens. Inside the pressure cell can be seen the ends of a piece of 1/8-inch stainless steel tubing (left) and a piece of coal (right).

With the large and heavy lens of the video camera attached to a tripod, fairly severe vibrational problems were encountered. Vibrations caused merely by walking past the station could be seen in the video image, which caused potential errors in the counting of

strain-pixels on the video monitor. However, even though accuracy was somewhat compromised by the vibrations, confidence that sample elongation was on the order of 0.5% was high. Nevertheless, a way to reduce or eliminate these vibrational effects on the video image was needed in order to more accurately measure strain.

The proof-of-principle experiment was done using carbon dioxide (a gas expected to cause a large sorption-induced strain) at high pressure because results using the best-case scenario were desired. Even though the video camera lens was highly magnified, the 0.5% strain (0.127 mm of actual length change) was at the low end of the system's detection capability. During the experiment, the end of the coal sample traveled only 5 pixels. In addition, the end of the coal sample was blurred over two to four pixels, making the determination of the edge difficult. Lower pressure and adsorption of other gases, such as methane or nitrogen, was expected to induce strains potentially much smaller than the 0.5% induced by the adsorption of carbon dioxide. Clearly, the ability to view much smaller changes in coal sample length was needed to compare the effect of different gases at a range of pressures.

Although the pressure cell was large enough to handle multiple samples of coal, Version 1 of the strain measurement apparatus was only able to handle one sample at a time. Being able to measure the strain of multiple samples would allow the generation of enough data to make meaningful comparisons between coals and conclusions about the nature of coal swelling.

4.2 Strain Measurement Apparatus – Version 2

Based upon the problems encountered using the proof-of-principle apparatus, a modified strain measurement apparatus (Version 2) was constructed. The main components of this refined system included a pressure cell of the type used previously, a removable multi-sample holder, and a digital filar microscope mounted directly to the pressure cell. The pressure cell was modified slightly by drilling-out the entrance and exit ports to al-

low for the passage of a ¼-inch rod used to house multiple samples. A multi-sample holder, fabricated out of a solid ¼-inch stainless steel rod, was designed to be easily removable from the pressure cell when samples needed to be changed. A microscope[2] was mounted directly onto the pressure cell to more accurately measure changes in coal strain under different pressures and gas compositions. Mounting the microscope directly to the pressure cell eliminated the vibrational problems encountered with the proof-of-principle apparatus and allowed a much closer and cleaner view of the end of the coal sample.

The rod holding the coal samples was centered in the pressure vessel by passing it through both the inlet and outlet ports of the pressure cell. The test gas could enter and exit the vessel through holes drilled through the center of the rod. A thermocouple to monitor temperature was placed inside the pressure vessel through the gas ports in the rod.

The stainless steel sample holder was designed to hold six samples allowing the measurement of six coal types under identical conditions. The size of the samples was constrained by the dimensions of the sample "beds" machined into the rod. The maximum size is 1-inch in length by 5/32-inch in width by 1/8-inch in height. The sample beds have a solid bottom on which the coal samples rest except for the upper portion, which is machined completely through the rod to allow light to shine up from below and illuminate the coal sample. Figure 4.3 is a photograph of the rod used to house the six samples. This rod, with samples in place, is inserted into the pressure cell for strain measurements.

---

[2] Model M110AE filar microscope with an M224 objective and M330 support rod, Gaertner Scientific Corporation, 3650 Jarvis Avenue, Skokie, Illinois 60076

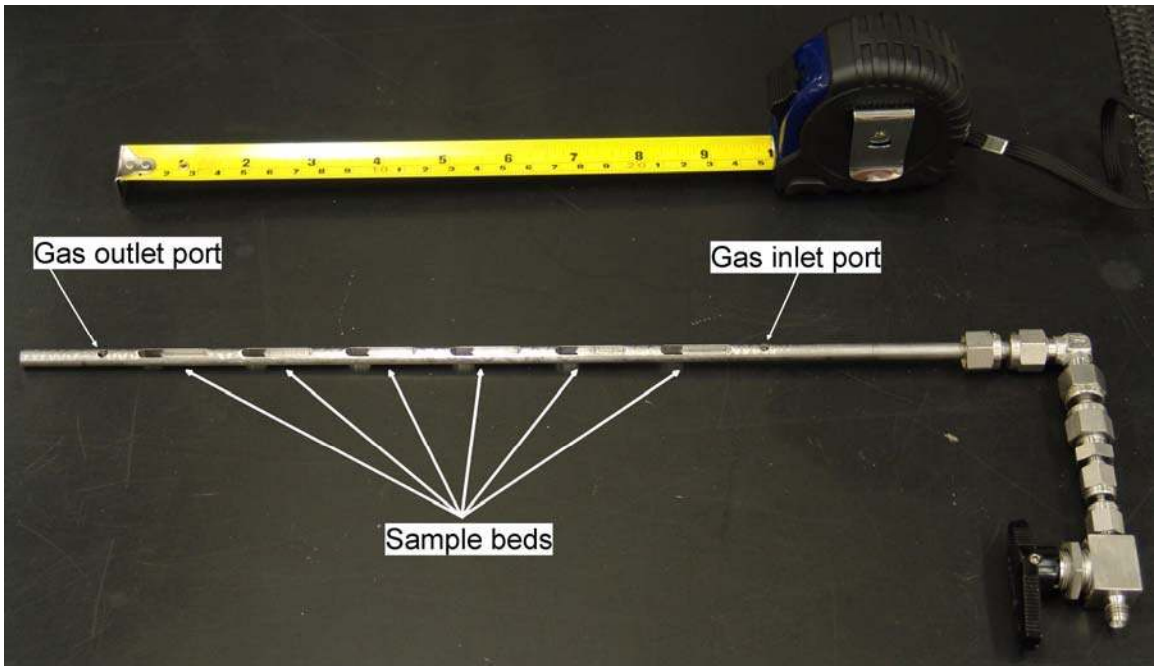

Figure 4.3. Photograph of the stainless steel rod used to house the coal samples.

The microscope currently employed has an attached eye piece that has a movable crosshair attached to a precision rotary encoder that sends the location to a small digital display with a precision of 0.0001 mm. The microscope has a magnification of 2.3X, which gives an object field of 4.8 mm. The coal samples used in these experiments are roughly 20 mm in length, 3 mm in width, and 3 mm in height (¾ in. by ⅛ in. by ⅛ in.). The lower limit of accurate and repeatable measurements of changes in length using the microscope and digital output is 0.001 mm, which translates into a strain of 0.005% for a 20 mm sample, which is two orders of magnitude better than the video camera used in the proof-of-principle apparatus. The upper limit for a growth measurement is 4 mm, yielding a strain of 20% for a 20 mm sample, which is an order of magnitude larger than typical coal strain induced by gas adsorption. Because of the magnification of the microscope, only the ends of the samples can be seen. The apparatus is tilted about 45 degrees

with respect to the horizontal plane so that the coal samples are at rest at one end of the bed. Figure 4.4 shows the components of the filar microscope.

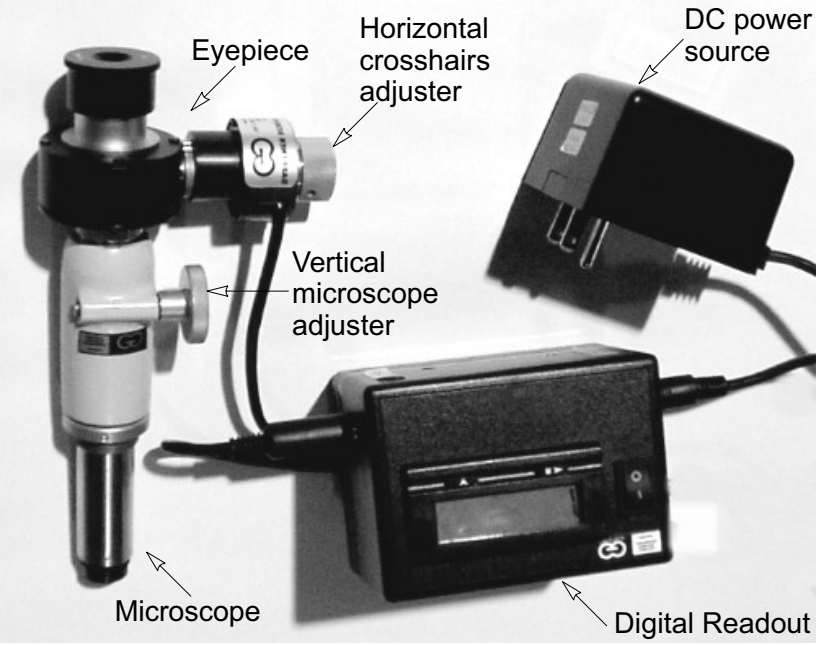

Figure 4.4. Components of the digital filar microscope used for measuring sorption-induced strain in coal.

An adjustable microscope holder was designed and fabricated that allows the entire microscope assembly to be translated along the length of the pressure cell window by turning a hand-adjusted rotating screw. By this means, the microscope can be precisely moved along the entire length of the cell window to view and measure the strain of each of the six samples in the cell during the same experiment.

Figure 4.5 is a photograph of the apparatus developed to measure the longitudinal strain of multiple samples under identical conditions of pressure, temperature, and gas

composition. In the photograph, the microscope attached to the pressure cell and a number of the sample beds can be seen.

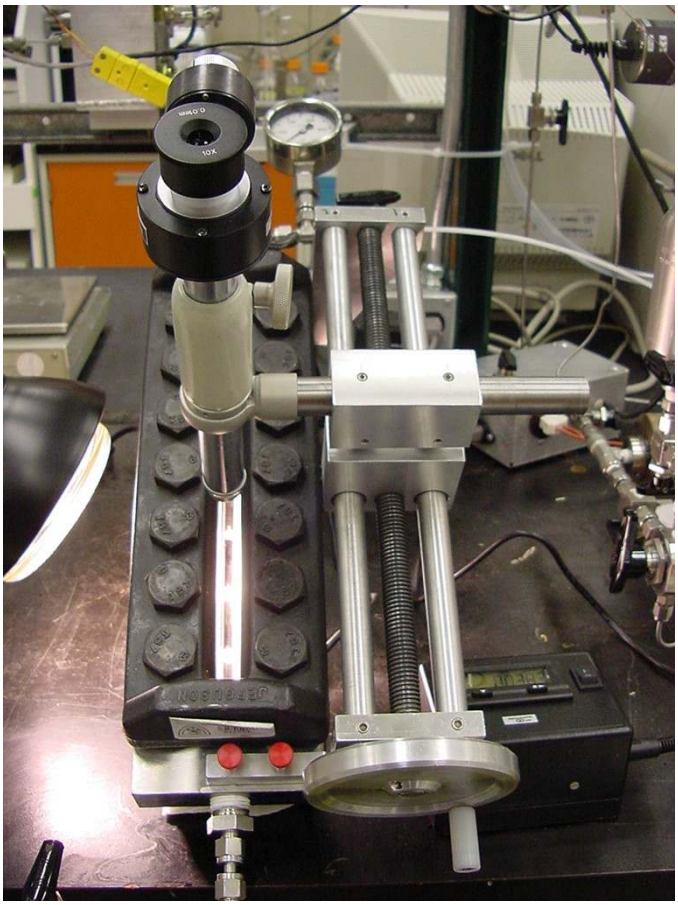

Figure 4.5. Photograph of the apparatus developed to measure the strain of multiple samples without the use of strain gauges.

The measurement of change in length of the samples is accomplished by recording the change in distance between the end of each sample and a specific mark on a clear plastic ruler placed directly on top of the pressure vessel between the microscope and the transparent glass wall of the pressure cell. Figure 4.6 is a photograph of a portion of the

pressure vessel showing the bottom of the microscope, the clear measurement standard, and a few coal samples lying in the sample holder.

Figure 4.6. Photograph of clear measurement standard overlaying the clear glass wall of the pressure vessel. At the top of the figure the bottom of the microscope can be seen; in the center, the sample holder containing coal samples.

4.2.1 Version 2 – Initial Testing

All the coal samples used in the following experiments were cut from a piece of coal taken from the Gilson coal seam. One-eighth-inch thick pieces were cut from a piece of the boulder using a tile saw cooled with DI water and then the small samples used in these experiments were chipped from these pieces to the appropriate size and length. Although every effort was made to minimize atmospheric exposure and to keep the samples moist, the samples may have dried somewhat, and in addition, moisture was not added to the pressure cell during these strain measurements.

A series of swelling experiments using carbon dioxide as the pressurizing medium were conducted to determine response time and swelling properties of coal compared to other porous media and to test the capabilities of this new system.

An experiment was run to compare coal swelling and sandstone swelling (as a control) at room temperature and using carbon dioxide as the adsorbing gas. A coal sample 19.61 mm in length and a Berea sandstone sample 19.97 mm in length were placed in the visual pressure cell in separate sample beds and the air in the cell was displaced by carbon dioxide. The end positions of both samples were recorded while at atmospheric pressure. The carbon dioxide atmosphere was then pressurized to 770 psig. The change in length of both samples was recorded as a function of time, while holding pressure and temperature constant at 770 psig and 73° F respectively. Results of this experiment are shown in Figure 4.7 and show that contrary to expectations, the sandstone sample did elongate somewhat in the presence of pressurized carbon dioxide – on the order of 0.1 percent. However, the coal sample experienced much more strain than the sandstone sample with a strain of over 1.0% under the identical conditions.

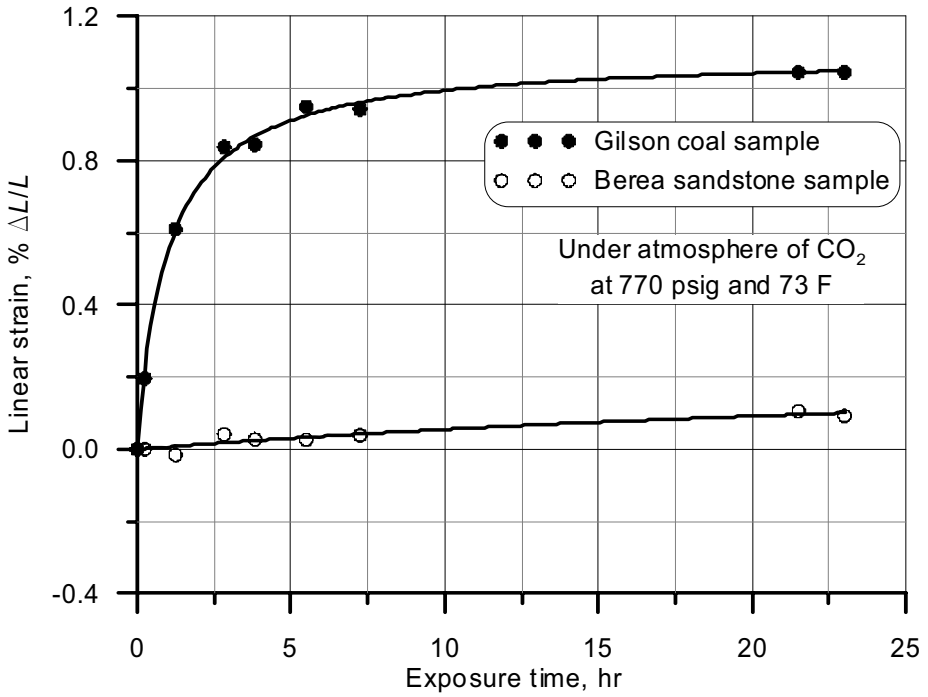

Figure 4.7. Linear strain in Gilson coal sample and Berea sandstone as a function of CO_2-exposure time. The calculated maximum strain for the coal curve is 1.10%.

In a subsequent experiment, multiple samples of coal from the same seam prepared in the same manner as the previous experiment were tested to determine the swelling capacity under the same conditions as above – 770 psig and room temperature. Six different coal samples ranging in length from 19.16 mm to 21.38 mm were placed inside the visual pressure cell and then the air in the cell was replaced by CO_2. The locations of the sample ends before pressurization were noted and then carbon dioxide was admitted into the cell until a pressure of 770 psig was reached at a temperature of 73° F. The change in length of each sample was monitored over the course of a day. Figure 4.8 shows the total linear strain of each of the samples as a percent of original length ($\Delta L / L \times 100$). As can be seen, there was a fair amount of variability in the measured strains for the samples tested, which might be caused by heterogeneity of the coal.

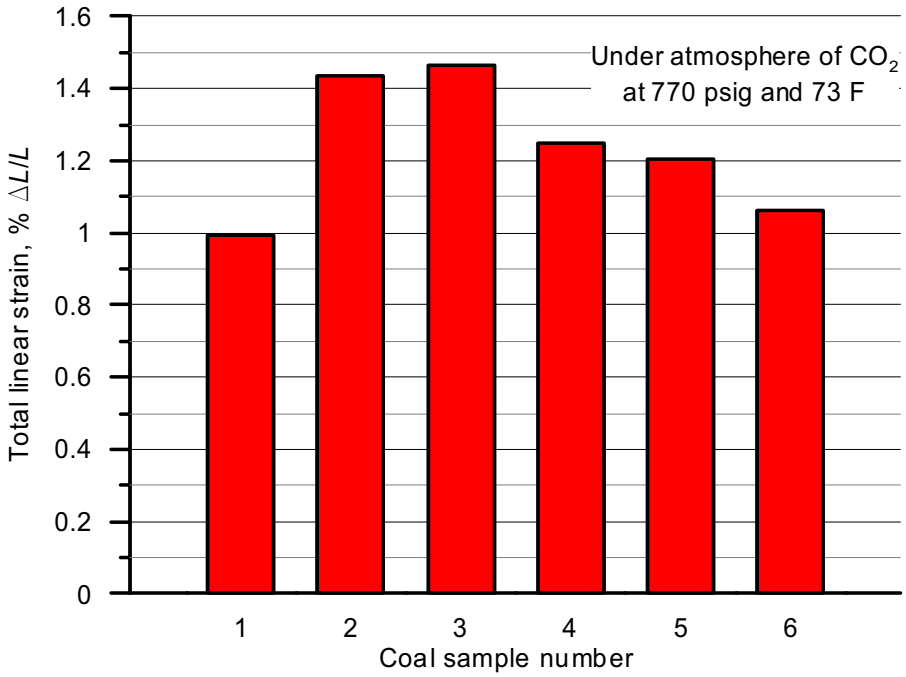

Figure 4.8. Total linear strain for six samples of Gilson-seam coal under identical test conditions.

Figure 4.9 shows the average strain build-up curve showing the standard deviation for the six samples. The average strain of all the samples is represented by the triangular data points. The vertical bars represent the standard deviation around the average and was calculated based on the spread in the strain data between the six coal samples measured.

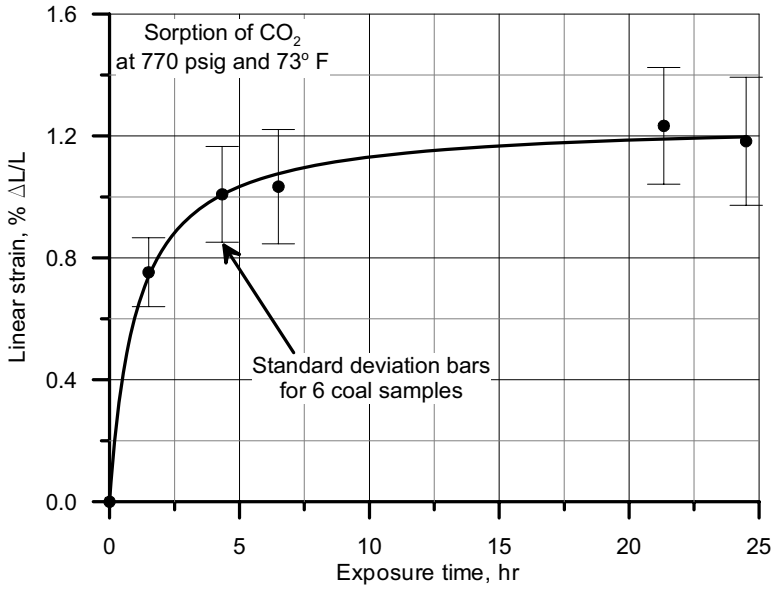

Figure 4.9. Average swelling response of Gilson-seam coal showing standard deviation of six different samples. The calculated average maximum strain is 1.25%.

4.2.2 Coal Heterogeneity Discussion

Comparing the swelling characteristics of six coal samples under identical conditions gives insight into the heterogeneity of the coal. Even though the samples were taken from the same small volume of coal, there is a fair amount of spread in the end points seen in Figure 4.8. The linear strain for these six samples ranged from 1.00% to 1.45%. If larger samples could have been used, perhaps the spread in strain measurements would have been smaller. Although bulkier samples might reduce the spread in the data, it would without question increase the equilibration time, which could make the acquisition of these kinds of data prohibitive. Averaging the strain data of a number of small samples is arguably a reasonable alternative to using larger samples

4.2.3 Modeling Strain Equilibration Time

The strain-time data shown in Figure 4.7 and Figure 4.9 were modeled using a Langmuir-type equation of the form:

$$S = \frac{S_t \cdot t}{t_L + t}, \quad \text{..... (4-1)}$$

where S is the observed linear strain, $\Delta L/L$; S_t is the maximum strain-time constant and represents the maximum amount of strain that can occur due to gas adsorption at infinite equilibration time at a given temperature and pressure; the time constant t_L corresponds to the time at which the observed strain is equal to one-half the maximum strain; and t is the time the sample is exposed to the new conditions (pressure or gas). At infinite time, observed strain, S, would equal the maximum strain, S_t.

Modeling the data in Figure 4.7 and Figure 4.9 with Eq (2) resulted in a very good fit: R-squared values of 0.997 and 0.996 respectively. The calculated values of maximum strain were 1.10% for Figure 4.7, and 1.25% for Figure 4.9. Recall that the data in Figure 4.7 were obtained using one single sample of coal, while the data in Figure 4.9 represented the average strain of six coal samples. Based on the excellent fit of the data, a very good estimate of maximum strain was calculated from data collected within the first 24 hours of exposure to the pressurized gas, which is a great improvement over the relatively long equilibration times required by methods employing strain gauges as described earlier.

4.2.4 Temperature Control and Possible Effect on Strain

These experiments were done at room temperature and no effort was made to regulate it, but it was monitored. The amount of adsorption (and by inference, resulting strain) is known to be a strong function of temperature [47, 48]. The room temperature during these experiments varied between 68° F and 75° F with an average of 73° F. The second

to the last data point in Figure 4.9 was taken at a temperature of 69° F, while the last data point was taken at a temperature of 73° F. At lower temperatures, more gas is adsorbed resulting in higher strains. This slight change in temperature could account for the decrease in strain from one point to the next. Studying the effect of temperature on coal strain was not included in the work scope of this project. In order to neglect any future temperature effects, the temperature was controlled at a constant value in all subsequent experiments by the addition of heat tape and insulation wrapped around the apparatus.

4.2.5 Discussion of Linear Strain versus Volumetric Strain

The main reason for obtaining coal strain data is to correlate strain data to changes in permeability. The volumetric strain of coal is needed to model changes in coal permeability as gas is adsorbed. In these experiments, linear strain was measured, not volumetric strain. A relationship between linear or longitudinal strain and volumetric strain is needed and derived in this section.

Longitudinal strain is defined as the change in length of a sample divided by its original length:

$$S_L \equiv \frac{\Delta L}{L}, \quad \text{(4-2)}$$

where ΔL is the change in length of a dimension and L is the original length of that dimension. Also, volumetric strain is defined as the change in volume of a sample divided by its original volume,

$$S_V \equiv \frac{\Delta V}{V}, \quad \text{(4-3)}$$

where ΔV is the change in volume of a body and V is the original volume of that body.

Assuming a solid, rectangular volume with dimensions L_1, L_2, and L_3, the change in volume (ΔV) can be calculated by subtracting the original volume (V) from the stressed volume:

$$\Delta V = (L_1 + \Delta L_1)(L_2 + \Delta L_2)(L_3 + \Delta L_3) - L_1 L_2 L_3. \quad \text{(4-4)}$$

Multiplying these terms and simplifying yields:

$$\Delta V = L_2 L_3 \Delta L_1 + L_1 L_3 \Delta L_2 + L_1 L_2 \Delta L_3 + L_1 \Delta L_2 \Delta L_3 + L_2 \Delta L_1 \Delta L_3 + L_3 \Delta L_1 \Delta L_2 + \Delta L_1 \Delta L_2 \Delta L_3. \quad \text{(4-5)}$$

Volumetric strain is calculated by dividing the change in volume (ΔV) by the original volume (V):

$$S_V = \frac{\Delta V}{V} = \frac{\left(\begin{array}{l} L_2 L_3 \Delta L_1 + L_1 L_3 \Delta L_2 + L_1 L_2 \Delta L_3 + L_1 \Delta L_2 \Delta L_3 \\ + L_2 \Delta L_1 \Delta L_3 + L_3 \Delta L_1 \Delta L_2 + \Delta L_1 \Delta L_2 \Delta L_3 \end{array} \right)}{L_1 L_2 L_3}. \quad \text{(4-6)}$$

Simplifying and canceling terms results in:

$$S_V = \frac{\Delta L_1}{L_1} + \frac{\Delta L_2}{L_2} + \frac{\Delta L_3}{L_3} + \frac{\Delta L_2 \Delta L_3}{L_2 L_3} + \frac{\Delta L_1 \Delta L_3}{L_1 L_3} + \frac{\Delta L_1 \Delta L_2}{L_1 L_2} + \frac{\Delta L_1 \Delta L_2 \Delta L_3}{L_1 L_2 L_3}. \quad \text{(4-7)}$$

Substituting the definition of longitudinal strain, $S_L = \Delta L / L$, into the above equation gives a rigorous derivation of the relationship between longitudinal strain and volumetric strain:

$$S_V = S_{L_1} + S_{L_2} + S_{L_3} + S_{L_2} S_{L_3} + S_{L_1} S_{L_3} + S_{L_1} S_{L_2} + S_{L_1} S_{L_2} S_{L_3}, \quad \text{(4-8)}$$

Coal, on a large scale, can be considered to be a layered and heterogeneous medium and layers of ash or other sediment can cause differences in vertical and horizontal strain. However, the samples used in these experiments are quite small and did not show any visible layering or changes in texture in any direction. By assuming the coal body is iso-

tropic, the strain becomes equal in all directions ($S_{L1} = S_{L2} = S_{L3} = S_L$), and the above relationship between linear and volumetric strains reduces to the following form:

$$S_V = 3S_L + 3S_L^2 + S_L^3 \quad \text{(4-9)}$$

If strain is small, the last two terms can be neglected and volumetric strain is approximately equal to three times the linear strain as shown in the following equation:

$$S_V = 3S_L \quad \text{(4-10)}$$

The assumption of isotropic conditions for coal is supported by the strain results reported by Levine [29]. In his experiments, strain was recorded for all three dimensions and both longitudinal strain and calculated volumetric strain were compared. The ratio of the longitudinal strain to the volumetric strain in Levine's data is 1:3, which supports the assumption that small samples of coal can be considered isotropic.

4.3 Strain Measurement Apparatus – Final Version

Based on the potential for temperature to affect the observed strain data as discussed in Section 4.2.4 , the entire pressure cell was wrapped with heat tape and insulated to better control the temperature. Temperature was controlled using input from the thermocouple inserted into the pressure cell through the upper gas port. Figure 4.10 is a photograph of the final version of the strain measurement apparatus showing the pressure cell wrapped in insulation, the digital filar microscope attached to the pressure cell, and the digital readout attached to the microscope.

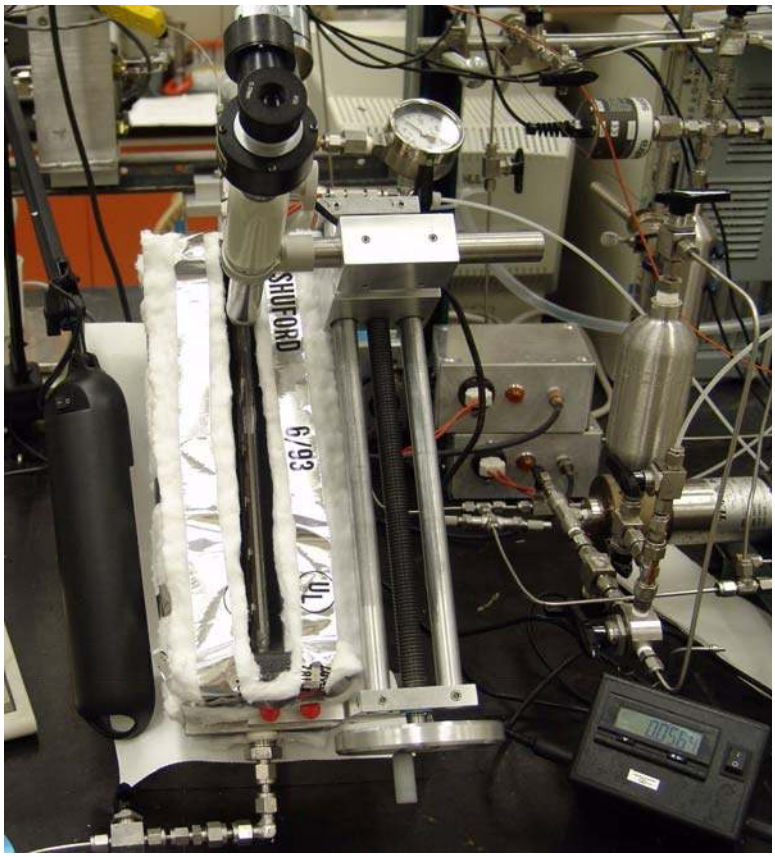

Figure 4.10. Photograph of the final version of the strain measurement apparatus. Pressure cell is wrapped in insulation, the attached microscope is attached to the top of the apparatus, and the digital readout is at the lower right of the photograph.

A series of experiments were designed and performed using the final version of the strain measurement apparatus. These experiments are described below.

4.3.1 Sample Preparation for Measurement of Strain Data

The small samples used to measure strain were taken from the larger blocks by using a rock saw cooled by de-ionized water. These small samples were then dried on the lab bench using paper towels, measured, and placed into the strain measurement apparatus.

Gas adsorption is known to be a strong function of moisture content [49, 50, 51]. To eliminate this potential source of variability in the strain data, the moisture within the samples was evaporated at 80^{o} F inside the strain measurement apparatus by cycling between a vacuum and high pressure moisture- and oxygen-free gas until strain at the pressure extremes was constant.

4.3.2 Experimental procedure

Much of the experimental procedure and resulting data has been previously reported by Robertson and Christiansen [52]. All strain measurements were done at a constant temperature of 80^{o} F. Initially, a hard vacuum was applied to the pressure chamber for 24 hours and then the initial location of each of the sample ends with respect to specific marks on the measurement standard was recorded. Gas was then introduced into the chamber and pressurized to a desired pressure and changes in the length of the samples were monitored over time as gas was adsorbed by the coal and the samples equilibrated to the new pressure state. The strain of five coal samples were averaged to arrive at an average strain value and one stainless steel sample was used as a control in all experiments. This procedure was repeated for a number of increasingly higher pressures until the maximum desired pressure was achieved. At that point, a hard vacuum was applied to determine the reversibility of the strain as gas was desorbed. The process was repeated for other gases of interest.

Strain measurements were obtained by following these steps:

With the microscope looking through the clear measurement standard overlying the clear glass wall of the pressure vessel, it is focused on the end of a coal sample and the eyepiece crosshairs are placed at the end of the sample by adjusting the horizontal adjuster (see Figure 4.4 for components of the filar microscope).

The digital readout is zeroed.

The microscope is then adjusted vertically (perpendicular to the plane of the direction of strain measurement) until it is refocused on the clear measurement standard on the outside of the pressure vessel.

The crosshairs are then adjusted until they are placed on the nearest mark on the measurement standard. This standard mark is used for all subsequent measurements associated with this sample.

The distance in millimeters between the end of the sample and the mark on the standard is read from the microscope's digital readout and recorded in laboratory notebook.

Once one of the sample measurements is taken, the entire microscope assembly is moved to the next sample by turning a threaded rod until the sample end comes into view through the microscope.

The strains of each of the samples are measured and averaged to arrive at a final strain value for that sample.

It takes about 10 minutes to collect this data for all six samples. This process is repeated every few hours until the distance between the ends of the samples and the standard marks ceases to change or nearly ceases to change, which generally occurs at about 24 hours.

The pressure of the gas is then increased by 200 psi (or some other desired step amount) and the whole process is repeated until data is collected at the maximum pressure of 1000 psi (or some other predetermined maximum).

A vacuum is then applied in one step and the shrinkage measurements are done in the same manner as the swelling measurements.

The entire process can generally be accomplished in seven to 10 days. When beginning a test with a different gas, a hard vacuum is maintained on the samples for 48 hours before any measurements are made to desorb all the previous gas and "re-zero" or initialize the samples.

4.3.3 Experimental Results – Strain Data with Respect to Time

Figure 4.11 is an example of the strain measurements collected over time for the Anderson coal and shows the average strain of five coal samples with respect to adsorption time under differing carbon dioxide and methane pressures. Note the difference in scale between the two plots. There is more scatter in the strain data for the methane sorption than for the carbon dioxide sorption because of the smaller strains induced by the sorption of methane compared to carbon dioxide.

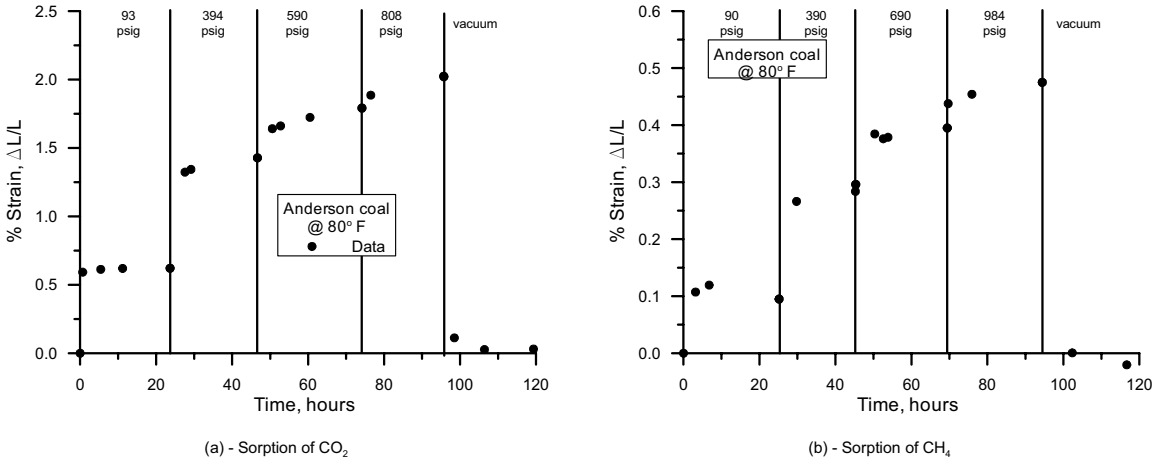

Figure 4.11. Change in Anderson seam coal strain with respect to time under different carbon dioxide (a) and methane (b) pressures.

As discussed previously in Section 4.2.3 , the relationship between strain and equilibration time (constant pressure) can be modeled very well using a Langmuir-type equation of the following form:

$$S = S_t \frac{t}{t_L + t}, \quad \text{..... (4-11)}$$

where S is the measured strain, S_t is the equilibrated strain (extrapolated to time = ∞), t is time in hours, and t_L is a constant representing the time at which S equals ½ S_t. The value of the equilibrated strain (S_t) is used later to construct strain versus pressure plots. Both S_t and t_L are variables determined by the shape of the strain-time data.

To model the data and obtain the appropriate constants (S_t and t_L), a macro was written for an Excel spreadsheet in Visual Basic to optimize the constants until the best fit of the data was obtained as measured by the R^2 value of the resulting equation. Appendix A lists the code used to optimize the constants in Eq (4-11). This approach was very helpful in extrapolating to infinite time (equilibrated strain) if the strain data were not completely stabilized after 24 hours. Figure 4.12 shows the same strain data as in Figure 4.11, but modeled using Eq (12).

For comparison, plots showing the sorption-induced strain data collected over time for the Gilson coal are shown in Figure 4.13. Each data point is an average of five strain measurements – one for each of the five samples of coal in the apparatus.

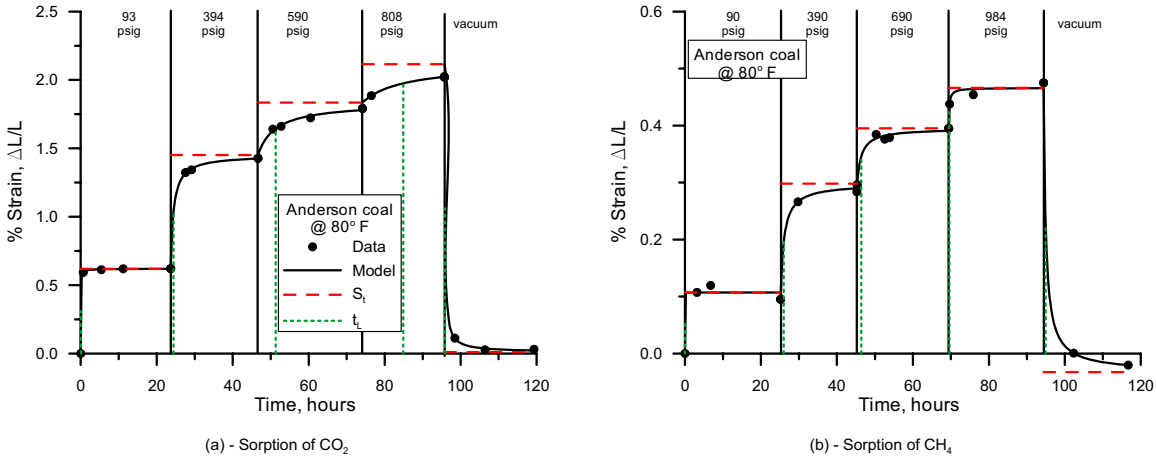

Figure 4.12. Change in Anderson seam coal strain with respect to equilibration time under different carbon dioxide and methane pressures. Also shown are the Langmuir-type models with corresponding constants.

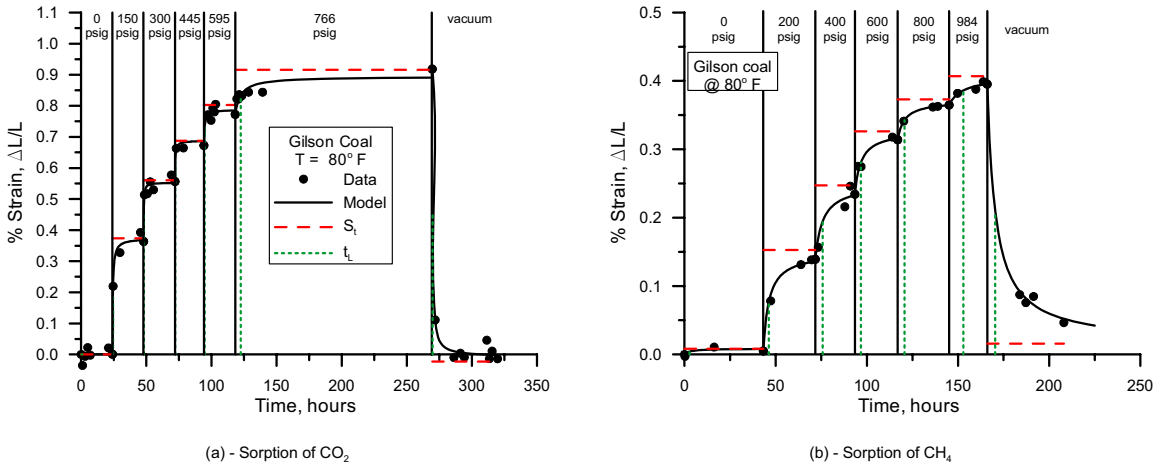

Figure 4.13. Average strain induced by the sorption of CO_2 (a) and CH_4 (b) plotted against equilibration time for the Gilson coal.

The constant t_L can be used as a measure of equilibration time; a small value for t_L means that the strain stabilized rapidly, while a large value for t_L represents a long stabilization time. Although not strictly the case, there appears to be a general trend for longer equilibration times as pressures increase from 0 psig towards 1000 psig. For example, strain data stabilized very quickly at lower pressures for CO_2 sorption with the Anderson coal (t_L = 0.032 hrs for 100 psia) and the equilibration time became progressively longer at the higher pressures (t_L = 10.7 hrs at 800 psia).

Figure 4.14 compiles all the equilibration time, t_L, data for the coals and pure gases and plots them versus the normalized pressure step ($\Delta p/p_{ave}$). There is quite a bit of scatter in the data, but generally, as the normalized pressure step decreases, the equilibration time increases. This finding is important as it will aid in the design of future strain experiments.

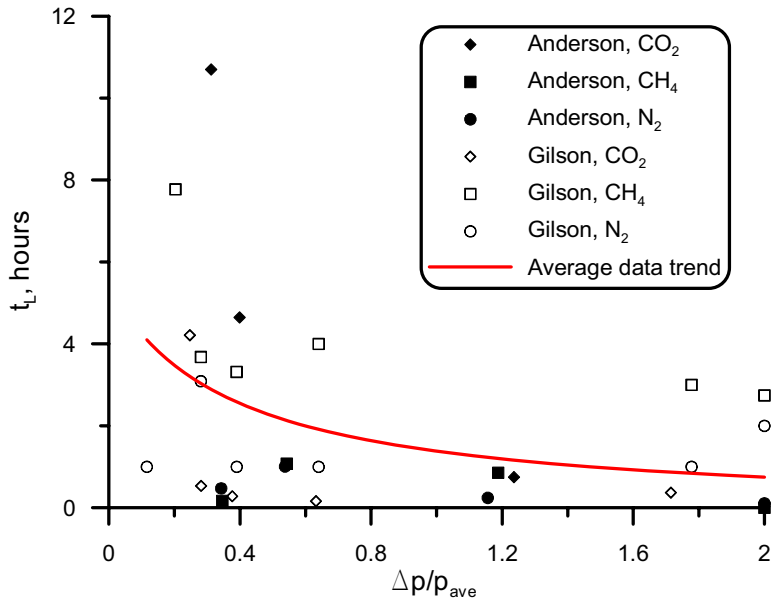

Figure 4.14. General relationship between the equilibration time, t_L, and the normalized pressure step, $\Delta p/p_{ave}$.

Eq (4-11) was used to extrapolate the 24 hours of strain data to infinite time in order to arrive at the stabilized strain for each pressure point as quickly as possible. In retrospect, more time could have been allowed for equilibration or more data points could have been taken to more fully establish the strain versus time trend. However, because the data is modeled very well by the Langmuir-type equation, any error associated with the extrapolation is expected to be small.

The calculated value of S_t at the various pressures was then used to construct a strain versus pressure plot. Figure 4.15 is an example of such data and also shows the strain measured in a non-reactive stainless steel bar used as a control for each of these experiments. In this figure the average longitudinal strain induced by the sorption of carbon dioxide is plotted for the Anderson seam coal.

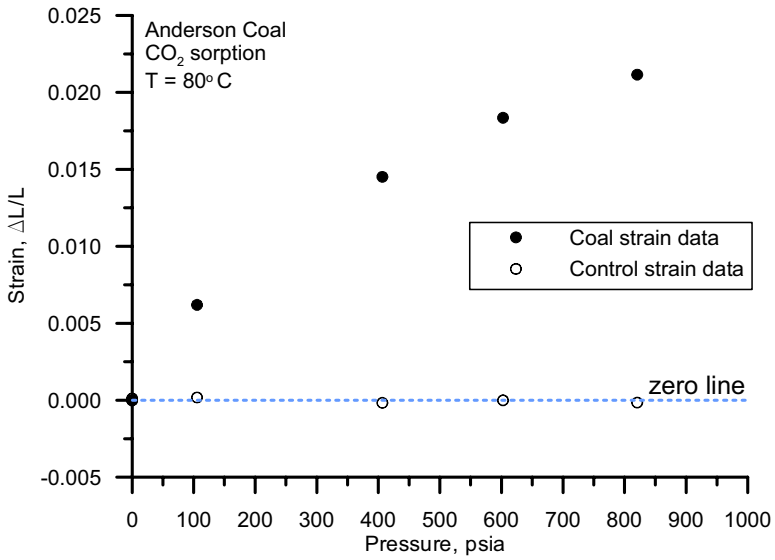

Figure 4.15. Measured longitudinal strain using coal from the Anderson seam under various CO_2 pressures. Also shown is the measured strain of a stainless steel sample used as a non-reactive control.

4.3.4 Discussion of Error Associated with Strain Data

Figure 4.15 also shows the measured strain of a stainless steel sample of the same size as the coal samples used as a control. Because stainless steel is non-reactive and does not display a change in dimensions with changes in gas pressure, any strain measured on the control sample is equivalent to the error associated with the measured strain in the reactive coal samples. All strain tests of the coal samples included a stainless steel control sample for quality control. The standard deviation of the error associated with Figure 4.15 (measured strain of control sample) was 0.0016% and was typical of all the strain experiments.

There was an element of operator skill associated with these strain measurements. The error associated with these measurements appeared to be random but was also related

to the ability, or inability, of the operator to accurately and repeatedly locate the ends of the samples or the calibration mark on the standard.

CHAPTER 5. PRESENTATION OF EXPERIMENTAL STRAIN DATA AND MODELING OF RESULTS

In this chapter the sorption-induced strain data versus pressure is presented for two coals of different ranks for pure gases and for a gas mixture. Some relationships between coal rank and strain are presented for pure gas sorption. In addition, prediction of strain induced by the sorption of a mixed gas based on the pure-gas strain parameters is discussed.

5.1 Experimental Strain and Modeling – Pure Gases

Sorption-induced strain as a function of pressure can be modeled using a Langmuir-type equation of the following form:

$$S = S_{max} \frac{p}{p_L + p}, \quad \text{..... (5-1)}$$

where S is the measured strain, S_{max} is the Langmuir strain, which is the maximum strain at a hypothetical infinite pressure, p is the gas pressure in psia inside the pressure chamber, and p_L is the Langmuir pressure, which is a constant representing the pressure at which S equals ½ S_{max}. Note that Eq (5-1) has the same basic form as Eq (4-11), which was used to model strain versus time data.

To model the strain versus pressure data, S_{max} and p_L were varied using the Excel spreadsheet macro in Appendix A until the R^2 value of Eq (5-1) was maximized.

Strain was measured using both the Gilson coal and the Anderson coal as a function of gas pressure for three pure gases: CO_2, CH_4, and N_2. Figure 5.1 shows the data resulting from these experiments, which were modeled using Eq (5-1). Table 5.1 shows the Langmuir strain constants accompanying the model curves for the different coals and

gases. Both coals exhibited the largest strain when adsorbing carbon dioxide; nitrogen-sorption induced the least strain in both coals tested; and the strain curve for methane adsorption fell between the carbon dioxide curve and the nitrogen curve for both coals.

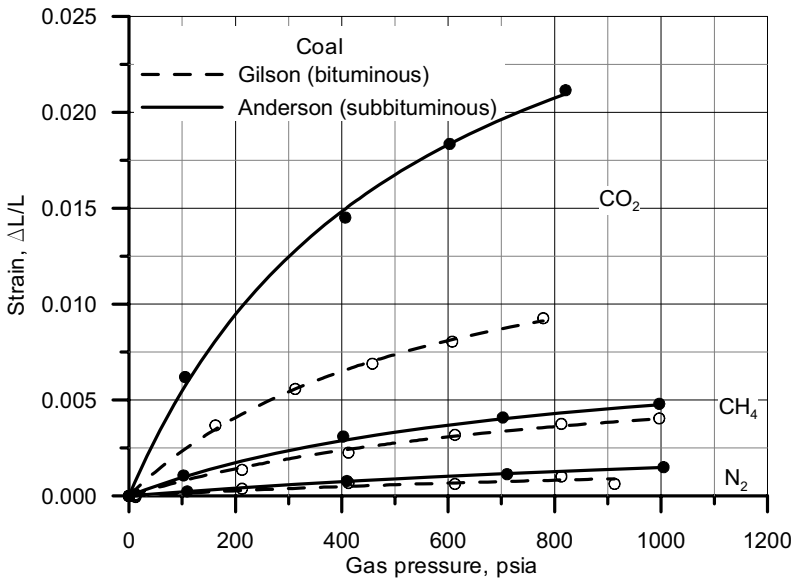

Figure 5.1. Strain curves for two different coals subjected to three different pure gases at various pressures. Solid circles are strain data for the Anderson coal and open circles are strain data for the Gilson coal.

5.1.1 Approach to Modeling Scattered Strain Data

The strain data seen in Figure 5.1 were modeled using Eq (5-1) by adjusting the values of the equation constants, S_{max} and p_L until the error associated with the calculated curve was minimized. To minimize the error, the coefficient of determination, R^2, was maximized. The equation for R^2 is:

$$R^2 = 1 - \frac{\sum\left(y - y^*\right)^2}{\sum\left(y - y^*\right)^2 + \sum\left(y - \bar{y}\right)^2}, \quad \text{..... (5-2)}$$

where y represents the measured strain data, y* represents the strain calculated by Eq (5-1), and $\bar{y}$ represents the average of the measured strain data. The value of the coefficient of determination can range from 0 to 1. An R^2 value of 1 indicates that the calculated curve passes through each data point indicating no differences between the measured and calculated data. As the value of R^2 decreases from unity towards zero, differences between the calculated values and measured data become larger.

Table 5.1. Langmuir strain constants for sorption-induced strain for Anderson and Gilson coals at 80° F.

Gas	Coal	Langmuir strain constants		R^2 value for curve fit
		S_{max}	P_L, psia	
CO_2	Anderson	0.03447	529.19	0.9985
	Gilson	0.01596	581.32	0.9972
CH_4	Anderson	0.00777	618.98	0.9997
	Gilson	0.00958	1070.82	0.9993
N_2	Anderson	0.00429	1891.44	0.9989
	Gilson	0.00112	348.41	0.8914

R^2 values are influenced by two possible conditions: 1) errors in the measured data and 2) errors with the model. Errors associated with the measured data are definitely present as demonstrated by the small scatter in the strain data of the control sample. However, when the measured strain is large, the error in the measured data is almost negligible. On the other hand, when the measured strain is small the error in the data can become significant.

Considering the strain data presented in Figure 5.1, the error associated with the CO_2 strain data is small relative to the magnitude of the strain measurements and very little

scatter is detected. However, the strain associated with nitrogen adsorption is much smaller than the CO_2 strain data and is approaching the lower limits of strain detection. In Figure 5.2, N_2 strain data using Gilson coal is plotted with the control sample for comparison. The magnitude of the N_2-induced strain is much less than the CO_2-induced strain; and because of this there is more apparent scatter associated with these data. Because of the data scatter, the confidence in the calculated Langmuir strain constants, S_{max} and p_L, is somewhat lower for N_2-induced strain than for CO_2-induced strain and rather large differences in the strain constants (S_{max} and p_L) could result in very nearly the same R^2 value for the N_2-induced strain data set.

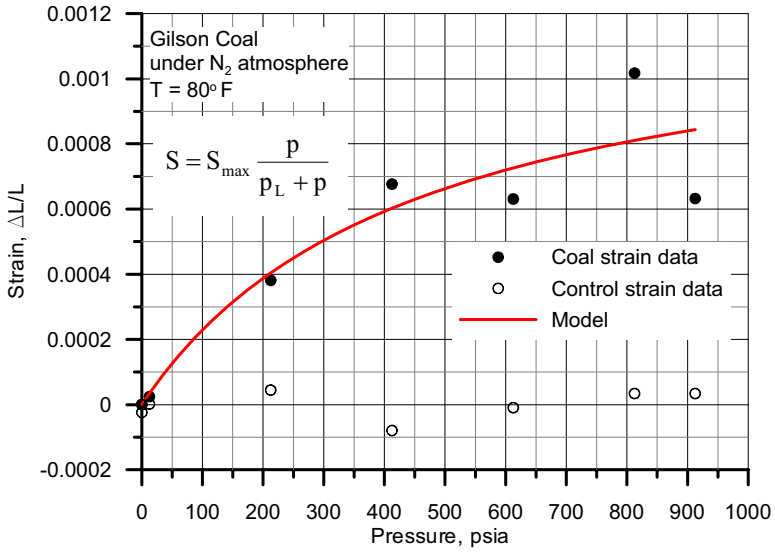

Figure 5.2. Measured Longitudinal strain using coal from the Gilson seam, Eastern Utah under various N_2 pressures. Also shown is the measured strain of the non-reactive control sample.

5.1.1.1 Relationship between S_{max} and p_L

The pressure constant, p_L, represents the pressure at which ½ of the maximum strain, S_{max}, is reached. These two parameters define the shape of the strain curve. A small value for p_L would result in a rapid increase in strain at low pressure, leveling off quickly as pressure increases. On the other hand, a large value for p_L could result in an almost linear rise in strain as pressure increased. Therefore, p_L controls the curvature and S_{max} controls the height of the strain curve. The data in Table 5.1 show a general trend of increasing p_L as S_{max} decreases.

The values for the pressure constant, p_L, are very similar for both coals when adsorbing carbon dioxide (see Table 5.1). That the strain curves for different coals adsorbing the same gas are of similar shape is an important finding for this allows the comparison of strain curves for different coals based on the value for S_{max}. In other words, if the pressure constant were the same for two coals, the sorption-induced strain curves could be compared by simply comparing the S_{max} values instead of a graphical comparison of the entire curve. Note that for methane, and then nitrogen, the maximum strain (S_{max}) becomes progressively smaller and the values for p_L become progressively less similar. The dissimilarity of the values of the pressure constants for nitrogen adsorption, and to a lesser extent for methane adsorption, could be attributed to increasing scatter in the strain data caused by the increasing influence of measurement error (see Figure 5.2).

5.1.1.2 Comparison of Strain Curves

Because of the magnitude of the CO_2-induced strain compared to the N_2-induced strain, there is inherently more confidence in the p_L values of the CO_2-induced strain curves. In the previous section it was noted that the p_L values of the CO_2-induced strain curves were very similar for both coals. It follows that the curvature of the respective

CH_4 and N_2 curves should also be similar, and averaging the p_L values for both coals for a given adsorption gas could be reasonable.

By using the average p_L value for both coals for a given gas, a normalized S_{max} was calculated and used to consistently compare strain data between coals and gases. Table 5.2 shows the resulting modified strain curve constants and the coefficient of determination, R^2, for each data set. Note that the R^2 values for each data set in Table 5.2 are very close to the original values listed in Table 5.1, which means that the model using the modified constants fits the data very nearly as well as the model using the original strain constants. For comparison, Figure 5.3 shows models using both the modified strain constants and the original strain constants for all three adsorbing gases.

Table 5.2. Modified Langmuir strain constants for sorption-induced strain for Anderson and Gilson coals at 80° F.

Gas	Coal	Modified strain constants		R^2 value for curve fit
		Normalized S_{max}	Average p_L, psia	
CO_2	Anderson	0.03527	555.25	0.9984
	Gilson	0.01559		0.9972
CH_4	Anderson	0.00907	844.90	0.9969
	Gilson	0.00838		0.9981
N_2	Anderson	0.00305	1119.93	0.9949
	Gilson	0.00196		0.8639

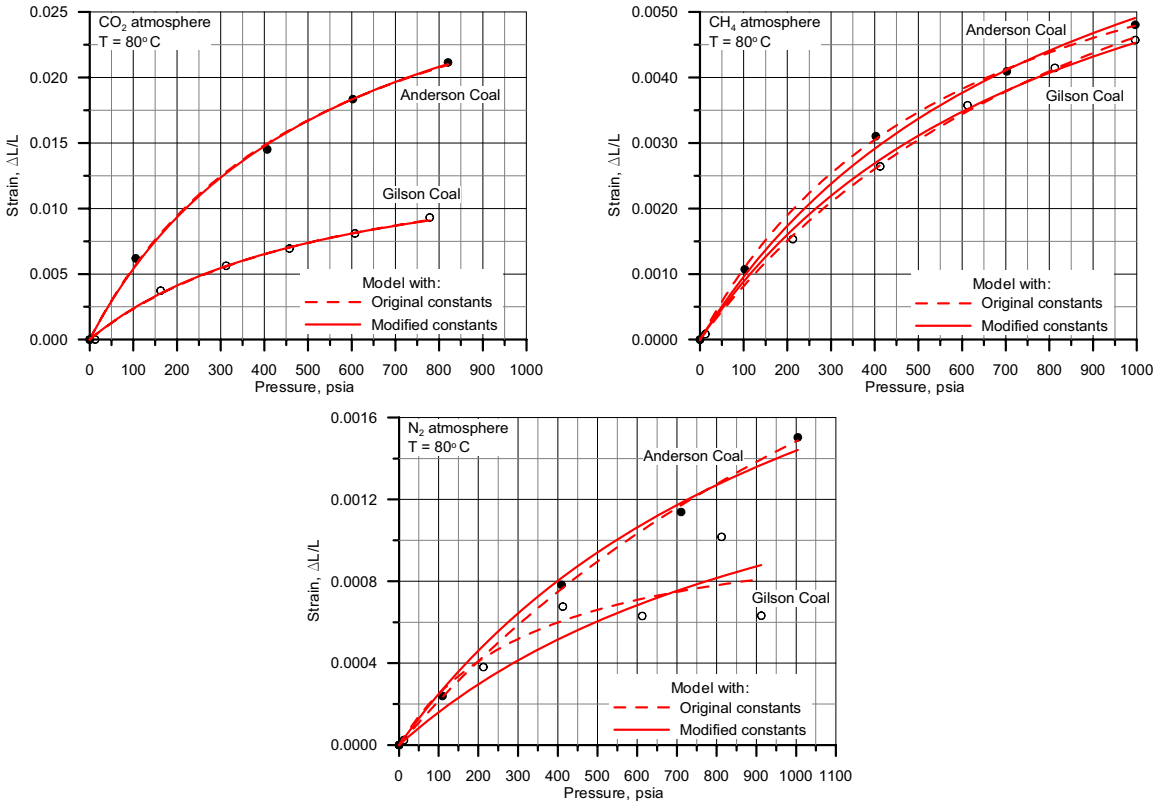

Figure 5.3. Comparison of models using original and modified strain constants.

The strain models using the original and the normalized strain constants overlie each other for the carbon dioxide data (Figure 5.3a); there is a slight difference in the curves for the methane data (Figure 5.3b); and an even larger difference for the nitrogen data (Figure 5.3c). However, even though the resulting curves were slightly different, the data were still modeled reasonably well using the normalized strain constants as shown by the relative small difference in R^2 values between Table 5.1 and Table 5.2.

The relationship between S_{max} and p_L can be seen in Figure 5.4, which plots the average value of p_L, as a function of the normalized S_{max} for both the Anderson and Gilson coals. The trend shown in this figure for a declining p_L with an increasing S_{max} is almost linear. The trend for higher values of p_L as S_{max} decreases results in a "straightening out"

of the strain curve as total strain decreases. This observation with the shape of the strain curves is analogous to the trend observed in adsorption curves where the Langmuir pressure, p_L, tends to increase as adsorption decreases [30, 56].

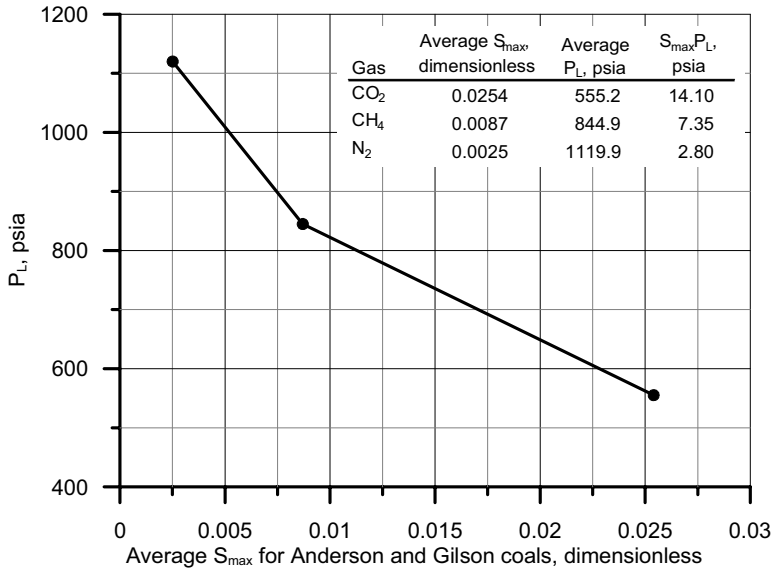

Figure 5.4. The relationship between the average Langmuir pressure and the average maximum strain for two different coals using three gases.

Figure 5.4 also shows data suggesting that the product of Langmuir strain constant and the Langmuir pressure ($S_{max} \cdot p_L$) decreases as S_{max} decreases; and ranges from 14 psia for CO_2 down to 2.8 psia for N_2.

5.1.2 Discussion of Shape of Sorption-Induced Strain Data

Seidle and Huitt reported pre-1990 coal strain data from several authors suggesting that sorption-induced coal strain varied linearly with pressure [28] and some early results from Harpalani and Schraufnagel [27] appear to indicate that sorption-induced strain in

coal could be linear with respect to pressure. However, the data presented in Figure 5.1 clearly indicate that sorption-induced strain is not a linear function of gas pressure, but can be very satisfactorily modeled using a Langmuir-type equation. This should be expected because the principal cause of the change in coal dimensions (strain) is the sorption of gas, which is also modeled by a Langmuir equation.

A secondary cause of strain in these experiments is the gas pressure acting to compress the coal samples. As gas pressure changes, the resulting compressive and sorptive strains are counter acting. The matrix compressive strain is small relative to the sorption-induced strain in the presence of carbon dioxide, but may become important when the sorbed gas is only slightly adsorptive such as nitrogen. The matrix compressibility can be determined by measuring the strain of a coal sample subjected to the pressure of a non-adsorbing gas such as helium. Figure 5.5 shows the strain induced by the exposure of the coal samples to helium at various pressures with temperature held constant at 80^{o} F. These data were obtained after allowing sufficient equilibration time to arrive at constant values with respect to time. From the data shown in Figure 5.5, the longitudinal matrix compressive strain is calculated to be 0.84E-6 psi^{-1}, which translates into a volumetric matrix compressibility of 2.5E-6 psi^{-1} for Anderson (vitrinite reflectance, R_o = 0.24%) coal at 80^{o} F. Schuyer et al. [53] reported compressibilities of "whole" coal ranging from 0.70E-6 psi^{-1} for a coal with R_o = 6.2% to 1.43E-6 psi^{-1} for a coal with R_o = 0.75%. (Note: Schuyer et al. reported compressibilities of coal correlated with the % carbon on a dry, ash-free (daf) basis. The % carbon daf was converted to vitrinite reflectance, R_o, using the correlation given by Berkowitz [54] to be able to compare Schuyer et al.'s compressibilities with that measured for the Anderson coal.) A direct comparison between the compressibility measured on the Anderson coal with those reported by Schuyer et al. is not intended, nor possible because of coal differences; however, the Anderson coal compressibility lies within the same trend as the Schuyer et al. data, which adds a level of credibility to the strain data generated as part of this work.

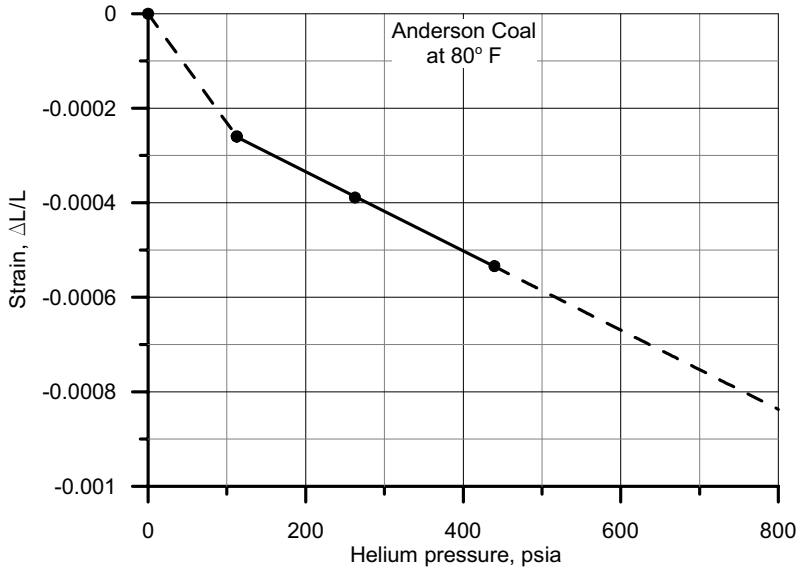

Figure 5.5. Longitudinal strain of Anderson (subbituminous) coal induced by various helium gas pressures at a constant temperature of 80° F.

Both adsorption isotherms and strain isotherms can be modeled using forms of the Langmuir equation and it may be possible to predict one based on the character of the other. There is evidence that for most gases and coals, the relationship between strain and adsorption is linear [29, 30]. However, Pekot and Reeves suggest that for high adsorbed gas concentration, the adsorption-strain relationship may become non-linear [55]. More work needs to be done in this area before any strong conclusions can be made as to the relationship between strain and adsorption curves, but there is strong evidence that there is a positive (and possibly linear) relationship between the sorption and strain isotherms.

5.1.3 Relationship between Strain and Coal Rank

The data presented in Figure 5.1 show a marked difference in the sorption strain between the two ranks of coals studied here. The relationships between sorption-induced

strain and coal rank for the three gases used in this study are shown in Figure 5.6. In this figure, S_{max} is used as a measure of strain and vitrinite reflectance is used as a measure of coal rank. The CH_4-induced strain decreases only slightly with the change in coal rank, but the CO_2- and N_2-induced strain curves each decrease by a factor of about two as vitrinite reflectance increases from 0.24 to 0.53. One would expect the strain curves of all three gases to be affected in the same manner by the change in coals, and more work should be done to determine if the CH_4 data are truly unaffected by a change in coal rank or if it is simply an experimental anomaly.

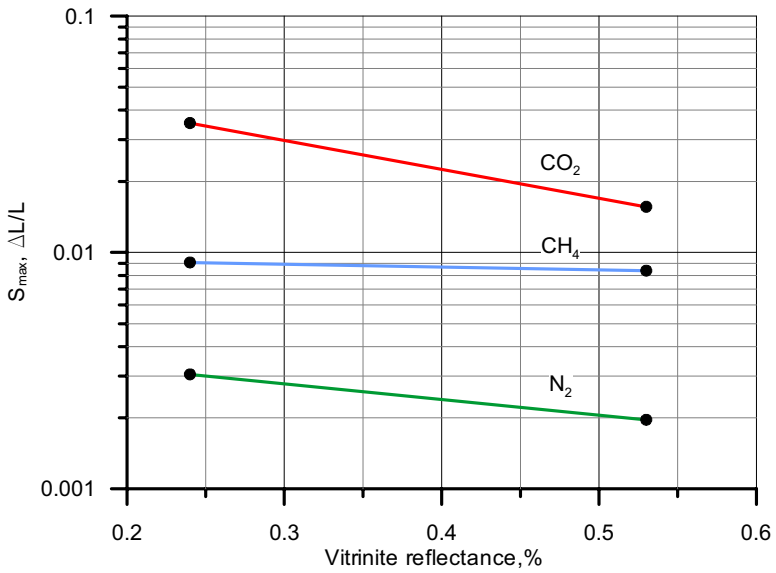

Figure 5.6. Results for two coal samples show that maximum strain decreases as vitrinite reflectance (coal maturity) increases.

Regardless of the amount of decrease in strain resulting from an increase in coal rank, the strain of all three gases did decline as rank increased. Other researchers, however, have shown different results. Bustin [56] compared the adsorption capacity (not strain) of coals of different ranks and found a trend towards higher capacity with higher coal

rank. Later, Chikatamarla and Bustin [30] measured sorption-induced strains of various coals and found that strain also increased with higher coal rank (shown in Figure 5.7), which is contrary to the data reported in Figure 5.6. Based on these results, it may not be possible to infer a general relationship between coal strains (and by analogy, adsorbed gas) and coal rank without further testing on a much larger group of coals of various ranks.

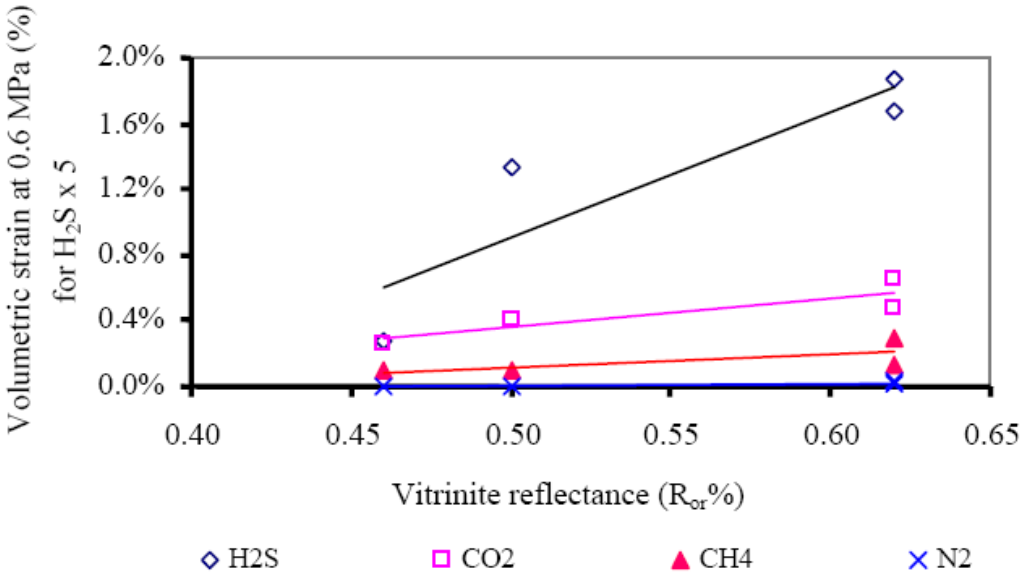

Figure 5.7. Strain as a function of vitrinite reflectance from Chikatamarla and Bustin [30]. This increasing trend is in opposition to the trend shown in Figure 5.6 of this current work.

5.1.4 Relationship between Carbon Dioxide/Methane Strain Ratios and Coal Rank

The ratio of strain induced by CO_2 adsorption to strain induced by CH_4 adsorption is of some importance when considering using coal seams as CO_2 sinks for sequestration of carbon or considering CO_2-enhanced CBM production (CO_2-ECBM). During either of

these two processes, the strain in the coal increases as CO_2 displaces methane. If the increase in strain is large enough, this can cause a significant reduction in permeability. Figure 5.8 shows the ratio of CO_2 strain and CH_4 strain for the two coals tested. This figure shows that if all the methane in the coal were to be displaced by carbon dioxide, the expected increase in strain would be about twice as large in the subbituminous coal compared to the bituminous coal. Therefore, permeability reduction due to coal swelling during CO_2-ECBM or CO_2 sequestration in coal appears to be sensitive to the rank of the coal and may be more of a detriment in coals of lower rank. This knowledge should be considered during the field selection process for CO_2-ECBM or CO_2 sequestration planning stages.

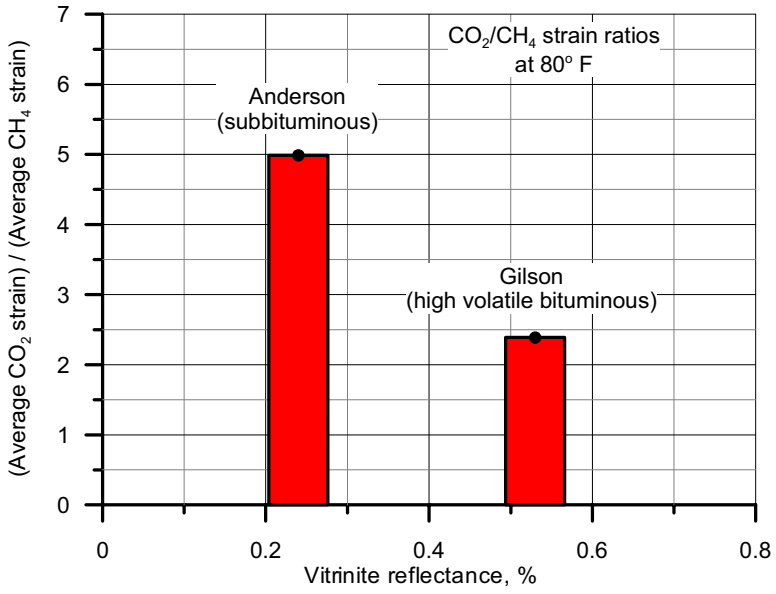

Figure 5.8. Average CO_2/CH_4 strain ratios for two coals of distinct ranks showing a decrease in the CO_2/CH_4 strain ratio with an increase in coal rank.

Reeves [57] compiled some historical data showing a relationship between the CO_2/CH_4 adsorption (not strain) ratio and coal rank and found that as coal rank increased

from subbituminous to high volatile bituminous the CO_2/CH_4 adsorption ratio decreased. However, Chikatamarla and Bustin [30] published strain data showing very little trend in CO_2/CH_4 strain ratio with respect to coal rank. The data shown in Figure 5.8 tend to support the results presented by Reeves, but definite conclusions regarding the relationship between CO_2/CH_4 strain ratios and coal rank are difficult to make because data for only two coals have been collected to date, and further testing should be done.

5.2 Experimental Strain and Modeling – Gas Mixtures

Strain induced by the adsorption of pure gases can be modeled by the Langmuir adsorption relationship as shown conclusively in Figure 5.1. Armed with that knowledge, extended Langmuir theory [58] then suggests that strain induced by the adsorption of gas mixtures can be predicted from the Langmuir constants defining the shape of the pure gas strain curves. The strain constants for pure gases in Table 5.2 should be able to be used to calculate the strain curve for a mixture of these gases by applying extended Langmuir theory. Simple Langmuir theory assumes that there is an ideal localized monolayer and that there is no interaction between adsorbed molecules. The following equation is an extended version of the Langmuir isotherm equation (modified for strain instead of adsorption) that accounts for multiple components in the gas phase:

$$S_{mix} = \frac{p\sum_{i=1}^{n}\left(\frac{S_{max_i} y_i}{p_{L_i}}\right)}{1 + p\sum_{i=1}^{n}\left(\frac{y_i}{p_{L_i}}\right)}, \quad \text{(5-3)}$$

where S_{mix} is the coal strain predicted by the adsorption of a gas mixture, i represents each pure gas component of the mixture, n is the total number of pure gas components, S_{max} is the maximum strain constant for each pure gas component, p_L is the Langmuir pressure constant for each pure gas component, and y is the mole fraction of each pure

gas component. According to this equation, if the individual strain-pressure curves were known for each pure gas in the mixture, the strain-pressure curve for any mixture of these gases could be directly calculated.

To test the accuracy of the above equation, the strains of the same Anderson coal and Gilson coal samples used with the pure gases were measured using a gas mixture of 51% N_2 and 49% CO_2. The gas composition was determined by gas chromatography. The measured strain data of the two coals for this gas mixture are shown in Figure 5.9. This figure also shows results of the extended Langmuir strain equation [Eq (5-3)] using pure gas strain constants from Table 5.2.

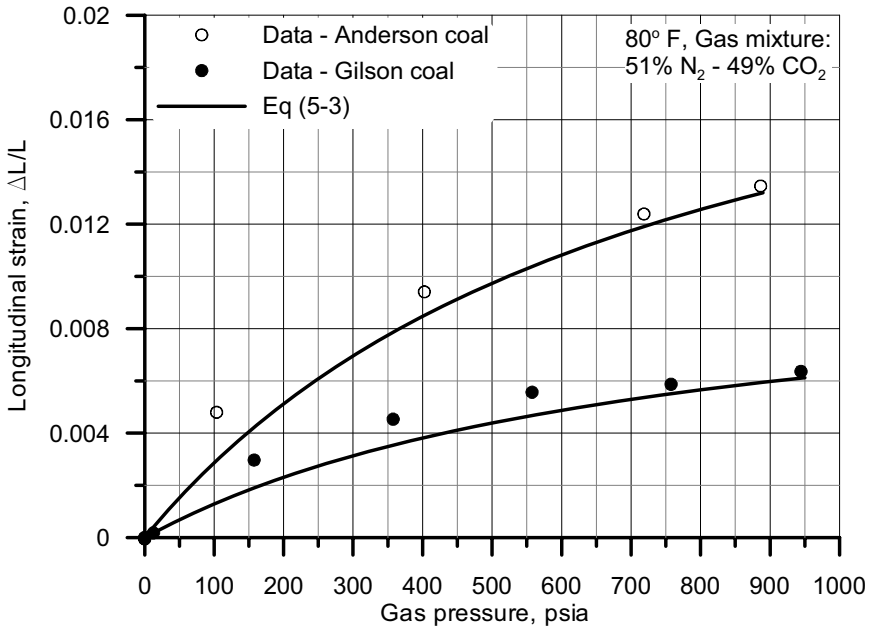

Figure 5.9. Strain of Anderson and Gilson coal caused by the adsorption of a gas mixture of 51% N_2 and 49% CO_2. The data are modeled using Eq (5-3) and the strain data for pure gases found in Table 5.2.

Modeling the mixed gas strain data for both cores using Eq (5-3) appears to be fairly accurate. The R^2 value for the Anderson coal curve is 0.968 and the R^2 value for the Gilson coal is 0.924. Both curves, however, under-predicted the amount of measured strain associated with adsorbing this particular gas mixture based on the strain curve of the pure gas components, which leads to the hypothesis that there may be some other component to the physics of the adsorption process that Eq (5-3) does not include.

Yang [59] presents a more sophisticated version of the extended Langmuir equation that takes into account the lateral interactions among adsorbed molecules that could be used to more accurately model mixed gas strain:

$$S_{mix} = \frac{p\sum_{i=1}^{n}\left(\frac{S_{max_i} y_i}{\eta_i p_{L_i}}\right)}{1 + p\sum_{i=1}^{n}\left(\frac{y_i}{\eta_i p_{L_i}}\right)} \quad \text{..... (5-4)}$$

where η describes the changes in interaction energies in the mixed adsorbates, which can either be greater or less than unity. If $\eta = 1$, Eq (16) reduces to Eq (5-3).

Because η accounts for the interaction energies between different species of gas molecules (not the adsorption energy between the substrate and the sorbing gas), it stands to reason that η should be independent of the adsorbing substrate (coal) surface. The strain data for the gas mixture are replotted in Figure 5.10 along with two extended Langmuir strain models – Eq (5-3) and Eq (5-4) – for comparison. Optimal values for η_{N2} and η_{CO2} were determined to be 0.25 and 0.58 respectively, by varying each independently until a reasonable match of the strain data was obtained using only the Gilson coal.

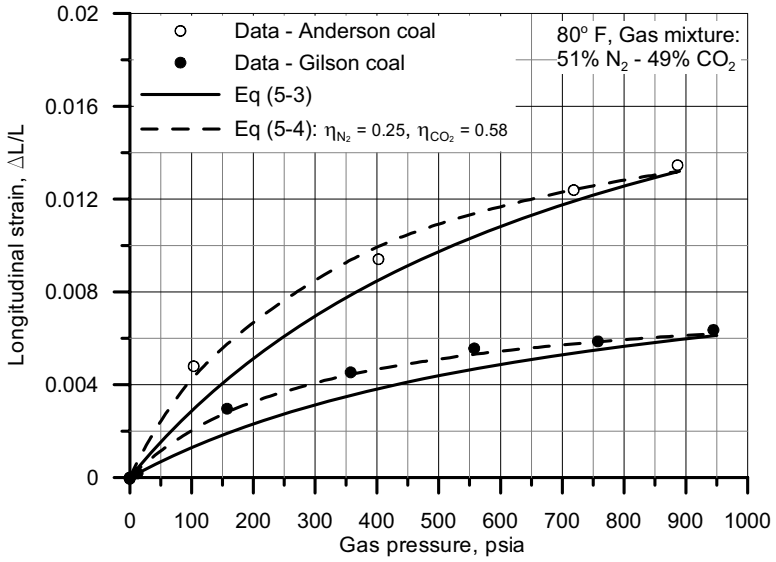

Figure 5.10. Strain data for Anderson and Gilson coals induced by the sorption of a mixed gas modeled by two different versions of the extended Langmuir strain equation: one neglecting interaction energies between molecules and the other accounting for molecule interaction.

The same values for η_{N2} and η_{CO2} were applied to the Anderson coal strain data and found to model it very well: the R^2 value for the Anderson coal for Eq (5-4) was 0.995 and for the Gilson coal the R^2 value was 0.997 using Eq (5-4). That the mixed-gas strain data for both coals were well modeled using the same values for η_{N2} and η_{CO2}, confirms experimentally that the gas interaction energies are independent of coal type.

CHAPTER 6. PERMEABILITY CHANGES IN COAL INDUCED BY SORPTION OF PURE GASES

In this chapter, the preparation of the coal cores for permeability measurements is discussed, the permeability apparatus and measurement methods are described, and modeling of the measured permeability is also discussed. As discussed earlier in Chapter 5, sorption-induced strain was measured for two different coals and three gases. Permeability measurements were also made using the same coals and gases under various pressure and stress regimes and have been previously reported by Robertson and Christiansen [60]. Results of these measurements and comparison of three permeability models from other researchers are presented in this chapter. This work should be of value to those who model coalbed methane fields using reservoir simulators.

6.1 Preparation of Cores for Permeability Tests

Cores used to measure permeability were drilled parallel to the bedding plane from the same coal blocks described earlier in this thesis using de-ionized water as the cooling/lubricating fluid. Some of the 2-inch diameter cores "fell apart" either while drilling or attempting to remove them from the bit, but persistence and care resulted in many good cores for flow tests. The cores were stored in small, sealed containers under de-ionized water until used in the experiments.

6.2 Permeability Measurements

All permeability measurements were made at 80° F with gas as the flowing fluid using 2-inch diameter cores. Figure 6.1 is a photograph of inlet and outlet faces of the two

cores used in the permeability measurements. The cleat system can be clearly seen in this figure.

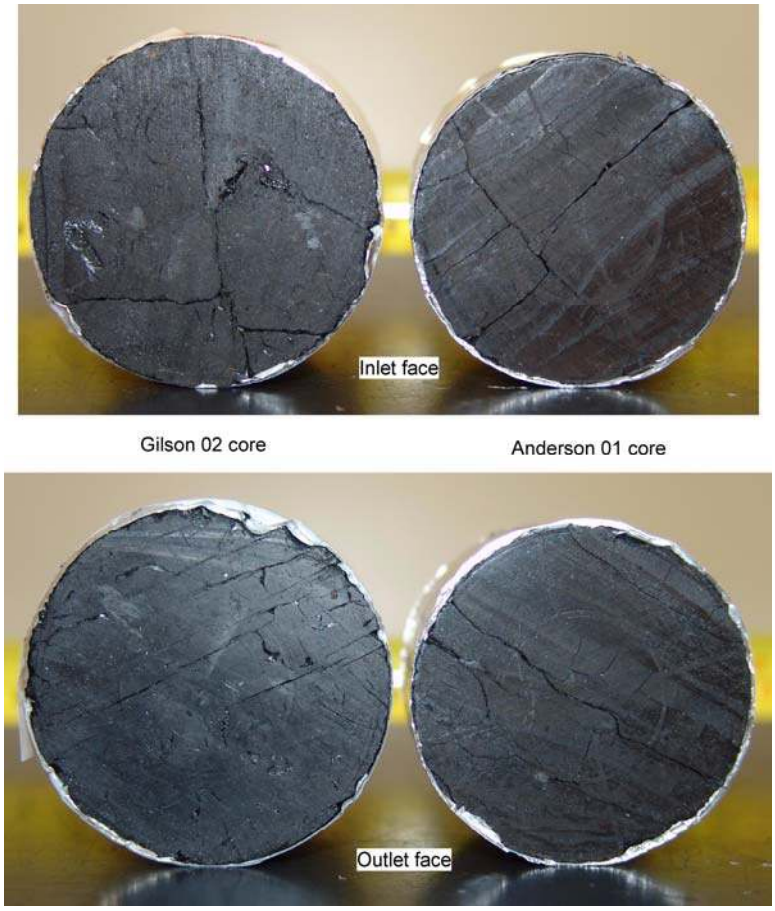

Figure 6.1. Photograph of inlet and outlet faces of cores used for permeability measurements. Cores are two inches in diameter.

6.2.1 Description of Permeability Apparatus Description

A hydrostatic-type core holder was used for the permeability experiments, which applied the same confining pressure to all surfaces of the cores. The flowing gas was supplied by pressurized gas cylinders and the flow rate was controlled by adjusting both the

cylinder regulator and a metering valve upstream of the core holder. A back pressure regulator was used to apply a minimum of 100 psia of pore pressure in order to minimize the Klinkenberg effect (assumed to be negligible at these conditions) of gas permeability measurements. Upstream and differential pressure measurements were made using pressure transducers. A flow meter was placed directly downstream of the back pressure regulator. All temperature, pressure, and time readings were logged onto a laboratory computer using data acquisition hardware[3] and analyzed using LabView™ software.[4] Figure 6.2 is a schematic of the permeability apparatus used in these experiments. LabView™ was also used to perform the calculations necessary to convert the input signals from the sensory equipment into pressure and temperature values with the appropriate units and to control the temperature and automatic valves used in the system as well as write the output data to a spreadsheet.

6.2.2 Permeability Calculation and Methodology

Permeability was calculated according to the following equation for linear flow through cylindrical cores:

$$k = \frac{q_{avg}\mu_{avg}L}{A\Delta p} \quad \text{..... (6-1)}$$

where k is permeability, q_{avg} is the average gas flow rate through the core calculated at the average pore pressure, μ is viscosity of the flowing fluid calculated at the average pore pressure, L is the length of the core sample, A is the cross-sectional area of the core, and Δp is the differential pressure across the core.

---

[3] FieldPoint FP-1601 module manufactured by National Instruments Corporation, 11500 N. Mopac Expressway, Austin, Texas 78759.

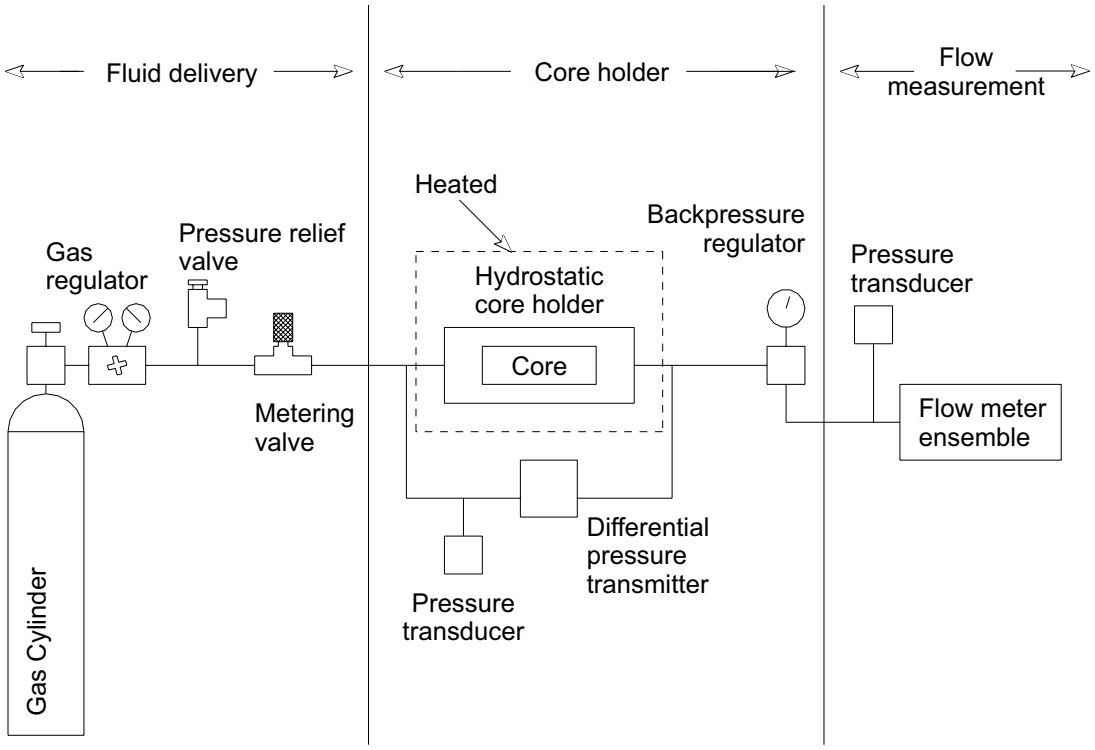

Figure 6.2. Drawing of the permeability apparatus.

6.2.2.1 Flow Meter Description

The flow rate through the core was calculated using a flow meter designed specifically for these experiments where mixtures of different gases could potentially be present. Figure 6.3 is a schematic drawing of the configuration of the flow meter used in these experiments. The flow rate of gas was obtained by measuring the rate of gas-pressure build-up in a known volume.

---

[4] A product of National Instruments Corporation, 11500 N. Mopac Expressway, Austin, Texas 78759.

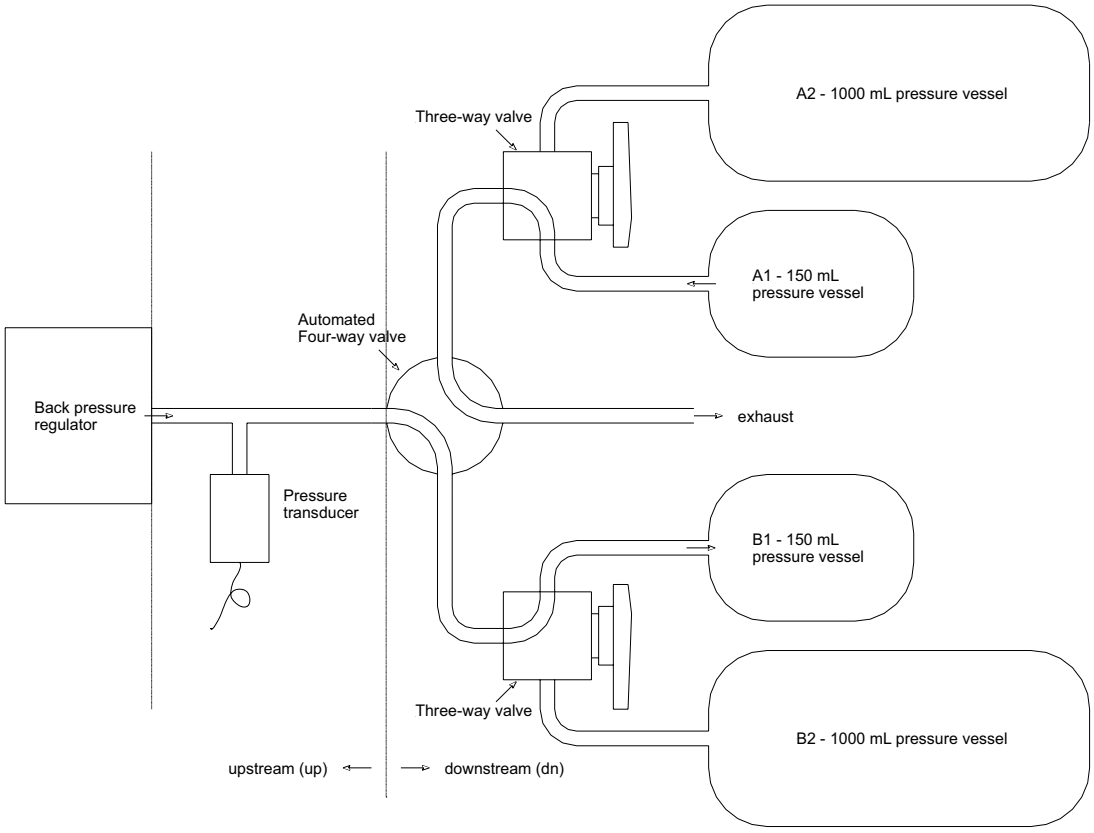

Figure 6.3. Illustration of the flow meter used during permeability experiments.

The flow meter consisted of two (or more) cylinders of equal volume, an automatic 4-way valve, and a pressure transducer. The final set up used in the permeability experiments included sets of cylinders of two different volumes: 150 mL for low flow rates and 1000 mL for higher flow rates. The volumes “A1” and “B1” shown in Figure 6.3 were made equal by adjusting the length of the lines connecting the cylinders to the 3-way

valves as were volumes “A2” and “B2.” The automated 4-way valve was configured to turn 90 degrees when the pressure in the filling vessel reached some predetermined value, such as 50 psig. When the ‘trip’ pressure was reached, and the 4-way automatic valve turned, which exhausted the pressurized cylinder and began to pressurize the empty cylinder. This process was continually repeated resulting in continuous, real-time measurement of gas flow rate. With this type of flow meter the pressure immediately downstream of the back-pressure regulator must be equal to or greater than the trip pressure.

6.2.2.2 Derivation of Equation Used to Calculate Flow Rate

The ideal gas law was assumed to apply because pressures in the flow meter were less than 50 psig.

$$n_{tot} = \frac{pV_{tot}}{RT}, \quad \text{(6-2)}$$

where n_{tot} is the total number of moles in the control volume; p is the pressure of the system; V_{tot} is the total volume of the system and is the sum of the upstream volume (V_{up}) and the downstream volume (V_{dn}); R is the universal gas constant, and T is the temperature of the system. The total control volume included the volume of the cylinders and the flow lines downstream of the back pressure regulator.

At some time, t_1, the number of moles in the control volume was:

$$n_{tot_1} = \frac{p_1 V_{tot}}{RT_1}, \quad \text{(6-3)}$$

where p_1 is the pressure in the control volume at time t_1, and T_1 is the temperature of the system at t_1. Likewise, at some time, t_2, the number of moles in the system was:

$$n_{tot_2} = \frac{p_2 V_{tot}}{RT_2}, \quad \text{(6-4)}$$

where p_2 is the pressure in the system at time t_2 and T_2 is the temperature of the system at t_2. The change in the number of moles of gas within the system from t_1 to t_2 was found by subtracting Eq (6-4) from Eq (6-3):

$$\Delta n_{tot} = n_{tot_2} - n_{tot_1} = \left(\frac{p_2}{T_2} - \frac{p_1}{T_1} \right) \frac{V_{tot}}{R}. \quad \text{(6-5)}$$

To convert the change in the total moles of gas within the system, Δn_{tot}, between t_1 and t_2 to the volume of gas produced at standard conditions between the same time values, the ideal gas law was applied:

$$V_{sc} = \Delta n_{tot} R \left(\frac{T}{p} \right)_{sc}. \quad \text{(6-6)}$$

Substituting Eq (6-5) into Eq (6-6) gives the working equation for the amount of gas produced between t_1 and t_2:

$$V_{sc} = \left(\frac{p_2}{T_2} - \frac{p_1}{T_1} \right) \cdot \frac{T_{sc}}{p_{sc}} \cdot V_{tot}. \quad \text{(6-7)}$$

where pressures and temperatures are absolute, and V_{tot} is the total control volume of the system.

The flow rate was defined as the volume of gas at standard conditions produced between t_1 and t_2 divided by the change in time:

$$q_{sc} = \frac{V_{sc}}{t_2 - t_1} = \left(\frac{p_2}{T_2} - \frac{p_1}{T_1} \right) \cdot \frac{T_{sc}}{p_{sc}} \cdot \frac{V_{tot}}{t_2 - t_1}, \quad \text{(6-8)}$$

where q_{sc} is the flow rate at standard conditions, such as standard milliliters per second. A thermocouple placed on the outside of the pressure cylinder was used to measure T_1 and T_2; a pressure transducer was used to measure p_1 and p_2; and the computer clock was used to measure t_1 and t_2. Using this methodology, the flow rate of the gas stream at standard conditions, regardless of its composition, was calculated.

To convert the flow rate at standard conditions to in situ conditions, the real gas law was used:

$$q_{\text{in situ}} = \left(\frac{pq}{T}\right)_{sc}\left(\frac{ZT}{p}\right)_{\text{in situ}}, \quad \text{(6-9)}$$

where the subscript 'sc' stands for standard conditions. The compressibility factor, Z, for pure gases was taken from the National Institute of Standards and Technology (NIST) WebBook [61]. Plots of the pure gas data were constructed and polynomial curves were used to model the data, which were then used to calculate Z factors for pure gases based on temperature and pressure.

When gas mixtures were used as the flowing fluid, the mole-fraction weighted average Z factor [62] was calculated and used to convert to in situ conditions. The weighted average Z factor is a function of the Z factors of the pure gases and their respective mole fractions and is defined by the following relationship:

$$Z_{av} = Z_1 x_1 + Z_2 x_2 + \ldots + Z_n x_n, \quad \text{(6-10)}$$

where x is the mole fraction of each of the gases in the mixture.

6.2.2.3 Viscosity Data and Calculation

Data for viscosity of the pertinent gases were collected as a function of temperature and pressure from the NIST WebBook. An example of this data can be seen in Figure 6.4. Each of the curves in this figure can be fitted by a polynomial; nitrogen and methane by a second-order polynomial, and carbon dioxide by a seventh-order polynomial curve.

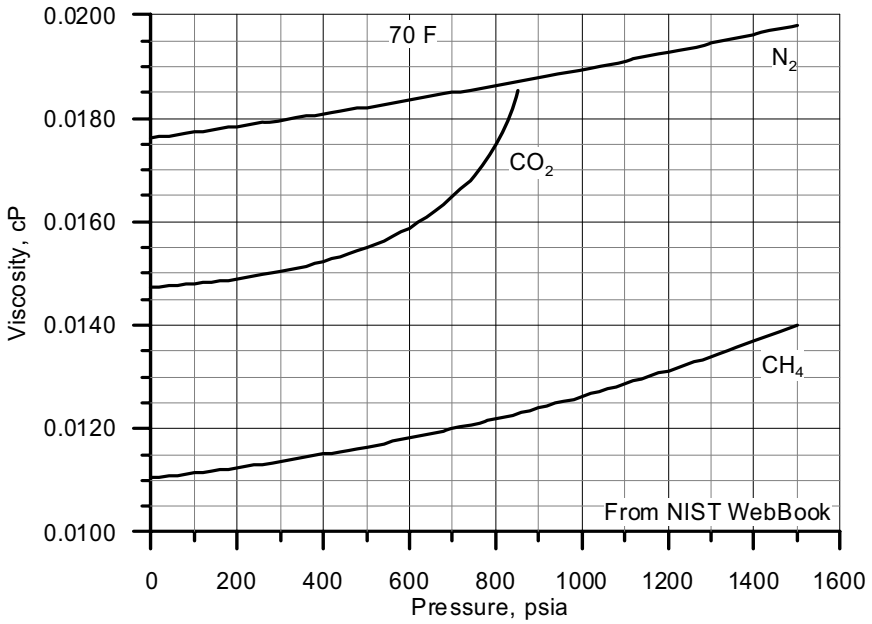

Figure 6.4. Example of viscosity data that can be obtained from the NIST web site [61].

Other plots showing viscosity as a function of temperature and pressure were prepared for each of these three gases and included in the laboratory notebook. An example of these plots is shown in Figure 6.5. Each viscosity isotherm curve was fitted with a polynomial and programmed into the LabView™ software used for data logging and calculation. Linear interpolation was used to obtain viscosities between viscosity isotherms. The calculated gas viscosity was then used in the coal permeability calculation.

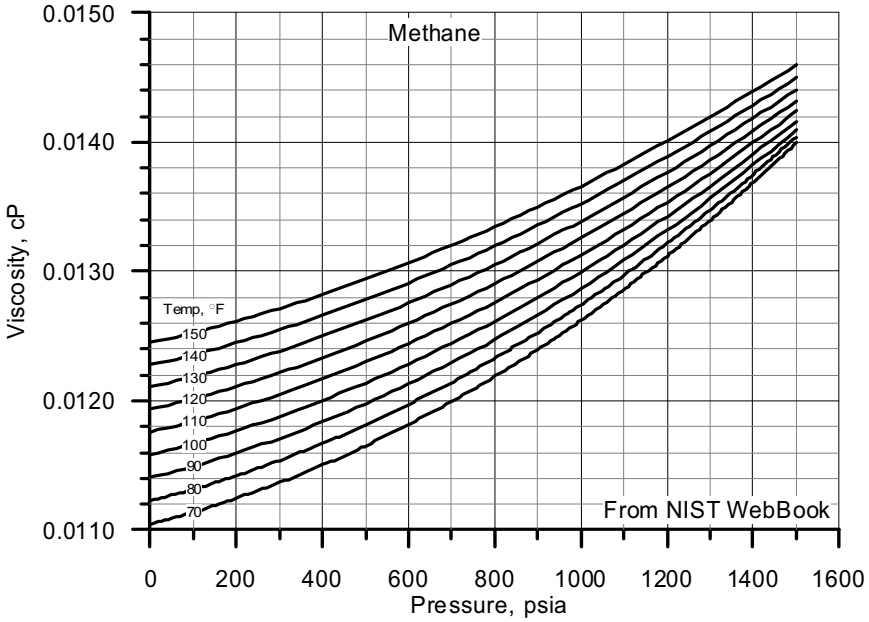

Figure 6.5. Viscosity of methane as a function of both pressure and temperature.

When mixtures of gases were used as the flowing fluid, the viscosity was calculated using the procedure set forth by Davidson [63] for calculating viscosities of gas mixtures. This method required knowledge of the mole fraction of each gas in the mixture, the molecular weight of each of the gases, and the viscosity of each component at the temperature and pressure of interest. To employ this method, Davidson calculates a momentum fraction for each component:

$$y_i = \frac{x_i \sqrt{M_i}}{\sum_{i=1}^{n} \left(x_i \sqrt{M_i} \right)}, \quad \text{(6-11)}$$

where y_i is the momentum fraction, x_i is the mole fraction of the gas in the mixture, M_i is the molecular weight, and n is the number of components in the gas mixture. Next, the efficiency of the momentum transfer was calculated for each of the three sets of possible

gas mixtures (nitrogen/carbon dioxide, nitrogen/methane, and methane/carbon dioxide) by the following equation:

$$E_{ij} = \frac{2\sqrt{M_i}\sqrt{M_j}}{M_i M_j}, \quad \text{(6-12)}$$

where E_{ij} is the momentum transfer efficiency between two gases i and j; and M_i and M_j are the molecular weights of the gases.

The fluidity of the gas mixture was then calculated by the following equation:

$$f_{mix} = \sum_{\substack{i,j=1 \\ \text{and } i \neq j}}^{n} \left(\frac{2 \cdot y_i y_j}{\sqrt{\mu_i}\sqrt{\mu_j}} E_{ij}^{1/3} \right) + \sum_{i=1}^{n} \left(\frac{y_i^2}{\mu_i} \right), \quad \text{(6-13)}$$

where f_{mix} is the fluidity of the gas mixture; μ_i and μ_j are the viscosities of the pure gas components, and n is the number of gas components in the mixture.

Finally, gas mixture viscosity is the reciprocal of fluidity:

$$\mu_{mix} = \frac{1}{f_{mix}}. \quad \text{(6-14)}$$

6.2.3 Experimental Procedure for Measuring Permeability

Coal cores used in the permeability experiments were cut under de-ionized water and stored immersed in sealed containers until needed. After removing a core from their sealed storage containers, it was surface dried, measured, wrapped with Teflon and aluminum foil to minimize gas leakage through the Viton sleeve covering the core, placed into the hydrostatic core holder set at 80° F (the same temperature as the strain experiments), and allowed to equilibrate for 24 hours inside the core holder with nitrogen flowing through at a low rate.

6.2.3.1 Method of Changing the Flowing Gas Between Permeability Experiments

During the course of the research, different gases were injected through coal cores, which were sorbed, causing changes in core permeability. Specifically, carbon dioxide, methane, nitrogen, and a gas mixture were tested. Each of these four gases was tested using the same coal core. When the time came to change gases between permeability experiments, helium was flushed through the core at a low rate for at least 24 hours to desorb any residual sorptive gas left in the core. If permeability was not stable by the end of 24 hours, then additional helium was flushed through the core until the permeability became stabile.

6.2.3.2 Discussion of Relationship between Net Stress and Pore Pressure

Hantush [64] stated that a change in pore pressure results in an equal and opposite change in effective stress. Walsh [65] gave the following general relationship between effective or net stress, σ, total stress, σ_t, and pore pressure, p_p:

$$\sigma = \sigma_t - s \cdot p_p . \quad (6\text{-}15)$$

where s was a constant for linearly elastic materials (such as coal). McKee et al. [66] used this relationship in their work on stress-dependent permeability in coals, but set 's' equal to unity with the caveat that this assumption might not be rigorously true. For lack of better information or evidence, the assumption made by McKee et al. was incorporated in this thesis and 's' in Eq (6-15) was assumed to equal to unity. McKee et al. also state that σ_t is a constant caused by the overburden. With these assumptions made, net stress can be defined as the difference between the overburden pressure and the pore pressure:

$$\sigma = p_{ob} - p_p . \quad (6\text{-}16)$$

The net stress condition used in the permeability experiments can be controlled by varying either overburden pressure or pore pressure, or both simultaneously.

6.2.3.3 Permeability Experiments while Varying Overburden Pressure

Achieving a repeatable permeability response was an important part of the preparation of the cores. The net stress was cycled from high to low and back again by varying the overburden pressure until permeability hysteresis was minimized or eliminated. To do this, the average pore pressure was set and held at a constant 100 psia and the overburden pressure was cycled from 1000 psia down to 300 psia and back up to 1000 psia while measuring permeability changes due to the change in net stress. The flow rate was adjusted as needed to keep the average pore pressure constant.

During the first overburden pressure cycling for a core, there would typically be quite a bit of hysteresis with the permeability data. However, additional overburden pressure cycles reduced the hysteresis until a repeatable permeability curve was obtained as a function of net stress (overburden pressure). Figure 6.6 shows the results of these core preparation permeability tests and shows the permeability hysteresis diminishing with repeated tests for the Anderson 01 core (a) and the Gilson 02 core (b).

6.2.3.4 Permeability Experiments while Varying Pore Pressure

Once the permeabilities of the cores were established and repeatable with a change in net stress, additional experiments were run where the overburden pressure was held constant and pore pressure was varied, allowing gases to be adsorbed or desorbed. In these experiments, the initial average pore pressure was set to about 100 psia and then increased incrementally until it reached about 800 psia. Because pore pressure was varied, gases were adsorbed or desorbed, and the effects of sorption-induced strain were manifest in the permeability results. Time was given for the gases to adsorb and permeability was monitored until a stabile value was achieved at each pressure increment. Data from these tests will be presented and discussed in Section 6.4 of this thesis.

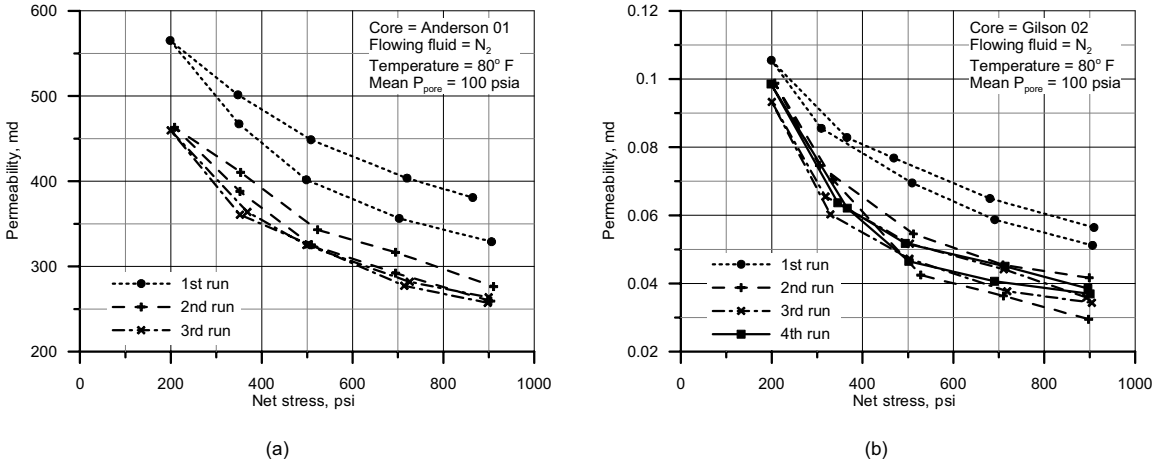

Figure 6.6. Results of core preparation permeability tests showing permeability hysteresis diminishing with repeated tests.

6.3 Description of Permeability Models

Three permeability models were selected from the literature to model the laboratory permeability data. Seidle and Huitt [28] published a permeability model in 1995, Palmer and Mansoori [23] published theirs in 1998, and Shi and Durucan [39] published their model in 2003.

A brief explanation of each of the models is laid out in the following paragraphs, but for comprehensive descriptions, please see the references for each model given in the preceding paragraph. Because experimental results of permeability measurements under certain conditions are used to calculate the initial porosities and fracture compressibilities of the cores used by the models, the models are discussed here before the presentation of the experimental results.

6.3.1 Seidle-Huitt Model

The derivation of this model begins with the assumption derived by Reiss [24] that the ratio of the observed permeability, k, to the initial permeability, k_0, is equal to the cube of the ratio of the observed porosity, ϕ, to the initial porosity, ϕ_0:

$$\frac{k}{k_0} = \left(\frac{\phi}{\phi_0}\right)^3 \quad \text{..... (6-17)}$$

The porosity ratio was given by Seidle and Huitt as

$$\frac{\phi}{\phi_0} = 1 + \left(1 + \frac{2}{\phi_0}\right) c_m V_m \left(\frac{p_0}{p_L + p_0} - \frac{p}{p_L + p}\right), \quad \text{..... (6-18)}$$

where $c_m V_m$ is equivalent to the Langmuir strain constant S_{max} as defined in this thesis. Rewriting this equation results in the Seidle-Huitt equation for permeability ratio that can be used to model the laboratory-generated permeability data:

$$\frac{k}{k_0} = \left[1 + \left(1 + \frac{2}{\phi_0}\right) S_{max} \left(\frac{p_0}{p_L + p_0} - \frac{p}{p_L + p}\right)\right]^3 . \quad \text{..... (6-19)}$$

This model is a function of initial porosity, the Langmuir strain curve constants, and pressure; and it neglects the elastic properties of coal and specifies that all permeability changes are caused by sorption-induced strain.

Model formulation was validated by comparing the calculated results from Eq (6-19) with the model output reported in the authors' paper. Figure 6.7 shows this comparison. The resulting fit is very good, which validates the formulation of the model used for this study.

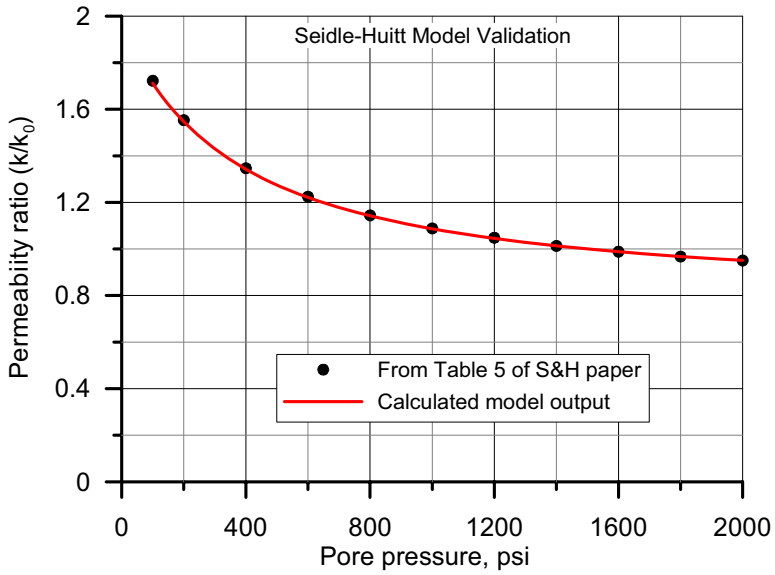

Figure 6.7. Seidle-Huitt model validation plot showing calculated model output compared to tabulated results from Table 5 of Seidle and Huitt [28].

6.3.2 Palmer-Mansoori Model

This is perhaps the most widely discussed permeability model in the literature. Other models are based on it such as the model published by Chikatamarla and Bustin [30] in 2004, which can be shown to be equivalent to the Palmer-Mansoori model. As with the Seidle-Huitt model, the Palmer-Mansoori model also assumes Reiss's cubic relationship between permeability and porosity for fractured media. The porosity-change equation for this model was given by Palmer and Mansoori as:

$$\frac{\phi}{\phi_0} = 1 - \frac{1}{M\phi_0}(\sigma - \sigma_0) + \frac{\varepsilon}{\phi_0}\left(\frac{K}{M} - 1\right)\left(\frac{p}{P_L + p} - \frac{p_0}{P_L + p_0}\right). \quad \text{(6-20)}$$

where M is the constrained axial modulus, K is the bulk modulus, and ε is the volumetric Langmuir strain constant. The constrained axial modulus [23] and the bulk modulus [67] can be rewritten in terms of Young's modulus and Poisson's ratio:

$$M = \frac{E(1-\nu)}{(1+\nu)(1-2\nu)} \quad \text{and} \quad K = \frac{E}{3(1-2\nu)}, \qquad (6\text{-}21)$$

where E is Young's modulus and ν is Poisson's ratio.

Recall that the volumetric strain was shown to be equal to three times the linear strain:

$$\varepsilon = 3S_{max} \qquad (6\text{-}22)$$

Substituting Eq (6-21) and Eq (6-22) into Eq (6-21) yields the Palmer-Mansoori permeability equation in terms of Young's modulus, Poisson's ratio, initial porosity, the Langmuir strain curve parameters, and pressure:

$$\frac{k}{k_0} = \left[1 - \frac{(1+\nu)(1-2\nu)}{E(1-\nu)}\frac{(\sigma-\sigma_0)}{\phi_0} + \frac{S_{max}}{\phi_0}\left(\frac{(1+\nu)}{1-\nu} - 3\right)\left(\frac{p}{p_L+p} - \frac{p_0}{p_L+p_0}\right)\right]^3 \qquad (6\text{-}23)$$

All parameters in this equation can be either measured or approximated except the initial porosity. However, initial porosity can be obtained by fitting the above equation to permeability data unaffected by sorption-induced strain and is discussed in Section 6.4.1 .

Model formulation was validated by comparing the calculated results from Eq (6-23) with the model output reported in the authors' paper. Figure 6.8 shows this comparison. The resulting fit is very good, which validates the formulation of the model used for this study.

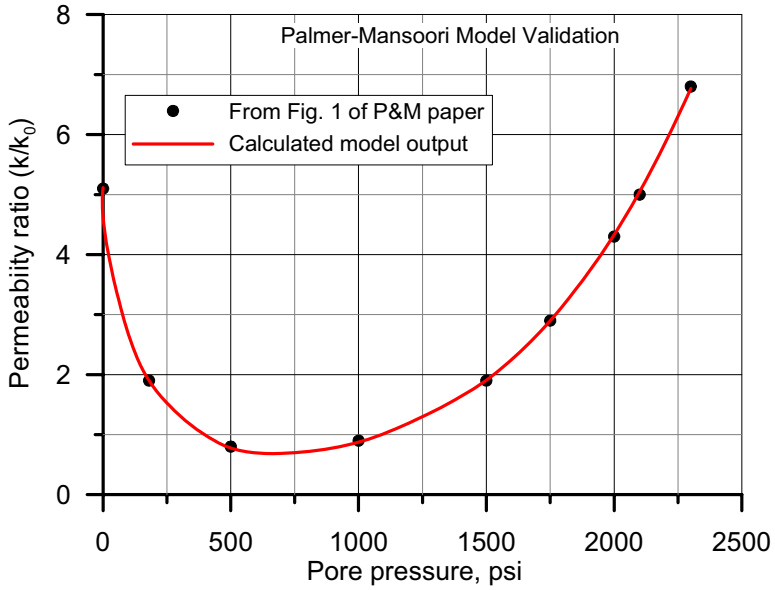

Figure 6.8. Palmer-Mansoori model validation plot showing calculated model output compared to data read from Fig. 1 of Palmer and Mansoori [23].

6.3.3 Shi-Durucan Model

The derivation of the Shi-Durucan permeability model begins with a permeability equation given by Seidle et al. [22] as:

$$\frac{k}{k_0} = \exp\left[-3C_f(\sigma - \sigma_0)\right], \quad \text{(6-24)}$$

where C_f is the fracture compressibility, and σ is the effective (net) stress. Shi and Durucan then derive an expression for the change in effective stress:

$$\sigma - \sigma_0 = \frac{\nu}{1-\nu}(\sigma - \sigma_0) + \frac{E}{3(1-\nu)}\varepsilon\left(\frac{p}{p_L + p} - \frac{p_0}{p_L + p_0}\right). \quad \text{(6-25)}$$

Noting that the volumetric strain, ε, is three times the linear strain and combining the two above equations results in a permeability equation that takes into account sorption-induced strain effects:

$$\frac{k}{k_0} = \exp\left\{-3C_f\left[\frac{\nu}{1-\nu}(\sigma-\sigma_0)+\frac{E}{(1-\nu)}S_{max}\left(\frac{p}{P_L+p}-\frac{p_0}{P_L+p_0}\right)\right]\right\}. \quad \text{(6-26)}$$

Model formulation was validated by comparing the calculated results from Eq (6-26) with the model output reported in the authors' paper. Figure 6.9 shows this comparison. The resulting fit is very good, which validates the formulation of the model used for this study.

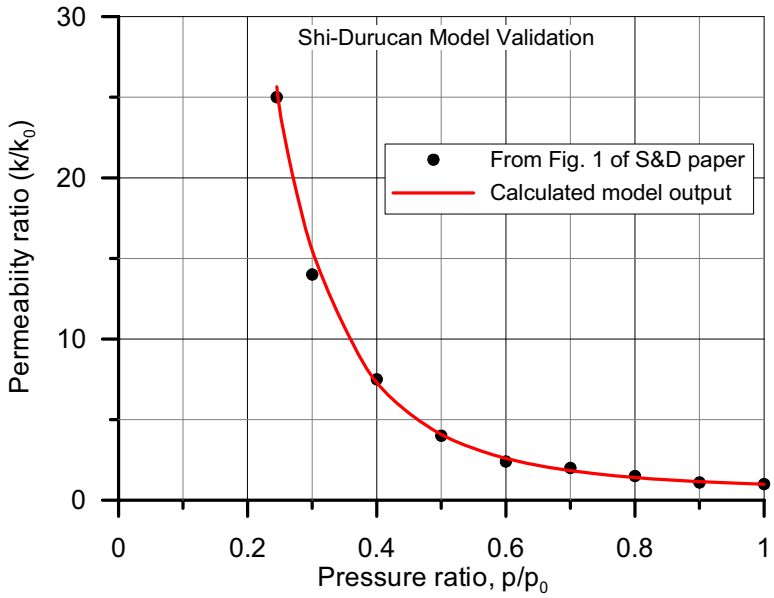

Figure 6.9. Shi-Durucan model validation plot showing calculated model output compared to data read from Fig. 1 of Shi and Durucan [39].

All variables in this equation either can be measured or are approximated except for the fracture compressibility, C_f. Fracture compressibility is not necessarily constant but often a function of net stress. McKee et al. [66] offered the following expression for stress dependent, variable fracture compressibility:

$$C_f = \frac{C_0}{\alpha(\sigma - \sigma_0)}\{1 - \exp[-\alpha(\sigma - \sigma_0)]\}. \quad \text{(6-27)}$$

where C_0 is the initial fracture compressibility and α is the fracture compressibility change rate. Substituting this term into the permeability equation yields an expression for the Shi-Durucan permeability model in terms of fracture compressibility, Young's modulus, Poisson's ratio, the Langmuir strain curve parameters, and pressure:

$$\frac{k}{k_0} = \exp\left\{\frac{-3C_0\{1 - \exp[-\alpha(\sigma - \sigma_0)]\}}{\alpha(\sigma - \sigma_0)}\left[\frac{\nu(\sigma - \sigma_0)}{1 - \nu} + \frac{E \cdot S_{max}}{(1 - \nu)}\left(\frac{p}{P_L + p} - \frac{p_0}{P_L + p_0}\right)\right]\right\}. \quad \text{(6-28)}$$

Values for C_0 and α are unique for each coal core, but can be obtained by fitting the above equation to permeability data unaffected by sorption-induced strain (discussed later in Section 6.4.1).

6.4 Permeability Experimental Results using Pure Gases

Results of the permeability tests are shown as plots of k/k_0 versus pressure. Two cores representing two different coal types and three different gases (CO_2, CH_4, and N_2) with different sorption-induced strain characteristics were used to obtain the permeability data.

Poisson's ratio and Young's modulus are two of the elastic properties of coal that are needed in order to model the permeability data of coal. Literature values for Poisson's ratio [22, 23, 39] range from 0.2 to 0.5 for coal. For this work, an average value of 0.35

was assumed. Literature values for Young's modulus [23, 39] range from 124,000 psi to 500,000 psi for coal; and for this work, a value of 200,000 psi was assumed.

6.4.1 Permeability Results: Varying Overburden Pressure

A series of experiments were conducted where confining (overburden) pressure was varied while holding pore pressure constant (100 psia) with nitrogen as the flowing fluid as described earlier. The initial overburden pressure was 1000 psia, which gives the initial stress equal to 900 psi using Eq (6-16). The initial condition of high net stress was selected based on plotting preferences and not tied to any physical reference.

The experiments where overburden pressure was varied were used to calculate the initial porosity and fracture compressibility constants for each coal core and are reported later in this paper. Because pore pressure was held constant in these experiments, there were no sorption-induced permeability effects, and any gas presumably could have been used with the same results.

To calculate initial porosity and fracture compressibility constants associated with the three permeability models, the initial porosity and fracture compressibility constants were varied until a best fit of the permeability data was obtained.

The Seidle-Huitt model is formulated such that if there is no sorption-induced strain (as was the case in this set of experiments), there would be no change in permeability, and the permeability ratio would be equal to unity; therefore, this model could not be used to obtain a value for initial porosity. However, the Palmer-Mansoori and Shi-Durucan models can be used to account for changing overburden pressure and were used to obtain initial porosity and fracture compressibility constants. Because the Seidle-Huitt model could not be used to analyze this data set, the Seidle-Huitt initial porosity was set equal to the initial porosity obtained for the Palmer-Mansoori model.

6.4.1.1 Varying Overburden Pressure: Anderson 01 Core Permeability Data

For the Anderson 01 core, permeability changes resulting from varying the overburden pressure are shown in Figure 6.10. Along with the actual permeability data, the Palmer-Mansoori and Shi-Durucan models are shown. Because pore pressure was held constant, sorption-induced strain was eliminated, which allowed these data to be used to calculate the initial porosity and the fracture compressibility constants. These properties of the cores are required by the models in order to be used when pore pressure and sorption-induced strain do affect permeability.

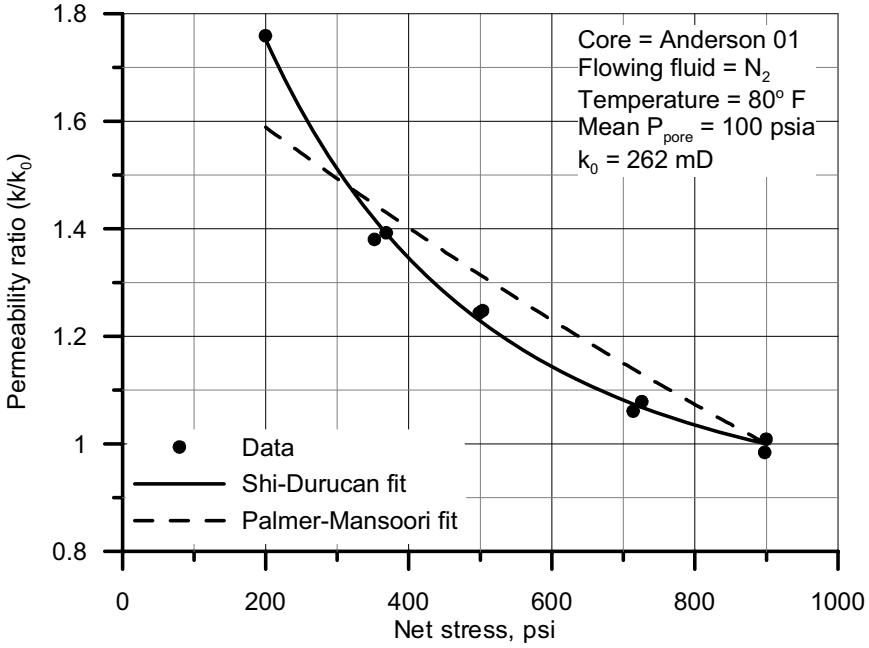

Figure 6.10. Permeability changes of the Anderson 01 core as a function of net stress.

Both of these models were forced to a best-fit of the data by varying either the initial core porosity or the core fracture compressibility constants until error was minimized using a least squares process. The calculated initial porosity (using the Palmer-Mansoori

model) was 1.31% and the calculated fracture compressibility constants, C_0 and α (using the Shi-Durucan model) were 1.88E-4 psi^{-1} and 24.3E-4 psi^{-1} respectively.

6.4.1.2 Varying Overburden Pressure: Gilson 02 Core Permeability Data

For the Gilson 02 core, permeability changes resulting from varying the overburden pressure are shown in Figure 6.11. Again, two of the models were forced to a best-fit of the data by varying initial porosity and fracture compressibility constants. The calculated initial porosity (using the Palmer-Mansoori model) was 0.804% and the calculated fracture compressibility constants, C_0 and α (using the Shi-Durucan model) were 1.69E-4 psi^{-1} and 37.5E-4 psi^{-1} respectively.

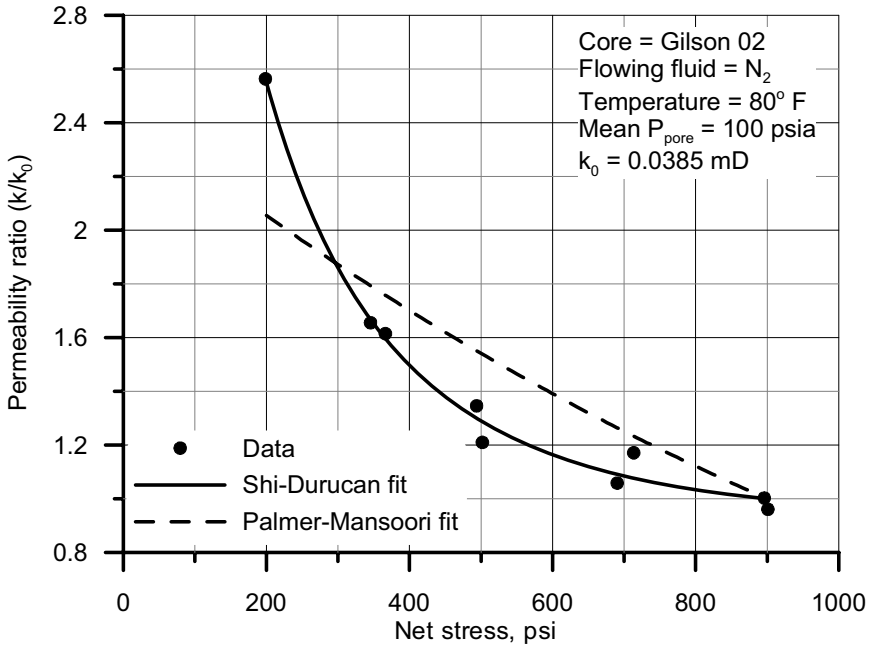

Figure 6.11. Permeability changes of the Gilson 02 core as a function of net stress.

Considering the wide difference in permeabilities of these two cores, the calculated fracture compressibility constants and initial porosities of these cores were remarkably similar. Table 6.1 summarizes the core properties for both the Anderson 01 core and the Gilson 02 core.

Table 6.1. Properties of coal cores used in permeability experiments

	Anderson 01	Gilson 02
Rank	Subbituminous	High-volatile bituminous
Vitrinite reflectance, V_r (%)	0.24	0.53
Initial permeability, k_0 (mD)	262	0.0385
Initial porosity, ϕ_0 (%)	1.31	0.804
Average fracture compressibility, C_f, (psi^{-1})	4.17E-4	6.59E-4
Initial fracture compressibility, C_0 (psi^{-1})	1.88E-4	1.69E-4
Fracture compressibility change rate,α (psi^{-1})	24.3E-4	37.5E-4

The values for average fracture compressibility, C_f, obtained in this work (see Table 6.1) both fall near the lower range of literature values reported for other coals [22, 66], which range from 4.28E-4 psi^{-1} to 18.7E-4 psi^{-1}. The values of compressibility change rate, α, for these two coal cores (see Table 6.1) compare very closely to a literature value [66] for coal in the Piceance basin equal to 29.5E-4 psi^{-1}.

6.4.2 Permeability Results: Varying Pore Pressure

Another series of experiments was conducted where pore pressure was varied while holding constant the confining pressure at 1000 psia. Again, high net stress was selected as the starting point for initial stress condition to be consistent with the varied overburden pressure tests, which required the initial pore pressure to be low. Because pore pressure

was varied, sorption of gases and the resulting strain was expected to affect the permeability of each of the cores to a different degree depending on the sorbing gas.

During these experiments, adsorption of gases caused by changes in the pore pressure affected the permeability results and some time was allowed to reach equilibrium as mentioned in Section 6.2.3.4 . Figure 6.12 is an example of these experiments showing the monitoring of permeability values with respect to time. Permeability was monitored in real time and pressure was changed only after equilibration of the permeability values. Permeability was measured for five different pore pressures, but the permeability values were recorded continuously for only three of these pressure regimes. In the other two pressure regimes (307 psia and 487 psia), permeability was monitored on the computer screen, but recorded sparingly. Contrary to the straight line connecting recorded data points (indicating an unequilibrated permeability), if the data had been recorded the permeability values in these two pressure regimes would actually appear much flatter before increasing the pressure to the next step. In retrospect, continuous permeability data should have been recorded for the entire duration of the experiments; however, that oversight should in no way invalidate the results of the experiments.

6.4.2.1 Varying Pore Pressure: Anderson 01 Core Permeability Data

Results of varying pore pressure and gas composition for the Anderson 01 coal core are shown in Figure 6.13. Initial permeabilities, k_0, for all the gases were measured at pore pressures of about 100 psia and are shown in the figure. Even though the same core was used for this set of experiments, the initial permeabilities for each of the gases were different because of the varying amount of sorption-induced strain caused by each of the gases (see Figure 5.1). As expected, adsorption of carbon dioxide resulted in the lowest initial permeability (86 mD) for the three gases, followed by methane (147 mD), and nitrogen adsorption resulted in the highest initial permeability (257 mD).

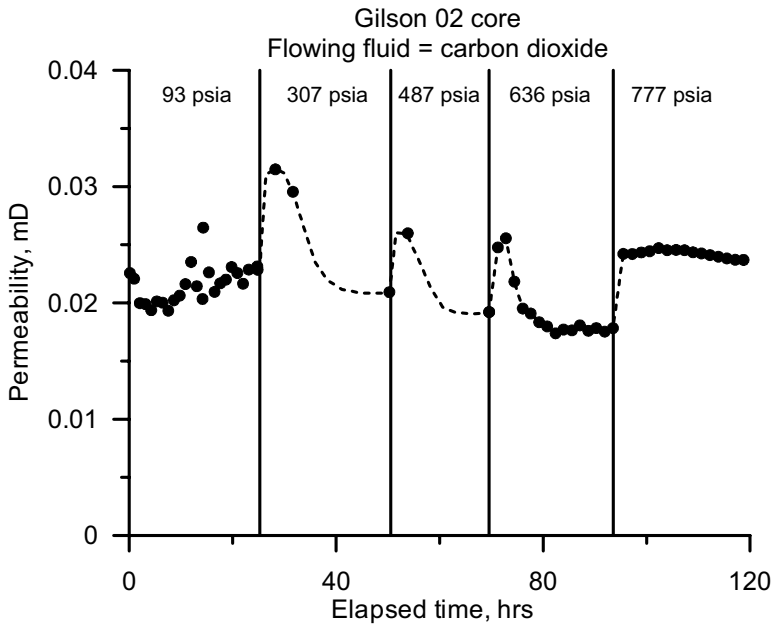

Figure 6.12. Gilson 02 coal core raw permeability results showing the equilibration of permeability with respect to time.

The nitrogen permeability ratio data generally increased as pore pressure increased, signifying very little effect of sorption-induced strain. Increasing the pore pressure (decreasing the net stress) with nitrogen as the flowing fluid increasingly opened the fractures and increased permeability.

The permeability results were different for both methane and carbon dioxide than the nitrogen results. As pore pressure increased, the permeability initially decreased with these two gases because of larger sorption-induced strain for these gases compared with nitrogen. Then as pore pressure continued to increase, the permeability also increased because the effect of sorption-induced strain was overcome by the opposite-acting strain caused by the elastic properties of the coal at higher pore pressures.

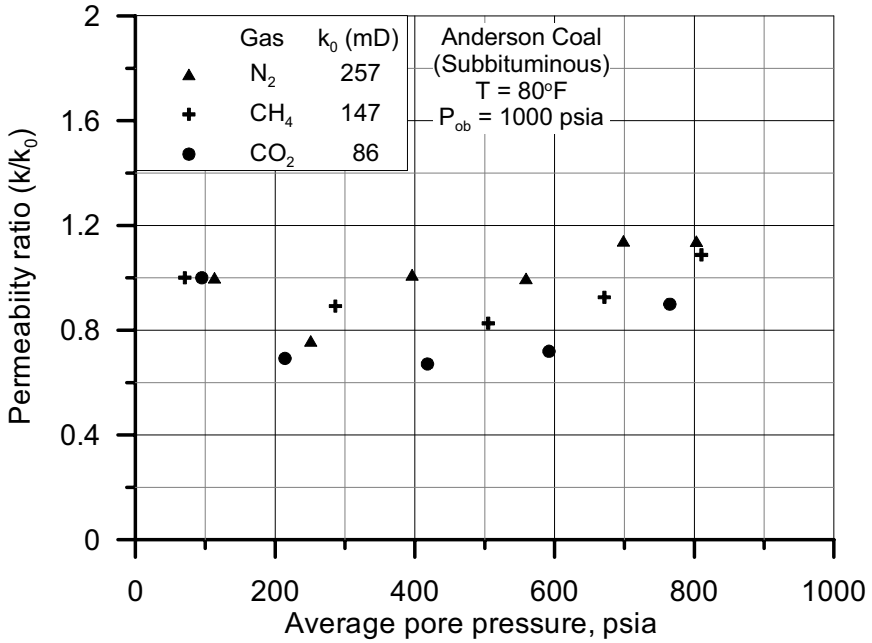

Figure 6.13. Permeability as a function of pore pressure for three gases using the Anderson 01 coal core.

6.4.2.2 Varying Pore Pressure: Gilson 02 Core Permeability Data

Results of varying pore pressure and gas composition for the Gilson 02 coal core are shown in Figure 6.14. As with the Anderson 01 core, adsorption of carbon dioxide resulted in the lowest initial permeability (0.0226 mD) for the three gases, followed by methane (0.0289 mD), and nitrogen adsorption resulted in the highest initial permeability (0.0372 mD).

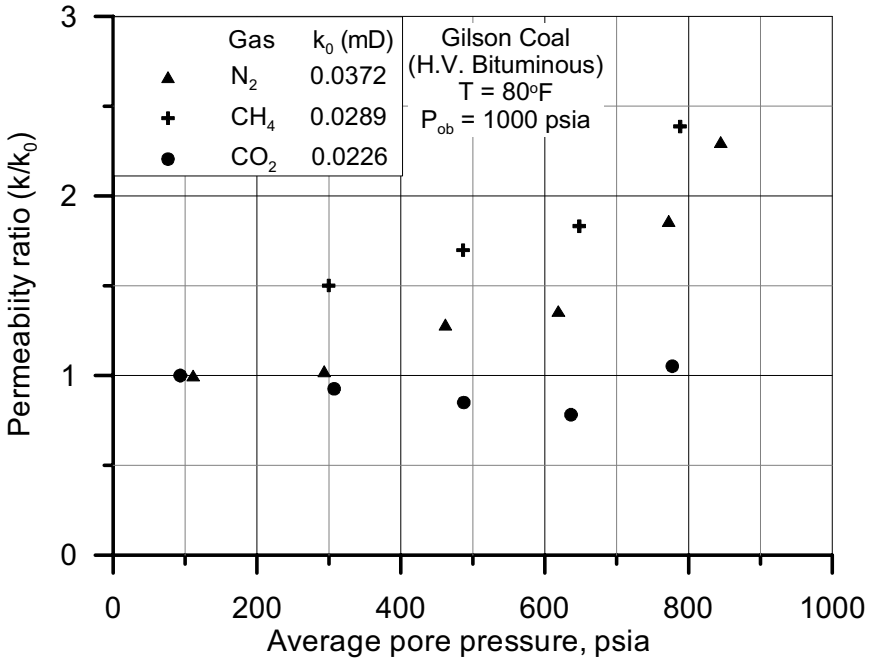

Figure 6.14. Permeability as a function of pore pressure for three gases using the Gilson 02 coal core.

The effect of sorption-induced strain was much less with the Gilson core compared to the Anderson core. This can be attributed to the lower sorption-induced strains associated with the Gilson coal as seen in Figure 5.1. Carbon dioxide was the only gas that caused enough sorption-induced strain to decrease the permeability as pore (sorption) pressure increased. The sorption of both methane and nitrogen had very little effect on the permeability. The change in permeability with methane and nitrogen for this core can almost entirely be attributed to the cleat compressibility and elastic properties of the coal. For example, the sorption-affected permeability data for nitrogen in Figure 6.14 is very similar to the permeability data in Figure 6.11, in which there was no gas sorption.

6.5 Modeling Sorption-Induced Permeability Changes for Pure Gases: Results

The three permeability models discussed earlier were applied to the data shown in Figure 6.13 and Figure 6.14 to determine the ability of the models to match permeability data affected by sorption-induced strain. The initial porosities and fracture compressibility constants shown in Table 6.1 as well as the sorption-induced strain constants listed in Table 5.2 were used with the respective models to generate the model output. The plots in Figure 6.15 show the model output along with the original permeability data.

6.6 Discussion of Modeling of Permeability Data

Overall, none of the three coal permeability models did a very good job matching the actual laboratory-generated permeability data for every case. However, two of the models were relatively better at matching the nitrogen permeability data.

6.6.1 Seidle-Huitt Model

The Seidle-Huitt model was designed to predict permeability changes as pore pressure decreased from an initial reservoir pressure towards some lower abandonment pressure as the reservoir was produced. For this research, the pore pressure was initially low and then was increased. As written, this model specifies that if pore pressure decreased, permeability would always increase; and if pore pressure increased, permeability would always decrease – potentially to negative values. This predicted permeability behavior is not valid because it does not allow for increasing permeability at higher pore pressure as the data indicate (see Figure 6.15). As a result, this model has a limited range of application.

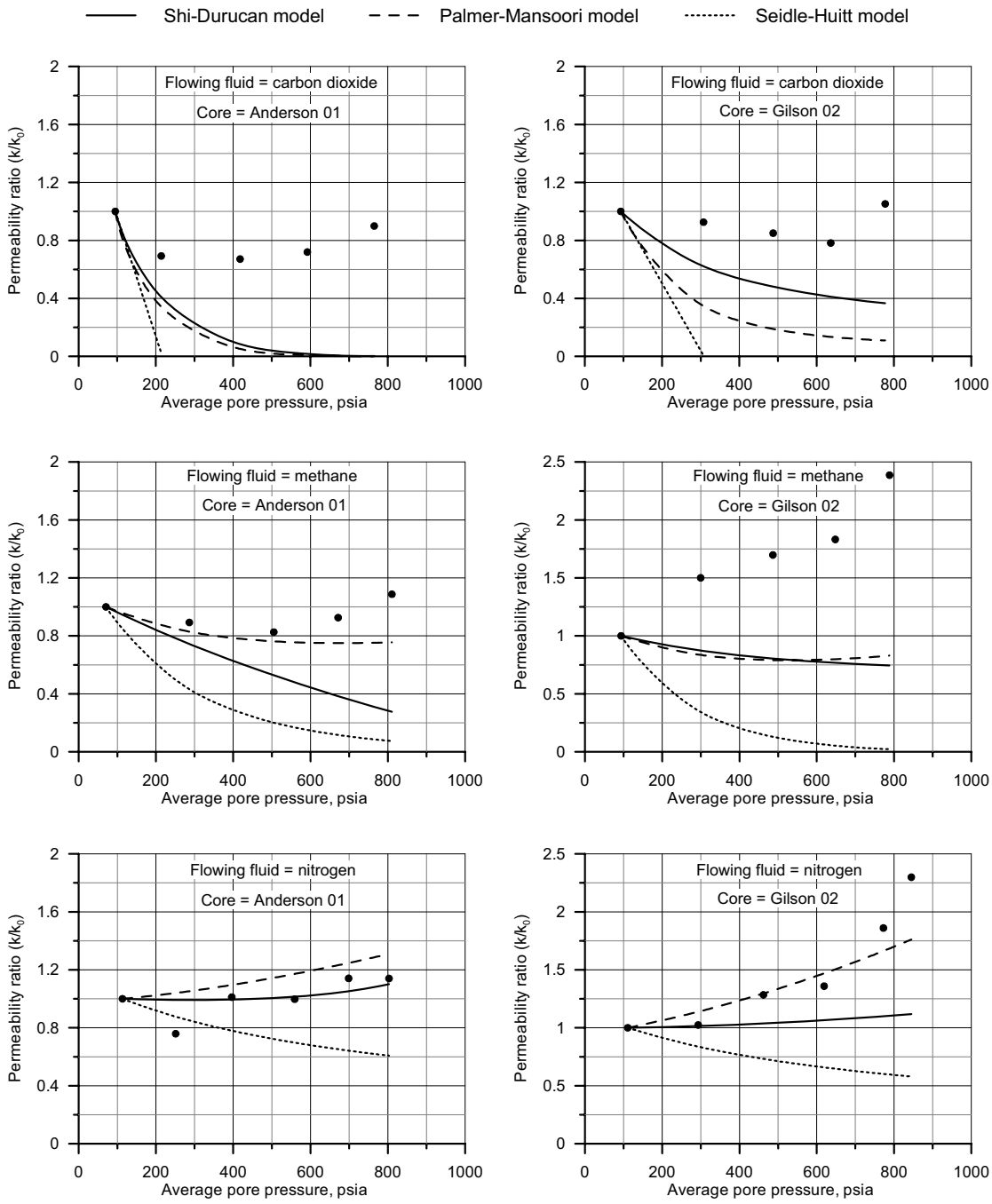

Figure 6.15. Model results compared to permeability data. Confining pressure was 1000 psia and temperature was 80° F.

Because the Seidle-Huitt model neglects the elastic properties of the coal it appears to oversimplify the mechanics of permeability changes in coal as pore pressure changes and gases are sorbed.

6.6.2 Palmer-Mansoori Model

The Palmer-Mansoori model appears to capture many of the trends associated with permeability changes in coal influenced by sorption-induced strain. However, for gases that caused large adsorption strains, this model significantly overestimated the decline in permeability (see Figure 6.15). The Palmer-Mansoori model, as with the Seidle-Huitt model, also has the capability to calculate negative permeability ratios, and interpretive care should be used to not take calculated negative values literally.

6.6.3 Shi-Durucan Model

This model also appears to match some permeability data well, but not all (see Figure 6.15). As with the Palmer-Mansoori model, the Shi-Durucan model tends to overestimate the impact of large sorption-induced strain on permeability. However, with low sorption-induced strain gases, this model is comparable to the Palmer-Mansoori model. In addition, this model is formulated in such a way that the permeability ratio is always greater than zero, which more accurately describes actual permeability data than the other two models.

6.7 Incorporating Extended Langmuir Theory to Model Permeability Changes in Coal Induced by Sorption of Gas Mixtures

Although methane is most generally the most prevalent gas produced from coal beds, there are other gases present as discussed in Section 1.4 of this thesis. This chapter dis-

cusses the calculation of permeability changes due to adsorbing or desorbing gas mixtures through the implementation of the extended Langmuir equation to two permeability-change models, and compares predicted results with measured permeability data with a gas mixture as the flowing fluid.

6.7.1 Permeability Models for Gas Mixtures

Reservoir simulators need to be able to calculate the amount of strain resulting from the sorption of an infinite variety of mixtures of gases as injection fronts pass and gases are sorbed and desorbed throughout enhanced recovery projects. Even though the collection of sorption-induced coal strain for pure gases and gas mixtures has been made dramatically easier and more rapid by this research, measuring the strain induced by the sorption of all possible gas mixtures is impractical. However, measuring the strain induced by the sorption of a number of pure gases for a wide variety of coals can now be easily and quickly accomplished compared to previous methods. Showing that coal strain induced by the sorption of pure gases can be used to predict the strain induced by the sorption of mixed gases would be a significant step forward in the development of adequate coal permeability-change equations used to simulate ECBM or CO_2 sequestration projects in coal.

In Section 5.2 , the application of extended Langmuir theory to account for mixed-gas adsorption was discussed. Two equations were presented: one based solely on the strain constants of the pure gas strain curves and the composition of the gas mixture – called the "simple extended Langmuir equation"; and the other adding in the gas interaction energies – called the "interaction extended Langmuir equation." Including these two equations into the Palmer-Mansoori and the Shi-Durucan models is discussed in the following sections.

6.7.1.1 Implementing the Simple Extended Langmuir Equation

The simple extended Langmuir equation, used to calculate the strain induced by the sorption of gas mixtures based on data provided by the strain induced by the sorption of pure gases was described earlier in Section 5.2 , and is rewritten here:

$$S_{mix} = \frac{p\sum_{i=1}^{n}\left(\frac{S_{max}\,y}{p_L}\right)_i}{1+p\sum_{i=1}^{n}\left(\frac{y}{p_L}\right)_i}, \quad \text{..... (6-29)}$$

This equation requires knowledge of the strain constants of the gas mixtures, the mole fractions of the gas components, and the observed pressure.

Inserting Eq (6-29) into the previously derived Palmer-Mansoori model, Eq (6-23), results in the following permeability equation capable of predicting permeability changes in coal induced by sorption of mixed gases:

$$\frac{k}{k_0} = \left[1 - \frac{(1+\nu)(1-2\nu)\Delta\sigma}{E(1-\nu)\phi_0} + \frac{1}{\phi_0}\left(\frac{1+\nu}{1-\nu} - 3\right)\left(\frac{p\sum_{i=1}^{n}\left(\frac{S_{max}\,y}{p_L}\right)_i}{1+p\sum_{i=1}^{n}\left(\frac{y}{p_L}\right)_i} - \frac{p_0\sum_{i=1}^{n}\left(\frac{S_{max}\,y}{p_L}\right)_i}{1+p_0\sum_{i=1}^{n}\left(\frac{y}{p_L}\right)_i}\right)\right]^3 \text{..... (6-30)}$$

Making the same modifications to the Shi-Durucan model, Eq (6-28), results in the following equation for sorption of gas mixtures:

$$\frac{k}{k_0} = \exp\left\{\frac{3C_0\{1-\exp[-\alpha\Delta\sigma]\}}{-\alpha\Delta\sigma}\left[\frac{\nu\Delta\sigma}{1-\nu} + \frac{E}{1-\nu}\left(\frac{p\sum_{i=1}^{n}\left(\frac{S_{max}\,y}{p_L}\right)_i}{1+p\sum_{i=1}^{n}\left(\frac{y}{p_L}\right)_i} - \frac{p_0\sum_{i=1}^{n}\left(\frac{S_{max}\,y}{p_L}\right)_i}{1+p_0\sum_{i=1}^{n}\left(\frac{y}{p_L}\right)_i}\right)\right]\right\} \text{..... (6-31)}$$

6.7.1.2 Implementing the Interaction Extended Langmuir Equation

The interaction extended Langmuir equation that incorporates gas interaction energies described in Section 5.2 is rewritten here:

$$S_{mix} = \frac{p\sum_{i=1}^{n}\left(\frac{S_{max}\,y}{\eta p_L}\right)_i}{1+p\sum_{i=1}^{n}\left(\frac{y}{\eta p_L}\right)_i}, \quad \text{(6-32)}$$

Section 5.2 showed that the above equation is a little more accurate than Eq (6-29) for predicting strain from mixed gases, but requires additional information regarding the gas interaction energies. Recall that in Section 5.2 the optimal values for η_{N2} and η_{CO2} were determined to be 0.25 and 0.58 respectively.

Inserting Eq (6-32) into the previously derived Palmer-Mansoori model, Eq (6-23), results in the following permeability equation capable of predicting permeability changes in coal induced by sorption of mixed gases:

$$\frac{k}{k_0} = \left[1 - \frac{(1+\nu)(1-2\nu)\Delta\sigma}{E(1-\nu)\phi_0} + \frac{1}{\phi_0}\left(\frac{1+\nu}{1-\nu} - 3\right)\left(\frac{p\sum_{i=1}^{n}\left(\frac{S_{max}\,y}{\eta p_L}\right)_i}{1+p\sum_{i=1}^{n}\left(\frac{y}{\eta p_L}\right)_i} - \frac{p_0\sum_{i=1}^{n}\left(\frac{S_{max}\,y}{\eta p_L}\right)_i}{1+p_0\sum_{i=1}^{n}\left(\frac{y}{\eta p_L}\right)_i}\right)\right]^3 \quad \text{(6-33)}$$

Making the same modifications to the Shi-Durucan model, Eq (6-28), results in the following equation for sorption of gas mixtures:

$$\frac{k}{k_0} = \exp\left\{\frac{3C_0\{1-\exp[-\alpha\Delta\sigma]\}}{-\alpha\Delta\sigma}\left[\frac{\nu\Delta\sigma}{1-\nu} + \frac{E}{1-\nu}\left(\frac{p\sum_{i=1}^{n}\left(\frac{S_{max}\,y}{\eta p_L}\right)_i}{1+p\sum_{i=1}^{n}\left(\frac{y}{\eta p_L}\right)_i} - \frac{p_0\sum_{i=1}^{n}\left(\frac{S_{max}\,y}{\eta p_L}\right)_i}{1+p_0\sum_{i=1}^{n}\left(\frac{y}{\eta p_L}\right)_i}\right)\right]\right\}. \quad \text{(6-34)}$$

6.7.2 Comparison of Models to Mixed-Gas Strain Data

Langmuir strain constants generated by the sorption of pure gases along with gas interaction energies and gas mole fractions were used with Eqs (6-30), (6-31), (6-33), and (6-34) to generate expected permeability changes induced by adsorbing a mixed gas stream. Calculated mixed-gas permeability was compared with measured mixed-gas permeability in Figure 6.16.

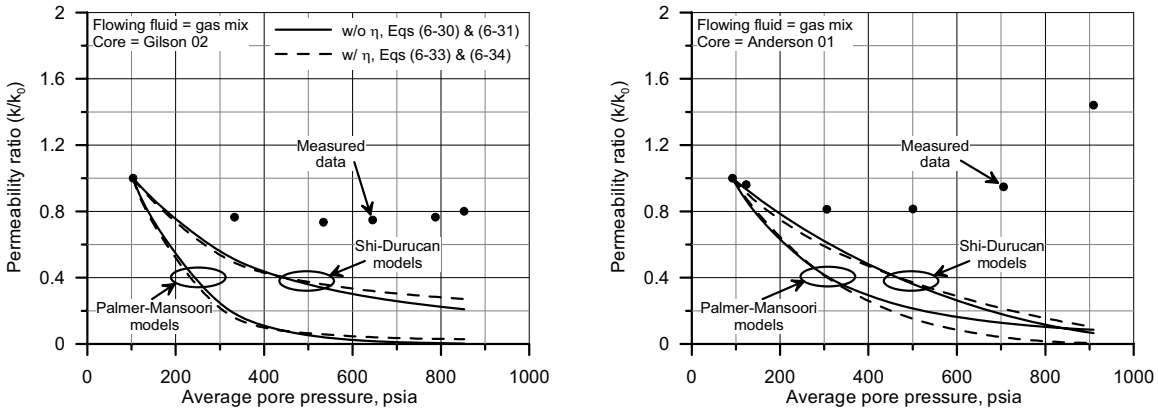

Figure 6.16. Mixed-gas model comparison for Gilson 02 and Anderson 01 cores.

As can be seen from the above figure, there is very little difference in predicted permeability between models including the interaction energy constants (η) and the models that neglect them. This is important because although the inclusion of the interaction energies results in a much better match of strain induced by the sorption of mixed gases (see Figure 5.10), the need to include the interaction energies is lost when modeling permeability changes caused by gas sorption.

Although the models do not appear to benefit from the inclusion of interaction energies associated with sorption of mixed gases, neither the Shi-Durucan model nor the

Palmer-Mansoori accurately predicts mixed-gas permeability changes in coal based on pure gas sorption constants alone.

6.8 Application of Correction Factor to Strain Constants

Generally, both the Shi-Durucan model and the Palmer-Mansoori model underestimated the permeability ratio for the six data sets, which could be 1) the result of incorrect model formulation, 2) caused by inappropriate strain data, or 3) the result of inaccurate permeability data. Of these three options, the second – inappropriate strain data – appeared the most probable for reasons discussed below.

Harpalani and Zhao, [68] Harpalani and Schraufnagel, [27] and Levine [29] all have reported sorption-induced strain data in coal using unconstrained coal samples, meaning that the coal samples were allowed to expand in all three directions without applying any external constraining forces. Gray [26] specifically states that unconstrained sorption-induced strain data are appropriate for use in his coal permeability model: "the strain derived from testing samples of coal that are free to move in all directions . . . can be directly used in calculations where strain is related to varying equivalent sorption pressure." Although other modelers [23, 35, 36, 39] did not specifically state that unconstrained strain data was appropriate for use in their models, they did cite the unconstrained strain data referenced above, which leads to the conclusion that they also intended unconstrained strain data to be employed in their permeability models.

The data shown in Figure 6.15, where measured permeability is compared to model-calculated permeability, indicate that there is less of an impact of sorption-induced strain occurring during the permeability experiments than that predicted by the models using the measured strain constants. However, because both the Palmer-Mansoori and the Shi-Durucan models accurately model permeability changes unaffected by gas sorption, it appears that the models' formulations are correct.

The use of unconstrained sorption-induced strain data in permeability equations designed to model constrained (by overburden pressure) flow tests appears to be somewhat inconsistent. Unconstrained sorption-induced strain data are easily measured; however, the use of these data in equations designed to model permeability changes with external forces being applied may be in error and the unconstrained data may need to be modified to account for the constrained nature of the flow tests.

By simply multiplying the strain data by some constant factor, the models could be forced to run through the permeability data; however, the shape of the resulting modeled permeability curve did not conform to the data very well, which implied that a variable strain factor dependent on pore pressure was needed.

Following this idea of modifying the strain data through the use of a variable strain factor, a variable strain factor that depends on the net stress and the pore pressure that has the following form was found to fit the permeability data more closely:

$$S_f = \frac{p_{ob}}{p_p} X, \quad \text{(6-35)}$$

where p_{ob} is the overburden pressure (psi), p_p is the pore pressure (psi), and X represents some factor and was determined by fitting the model output to the permeability data using a least squares analysis. This factor was different for each permeability data set.

For both the Palmer-Mansoori and the Shi-Durucan models, a grouping of pertinent strain, coal, and gas parameters was found to have a very good linear relationship with the calculated values for X. The resulting linear relationship was determined to be:

$$X = a + b\left(\frac{p_L}{S_{max} V_r^{\,2} \sqrt{\gamma}}\right), \quad \text{(6-36)}$$

where p_L and S_{max} are the Langmuir strain parameters, V_r is the percent vitrinite reflectance for a particular coal, and γ is the specific gravity of the sorbed gas. The constants 'a' and 'b' in the above equation were unique for each of the two models. For the Shi-

Durucan model the values for 'a' and 'b' were 8.6846E-2 and 8.4787E-8 psi^{-1} respectively. For the Palmer-Mansoori model the values for 'a' and 'b' were 12.609E-2 psi^{-1} and 15.346E-8 psi^{-1} respectively. By combining the two previous equations, an expression for a variable strain factor (S_f) was obtained that when multiplied to the Langmuir strain constant, S_{max}, improves both models' ability to match the actual permeability data:

$$S_f = \frac{p_{ob}}{p_p}\left[a + b\left(\frac{p_L}{S_{max} V_r^{\,2} \sqrt{\gamma}}\right)\right]. \quad \text{(6-37)}$$

Figure 6.17 shows the output of the Palmer-Mansoori model and the Shi-Durucan model when the variable strain factor is applied to the original unconstrained strain data. Compared to the models' results shown in Figure 6.15, the results when the variable strain factor is applied (Figure 6.17) are much better for all coals and gases.

6.8.1 Shape of the Modified Strain Data Curves

Figure 6.18 shows the comparison between the original strain curves and the modified strain curves for the Anderson and Gilson coals. With only one exception, the modified strain curves in Figure 6.18 reflect that strain needed to be depressed in relation to the originally measured data at larger pore pressures using unconstrained samples in order to match the measured permeability data. In addition, the modified strain curves for both the Palmer-Mansoori model and the Shi-Durucan model are very similar to each other in all but one or two cases.

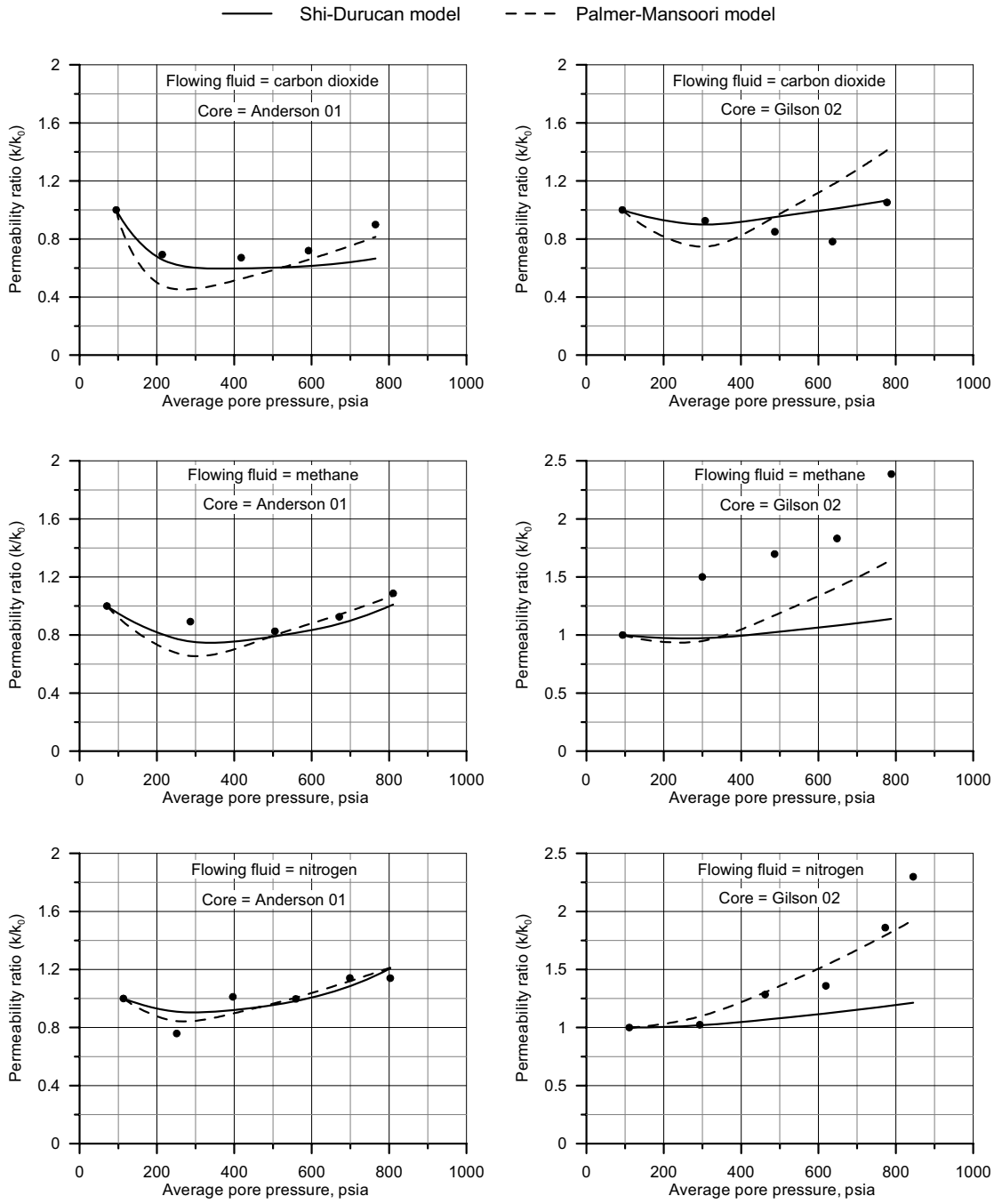

Figure 6.17. Plots showing refined model comparisons to permeability data. Confining pressure was 1000 psia and temperature was 80° F.

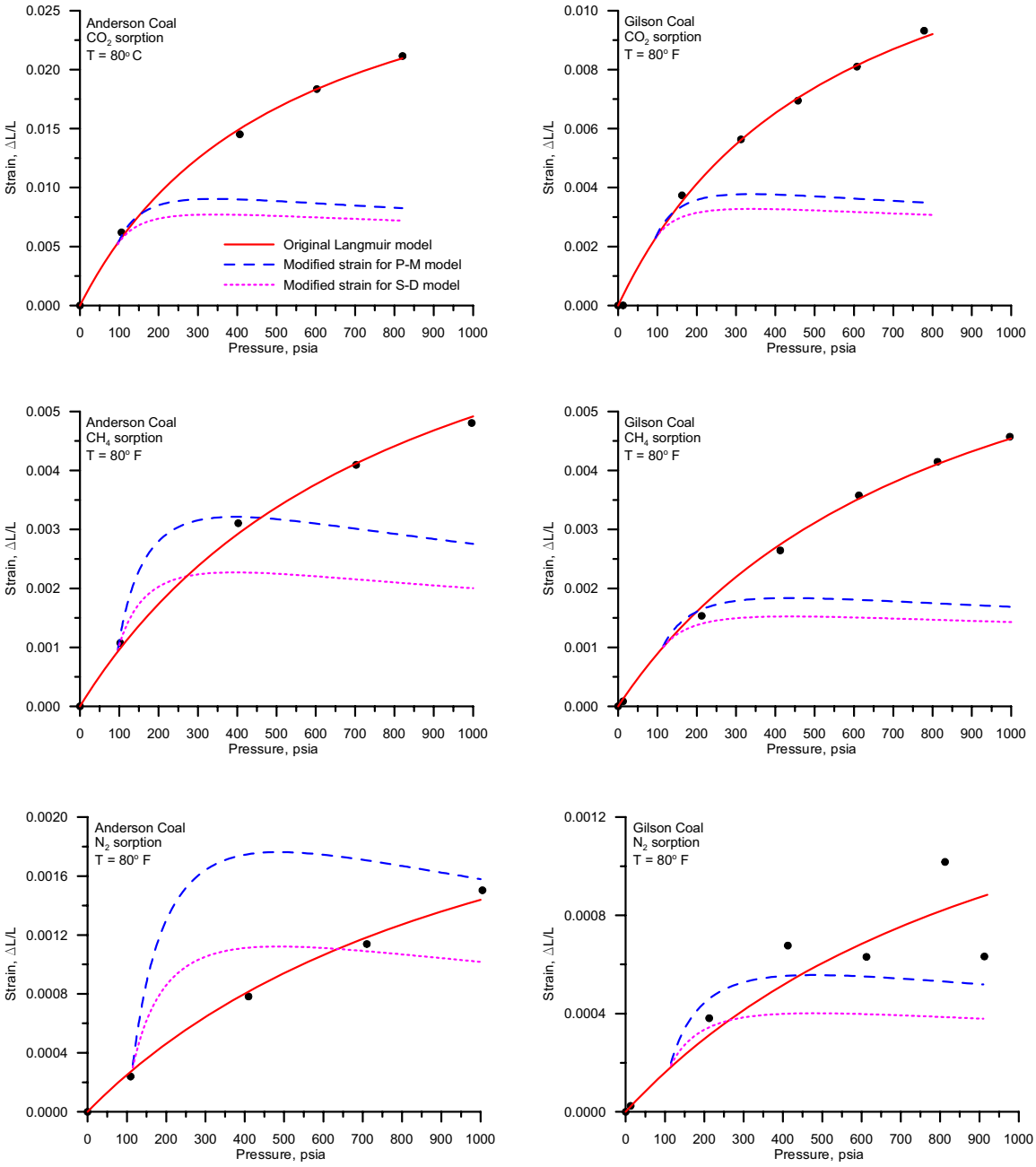

Figure 6.18. Comparison of modified strain curves with original Langmuir strain curves. Measured strain data are indicated by solid circles. P-M refers to the Palmer-Mansoori model and S-D refers to the Shi-Durucan model.

6.8.2 Testing the Strain Modification.

To test the application of the strain modification to other gases, permeability was measured for the same two coal cores (Anderson 01 and Gilson 02) using the gas mixture described in Section 5.2 . The sorption-induced strain isotherms shown in Figure 5.10 were used to calculate the Langmuir strain constants shown in Table 6.2.

Table 6.2. Langmuir constants for sorption-induced strain curves for a gas mixture at 80° F.

Gas	Coal	Constants for Strain Curves		R^2 value for curve fit
		Normalized S_{max}	Average p_L, psia	
51% N_2 – 49% CO_2	Anderson	0.01766	306.27	0.9952
	Gilson	0.00844		0.9985

The permeability data for each core were collected in the same manner as the previous permeability experiments with the exception of the composition of the gas flowing through the cores. The same gas mixture that was used in the strain experiments was employed for the permeability tests. Figure 6.19 shows the generated permeability data along with the permeability models with and without the application of the variable strain factor for these two cores.

Incorporating the variable strain factor to both of the models greatly improved the capability to fit the permeability data for the Anderson 01 core. For the Gilson 02 core, the results were not as striking, but still did improve the fit of the measured data. These results tend to validate the assumption that unconstrained strain data need to be adjusted in order to be used to fit actual laboratory-generated permeability data.

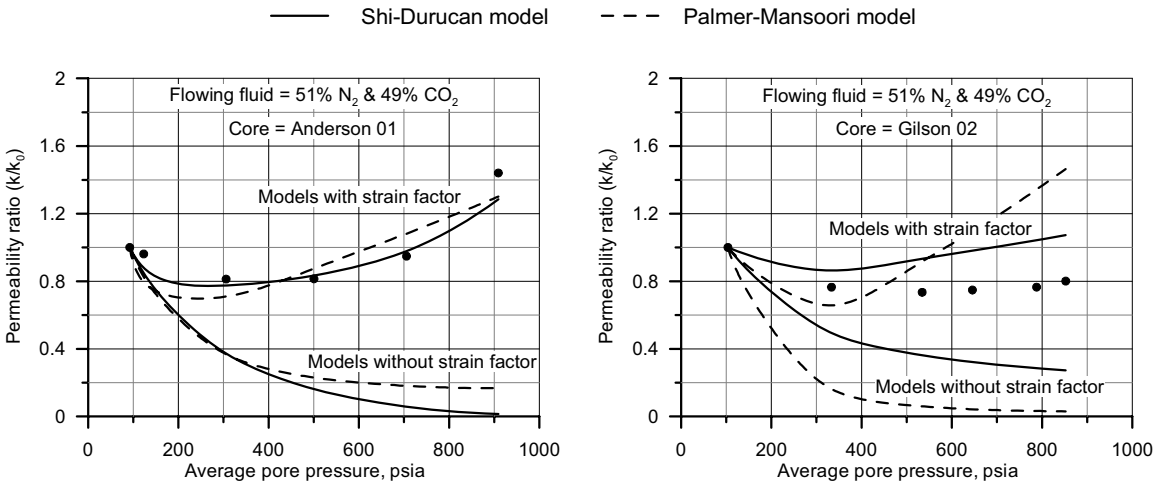

Figure 6.19. Plots showing permeability model comparisons for a gas mixture flowing through two coal cores. Confining pressure was 1000 psia and temperature was 80° F.

CHAPTER 7. CONCLUSIONS

This chapter summarizes the findings, conclusions, and recommendations for future work noted in the previous chapters.

7.1 Findings and Conclusions

An optical method to measure the linear strain in coal induced by the sorption of gases was developed that greatly reduces the amount of time required for sample equilibration. The total time needed to construct a strain-pressure plot for a given temperature has been reduced from over 100 days with traditional strain gauges to less than 10 days using this new technique.

Unconfined strain was measured for coal samples subjected to CO_2, CH_4, and N_2 at pressures up to 1000 psia.

Time-dependence of sorption-induced strain (at constant pressure and temperature) can be modeled using a Langmuir-type equation, which allows the extrapolation of strain to infinite time.

During sorption-induced strain measurements, as the ratio of the change in sorption pressure to total pressure ($\Delta p/p$) increased, the equilibration time generally increased for the samples tested.

Sorption-induced strain at equilibrium is best modeled using a Langmuir-type equation with pressure constant p_L and maximum strain constant S_{max} and is not a linear function of gas pressure.

When comparing the strain curves for a given coal sample caused by the sorption of different gases, CO_2 adsorption caused the highest strain, followed by CH_4, and N_2 adsorption caused the lowest strain.

Coal samples adsorbing gases (such as CO_2) that induce large strains approach their maximum strain at lower pressures than when adsorbing gases (such as N_2) that induce small strains. In other words, the curvature of the strain curve decreased as total strain decreased.

Sorption-induced strain decreased as coal rank increased for all gases tested. The CO_2 and N_2 strains were about twice as large in the subbituminous coal as the high-volatile bituminous coal, while CH_4 strain was only 1.1 times larger in the subbituminous coal than the high-volatile bituminous coal.

The CO_2/CH_4 strain ratio decreased with an increase in coal rank, which implies that there will be more permeability reduction in lower rank coals during CO_2 injection for CO_2-ECBM or CO_2 sequestration operations.

Simple extended Langmuir theory can be used to model coal strain induced by the adsorption of a multi-component gas mixture; however, the inclusion of the adsorbate interaction energies significantly improves the modeling of strain induced by the adsorption of gas mixtures.

Permeability was measured for coal samples subjected to CO_2, CH_4, and N_2 at pore pressures up to 800 psia.

With confining pressure fixed at 1000 psi, permeability, in some cases, decreased and then increased with increasing pore pressure. In other cases, the permeability simply increased with increasing pore pressure.

Correlating changes in permeability with unconfined strain measurements proved difficult.

Although there are many permeability-change models available for use in predicting coal permeability behavior as a function of pore pressure, some are too simplistic to be of real value in reservoir simulation.

All three permeability models considered in this work significantly overestimated the decrease in permeability as pore pressure was increased.

For mixed-gas fluids, very little difference was found in predicted permeability between models including the interaction energy constants and the models that neglect them. Therefore, there may be no need to include the interaction energies when modeling permeability changes caused by mixed-gas adsorption or desorption.

Although the models do no appear to benefit from the inclusion of interaction energies associated with sorption of mixed gases, neither the Shi-Durucan model nor the Palmer-Mansoori accurately predicts mixed-gas permeability changes in coal based on pure gas sorption constants alone.

A correction factor was developed that is a function of pore pressure, overburden pressure, gas type, and coal rank that when multiplied to the original strain data, improves both the Palmer-Mansoori model and the Shi-Durucan model.

A test of the application of the correction factor to sorption-induced changes in permeability appears to validate its application to the strain data.

Adjusting unconfined sorption-induced strain measurements for incorporation into permeability models to account for the confining stress associated with laboratory (and presumably field) conditions.

Corrected sorption-induced strain curves were generally lower as sorption pressure increased when compared to actual strain measured on unconstrained samples.

7.2 Recommendations for Future Work

Initial tests showed that sandstone was not inert with respect to swelling in the presence of pressurized carbon dioxide. Further testing should be done to elucidate this phenomenon for it may have application to CO_2 injection into deep saline aquifers for CO_2 sequestration.

Temperature effects on sorption-induced strain measurements were specifically excluded from this work, but could be easily studied using the optical strain measurement apparatus developed for this work.

Other researchers have shown that coal is probably isotropic at least in small samples. Experiments could be easily designed to study the isotropic nature of coals by carefully cutting samples in the x, y, and z directions to verify that assumption.

There are differences of opinion regarding the relationship between adsorption isotherms and sorption-induced strain isotherms. More work should be done to relate these two measurements.

There have been many studies showing the effect of moisture on adsorption isotherms in coal, but none have been found that investigates the effect of moisture on strain isotherms.

Further experimentation should be done to confirm the finding that during sorption-induced strain measurements, as the ratio of the change in sorption pressure to total pressure ($\Delta p/p$) increased, the equilibration time generally increased for the samples tested.

Because sorption-induced strain is important to modeling reservoir performance during coalbed CO_2 sequestration, CO_2-ECBM, as well as CBM production by pressure depletion, more strain measurements are needed for a wide variety of coals and under different conditions.

Although the operation of the strain measurement apparatus was fairly straightforward, there was still an element of operator skill or art involved with the collection of the data. Improvements to the apparatus should be done to automate the detection of the coal edges and avoid the potential for operator error.

The value for the Langmuir pressure constant (p_L) appeared to be independent of coal rank. Further testing should be done to affirm this observation.

Data in this work show that strain decreases with an increase in coal rank; however, other researchers have reported opposite results. More work should be done to elucidate these differences.

Measured strain data in this work show that as coal rank increased the ratio of the CO_2-induced strain to the CH_4-induced strain decreased. This finding supports the work

of other researchers, but contradicts the work of others. More data need to be collected in order to validate this finding.

LIST OF SYMBOLS

a = constant used in variable strain factor equation, dimensionless

A = cross sectional area of core, cm^2

b = constant used in variable strain factor equation, psi^{-1}

C_f = fracture compressibility, psi^{-1}

$c_m V_m$ = equivalent to the Langmuir strain constant, S_{max}, dimensionless

C_0 = initial fracture compressibility, psi^{-1}

E = Young's modulus, psi

E_{ij} = momentum transfer efficiency between two gases i and j

f_{mix} = fluidity of a gas mixture, cp^{-1}

K = bulk modulus, psi

k = permeability, mD

k_0 = initial permeability, mD

L = length, cm

ΔL = change in length, cm

M = constrained axial modulus, psi

M_i = molecular weight of gas mixture components, g/mole

n = number of moles, dimensionless

p = pressure, psia

Δp = differential pressure across core, psia

p_L = Langmuir pressure constant, psia

p_0 = initial pressure, psia

p_{ob} = overburden pressure, psia

p_p = pore pressure, psia

p_{pore} = pore pressure, psia

q_{avg} = average flow rate through core, mL/s

R = universal gas constant, psi-mL/moles/°R

R_o = % vitrinite reflectance

R^2 = coefficient of determination, dimensionless

S = strain, dimensionless

s = constant for linearly elastic materials (equal to unity for coal)

S_f = variable strain factor, dimensionless

S_L = linear or longitudinal strain, dimensionless

S_t = Langmuir strain-time constant; strain at infinite time, dimensionless

S_{max} = Langmuir linear strain constant; strain at infinite pressure, dimensionless

S_{mix} = strain induced by sorption of a gas mixture, dimensionless

S_V = volumetric strain, dimensionless

t = time, sec or hr

T = temperature, °F or °R

t_L = Langmuir time constant, sec or hr

V = volume, mL

V_{sc} = volume at standard conditions, mL

V_L = Langmuir volume, mL

ΔV = change in volume, mL

V_r = vitrinite reflectance, %

x = Eq (26) and Eq (27): mole fractions of components in gas mixture, dimensionless

X = interim strain factor, dimensionless

y = Eq (14): measured strain data, dimensionless

Eq (15): mole fractions of components in gas mixture, dimensionless

Eq (27): momentum fraction of each gas component, dimensionless

y* = calculated strain data, dimensionless

ybar = the average of the measured strain data, dimensionless

Z = compressibility factor

α = fracture compressibility change rate, psi^{-1}

γ = gas gravity, dimensionless

ε = volumetric strain, dimensionless

η = interaction energy of gas adsorbate, dimensionless

μ = viscosity

ν = Poisson's ratio, dimensionless

σ = effective or net stress, psi

σ_t = total stress, psi

σ_0 = initial net stress, psi

ϕ = porosity, dimensionless

ϕ_0 = initial porosity, dimensionless

REFERENCES CITED

1. Nelson, C.R., 1999: "Effects of Coalbed Reservoir Property Analysis Methods on Gas-In-Place Estimates," paper SPE 57443, presented at the SPE Eastern Regional Meeting, Charleston, WV (21-22 October 1999).

2. Stevens, S.H., D. Spector, and P. Riemer, 1998: "Enhanced Coalbed Methane Recovery Using CO_2 Injection: Worldwide Resource and CO_2 Sequestration Potential," paper SPE 48881, presented at the SPE International Conference and Exhibition in China, Beijing, China (2-6 November 1998).

3. Tennesee Valley Authority (TVA) – Facts on Fossil Fuel Power Generation found at the following internet location: www.tva.gov/power/fossil.htm.

4. Puri, R. and D. Yee, 1990: "Enhanced Coalbed Methane Recovery," paper SPE 20732, presented at the SPE 65th Annual Technical Conference, New Orleans, LA (September 24-26, 1990).

5. Berkowitz, N.: *Coal Science and Technology 7 – The Chemistry of Coal*, Elsevier Science (1985) 86.

6. Berkowitz, N.: *An Introduction to Coal Technology – Second Edition*, Academic Press, Inc. (1994) 75-76.

7. Rice, D.D., 1993: "Composition and Origins of Coalbed Gas," *Hydrocarbons from Coal, American Association of Petroleum Geologists Studies in Geology*, **38**, B.E. Law and D.D. Rice, eds (1993) 159-184.

8. Nelson, C.R., D.G. Hill, and T.J. Pratt, 2000: "Properties of Paleocene Fort Union Formation Canyon Seam Coal at the Triton Federal Coalbed Methane Well, Campbell County, Wyoming," paper SPE 59786, presented at the SPE/CERI Gas Technology Symposium, Calgary, Alberta, Canada (3-5 April 2000).

9. Gamson, P., B. Beamish, and D. Johnson, 1996: "Coal microstructure and secondary mineralization: their effect on methane recovery," *Coalbed Methane and Coal Geology*, R Gayer and I. Harris (eds.) 1996, Geological Society Special Publication No. 109, 165-179.

10. Mavor, M.J., L.B. Owen, and T.J. Pratt, 1990: "Measurement and Evaluation of Coal Sorption Isotherm Data," paper SPE 20728, presented at the SPE 65th Annual Technical Conference, New Orleans, LA (September 24-26, 1990).

11. Langmuir, I., 1916: "The Constitution and Fundamental Properties of Solids and Liquids," *Journal of the American Chemical Society*, **38** (1916) 221-229.

12. COMET2 version 2.11 Users Guide (11 December 2001) Figure 4-4, p. 72.

13. Stevenson, M.D., W.V. Pinczewski, and R.A. Downey, 1993: "Economic Evaluation of Nitrogen Injection for Coalseam Gas Recovery," paper SPE 26199, presented at the SPE Gas Technology Symposium, Calgary, Alberta, Canada (28-30 June 1993).

14. Wong, S., W.D. Gunter, and M.J. Mavor, 2000: "Economics of CO_2 Sequestration in Coalbed Methane Reservoirs," paper SPE 59785, presented at the SPE/CERI Gas Technology Symposium, Calgary, Alberta, Canada (3-5 April 2000).

15. Rice, D.D., 1993: "Composition and Origins of Coalbed Gas," *Hydrocarbons from Coal, American Association of Petroleum Geologists Studies in Geology*, **38**, B.E. Law and D.D. Rice, eds (1993) 159-184.

16. Nelson C.R., D.G. Hill, and T.J. Pratt, 2000: "Properties of Paleocene Fort Union Formation Canyon Seam Coal at the Triton Federal Coalbed Methane Well, Campbell County, Wyoming," paper SPE 59786, presented at the SPE/CERI Gas Technology Symposium, Calgary, Alberta, Canada (3-5 April 2000).

17. Reeves, S. and A. Oudinot, 2004: "A Tiffany Unit N_2 - ECBM Pilot: A Reservoir Modeling Study," U.S. Department of Energy Topical Report (March 2004).

18. Liang J., K.T. Raterman, and E.P. Robertson, 2003: "A Mechanistic Model for CO_2 Sequestration in Tiffany Coal Bed Methane Field," *proc.* 2003 International Coalbed Methane Symposium, paper 0339, University of Alabama, Tuscaloosa, Alabama (5-9 May 2003).

19. Reeves, S., A. Taillefert, and L. Pekot, 2003: "The Allison Unit CO_2 – ECBM Pilot: A Reservoir Modeling Study," U. S. Department of Energy Topical Report (February 2003).

20. Mavor, M.J., W.D. Gunter, and J.R. Robinson, 2004: "Alberta Multiwell Micro-Pilot Testing for CBM Properties, Enhanced Methane Recovery and CO_2 Storage

Potential," paper SPE 90256 *proc*. 2004 SPE Annual Technical Conference and Exhibition, Houston, Texas (26-29 September 1990).

21. Zuber, M, and C. Hopkins, 1999: "Coalbed Methane Engineering Methods," *SPE Educational Services Short Course* (1999).

22. Seidle, J.P., M.W. Jeansonne, and D.J. Erickson: "Application of Matchstick Geometry to Stress Dependent Permeability in Coals," paper SPE 24361 presented at the SPE Rocky Mountain Regional Meeting, Casper, Wyoming (18-21 May 1992).

23. Palmer, I. and J. Mansoori, 1998: "How Permeability Depends on Stress and Pore Pressure in Coalbeds: A New Model," paper SPE 52607, *SPE Reservoir Evaluation & Engineering* (December 1998) 539-544.

24. Reiss, L.H., 1980: *The Reservoir Engineering Aspects of Fractured Formations*, Gulf Publishing Company (1980).

25. Harpalani, S. and G. Chen, 1995: "Estimation of Changes in Fracture Porosity of Coal with Gas Emission," *Fuel*, **74**, (1995) 1491.

26. Gray, I., 1987: "Reservoir Engineering in Coal Seams: Part 1 – The Physical Process of Gas Storage and Movement in Coal Seams," paper SPE 12514, *SPE Reservoir Engineering* (February 1987) 28-34.

27. Harpalani, S. and R.A. Schraufnagel, 1990: "Influence of Matrix Shrinkage and Compressibility on Gas Production from Coalbed Methane Reservoirs," paper SPE 20729, presented at the 1990 SPE Annual Technical Conference and Exhibition, New Orleans, Louisiana, 23-26 September.

28. Seidle, J.P. and L.G. Huitt, 1995: "Experimental Measurement of Coal Matrix Shrinkage Due to Gas Desorption and Implications for Cleat Permeability Increases," paper SPE 30010, presented at the 1995 International Meeting on Petroleum Engineering, Beijing, China (14-17 November 1995).

29. Levine, J.R., 1996: "Model study of the influence of matrix shrinkage on absolute permeability of coal bed reservoirs," *Coalbed Methane and Coal Geology*, R Gayer and I. Harris (eds.) 1996, Geological Society Special Publication No. 109, 197-212.

30. Chikatamarla, L. and M.R. Bustin, 2004: "Implications of Volumetric Swelling/Shrinkage of Coal in Sequestration of Acid Gases," paper 0435, *proc.* of the 2004 International Coalbed Methane Symposium, University of Alabama, Tuscaloosa, Alabama (May 2004).

31. Zutshi A. and S. Harpalani, 2004: "Matrix Swelling with CO_2 Injection in a CBM Reservoir and Its Impact on Permeability of Coal," paper 0425 presented at the 2004 International Coalbed Methane Symposium, University of Alabama, Tuscaloosa, Alabama (May 2004).

32. Massarotto, P., 2004: "Enhanced Coalbed Methane with Geological Sequestration of CO_2," presented at the SPE ATW Enhanced CBM Recovery and CO_2 Sequestration, Denver, CO (29 Oct 2004).

33. Law, D.H.S. 2002: "Numerical Model Comparison Study for Greenhouse Gas Sequestration in Coalbeds," presented at the COAL-SEQ I Forum, Houston, Texas, U.S.A. (14-15 March 2002).

34. "RECOPOL Workshop," *Greenhouse Issues*, Number 78 (June 2005) 5-7, www.ieagreen.org.uk.

35. Sawyer, W.K., G.W. Paul, and R.A. Schraufnagel, 1990: "Development and Application of a 3D Coalbed Simulator," paper CIM/SPE 90-119, presented at the 1990 International Technical Meeting hosted jointly by the Petroleum Society of CIM and the Society of Petroleum Engineers, Calgary, Alberta, Canada (10-13 June 1990).

36. Pekot, L.J. and S.R. Reeves, 2003: "Modeling the Effects of Matrix Shrinkage and Differential Swelling on Coalbed Methane Recovery and Carbon Sequestration," paper 0328 *proc.* 2003 International Coalbed Methane Symposium, University of Alabama, Tuscaloosa, Alabama (May 2003).

37. Palmer, I, 2004: "Permeability Changes in a CBM Reservoir During Production: an Update and Implications for CO_2 Injection," paper 0403, presented at the 2004 International Coalbed Methane Symposium, U. of Alabama, Tuscaloosa, AL, 3-7 May 2004.

38. Palmer, I, 2004: "Geomechanics and Permeability Changes," presented at the SPE ATW Enhanced CBM Recovery and CO_2 Sequestration, Denver, CO (29 Oct 2004).

39. Shi, J.Q. and S. Durucan, 2003: "Changes in Permeability of Coalbeds During Primary Recovery – Part 1: Model Formulation and Analysis," paper 0341 *proc.* at the 2003 International Coalbed Methane Symposium, University of Alabama, Tuscaloosa, Alabama (May 2003).

40. Shi, J.Q. and S. Durucan, 2003: "Changes in Permeability of Coalbeds During Primary Recovery – Part 2: Model Validation and Field Application," paper 0342 *proc.* at the 2003 International Coalbed Methane Symposium, University of Alabama, Tuscaloosa, Alabama (May 2003).

41. Berkowitz, N.: *An Introduction to Coal Technology – Second Edition*, Academic Press, Inc. (1994) 102.

42. Gash, B.W., 1991: "Measurement of 'Rock Properties' in Coal for Coalbed Methane Production," paper SPE 22909, presented at the 1991 SPE Annual Technical Conference and Exhibition, Dallas, Texas (6-9 October 1991).

43. Stricker, G.D. and M.S. Ellis, 1999: "Coal Quality and Geochemistry, Powder River Basin, Wyoming and Montana," 1999 Resource Assessment Of Selected Tertiary Coal Beds And Zones In The Northern Rocky Mountains And Great Plains Region, Part I: Powder River Basin, *in* U.S. Geological Survey Professional Paper 1625-A.

44. *Annual Review and Forecast of Utah Coal, Production and Distribution – 2003*, prepared by the Utah Energy Office, Department of Natural Resources, printed October 2004.

45. Vorres, K.S., 1990: *Users Handbook for The Argonne Premium Coal Sample Program*, www.anl.gov/PCS/report/part1.html.

46. Robertson, E.P. and R.L. Christiansen, 2004: "Optically-based Strain Measurement of Coal Swelling and Shrinkage," paper 0417 *proc.* 2004 International Coalbed Methane Symposium, University of Alabama, Tuscaloosa, Alabama (May 2004).

47. Olszewski, A.J., D.L. Luffel, J. Hawkins, M.D. Zuber, J.D. McLennan, J.F. Shatz, and R.B. Truman, 1993: "Development of Formation Evaluation Technology for Coalbed Methane Development," Final Report, No. GRI-93/0178, Gas Research Institute, Chicago, Illinois (April, 1993).

48. White, C.M., D.H. Smith, K.L. Jones, A.L. Goodman, S.A. Jikich, R.B. LaCount, S.B. DuBose, E. Ozdemir, B. I. Morsi, and K.T. Schroeder, 2005: "Sequestration of Carbon Dioxide in Coal with Enhanced Coalbed Methane Recovery – A Review," *Energy & Fuels*, **19**, 3 (May/June 2005).

49. Joubert, J.I., C.T. Grein, and D. Bienstock, 1974: "Effect of Moisture on the Methane Capacity of American Coals," *Fuel*, **53**, 3 (July 1974) 186-191.

50. Levy, J.H., S.J. Day, and J.S. Killingley, 1997: "Methane Capacities of Bowen Basin Coals Related to Coal Properties," *Fuel*, **76**, 9 (July 1997) 813-819.

51. Chikatamarla, L. and M.R. Bustin, 2003: "Sequestration Potential of Acid Gases in Western Canadian Coals," paper 0360, *proc.* of the 2003 International Coalbed Methane Symposium, University of Alabama, Tuscaloosa, Alabama (May 2003).

52. Robertson, E.P. and R.L. Christiansen, 2005: "Measurement of Sorption-Induced Strain," paper 0532 *proc*. 2005 International Coalbed Methane Symposium, University of Alabama, Tuscaloosa, Alabama (May 2005).

53. Schuyer, J., H. Dijkstra, and D.W. van Krevelen, 1954: "Chemical Structure and Properties of Coal VII – Elastic Constants," *Fuel*, **33**, No. 4 (October 1954) 409-418.

54. Berkowitz, N., 1985: *Coal Science and Technology 7 – The Chemistry of Coal*, Elsevier Science (1985) Figure 2.7, 286.

55. Pekot, L.J. and S.R. Reeves, 2002: "Modeling Coal Matrix Shrinkage and Differential Swelling with CO_2 Injection for Enhanced Coalbed Methane Recovery and Carbon Sequestration Applications," topical report, Contract No. DE-FC26-00NT40924, U.S. DOE, Washington, DC (November 2002).

56. Bustin, M., 2002: "Research Activities on CO_2, H_2S, and SO_2 Sequestration at UBC," Coal-Seq I Forum, Houston Texas, 14-15 March.

57. Reeves, S.R., 2003: "Enhanced CBM recovery, coalbed CO_2 sequestration assessed," *Oil & Gas Journal* (July 14) 49-53.

58. *Gas Separation by Adsorption Processes*, Ralph T. Yang (ed.) Imperial College Press, London (1997).

59. *Gas Separation by Adsorption Processes*, Ralph T. Yang (ed.) Imperial College Press, London (1997), Eq (3.8), p 51.

60. Robertson, E.P. and R.L. Christiansen, 2005: "Modeling Permeability in Coal Using Sorption-Induced Strain Data," paper SPE 97068, *proc*. 2005 SPE Annual Technical Conference and Exhibition, Dallas, Texas (October 2005).

61. http://webbook.nist.gov/chemistry/fluid/

62. Peress, J.: "Working with Non-Ideal Gases," www.cepmagazine.org (March 2003) 39-41.

63. T.A. Davidson, 1993: "A Simple and Accurate Method for Calculating Viscosity of Gas Mixtures," U.S. Department of the Interior, Bureau of Mines Report of Investigations RI-9456 (1993).

64. Hantush, M.S.: "Hydraulics of Wells," *Advances in Hydroscience*, V.T. Chow (ed.) Academic Press, New York City (1964) **1**, 281-432.

65. Walsh, J.B., 1981: "Effect of Pore Pressure and Confining Pressure on Fracture Permeability," *Intl. J. Rock Mech. Min. Sci. Geomech. Abstracts* (1981) **18**, 5, 429-35.

66. McKee, C.R. A.C. Bumb, and R.A. Koenig, 1988: "Stress-Dependent Permeability and Porosity of Coal and Other Geologic Formations," paper SPE 12858, *SPE Formation Evaluation* (March 1988) 81-91.

67. *Petroleum Engineering Handbook*, H.B. Bradley (ed.), third printing, Society of Petroleum Engineers, Richardson, Texas (1992) 51-2.

68. Harpalani, S. and X. Zhao, 1989: "Changes in Flow Behavior of Coal with Gas Desorption," paper SPE 19450, unsolicited manuscript (1989).

APPENDIX

Visual Basic code used to optimize the model used to fit the measured strain data.

```
Sub LangmuirTypeFit()

'--- Declare module level variables
Dim ymax As Double
Dim ymax0 As Double
Dim ymax1 As Double
Dim ymax2 As Double
Dim ymax3 As Double
Dim xval As Double
Dim xval0 As Double
Dim xval1 As Double
Dim xval2 As Double
Dim xval3 As Double
Dim row As Integer
Dim n As Integer
Dim ystar As Double
Dim deltay As Double
Dim rsqprev As Double
Dim rsq As Double
Dim rsqy As Double
Dim ybar As Double
Dim datarow As Integer
Dim nmax As Integer
Dim i As Integer
Dim xvalconst As String

' clear selected part of the output spreadsheet
    ActiveSheet.Range("e7:e9").Select
    Selection.ClearContents
    ActiveSheet.Range("A3").Select
    datarow = 3

' find beginning of data
' count data points
    Selection.End(xlDown).Select
    nmax = ActiveCell.row - datarow + 1

' place active cell at top of new data column
    ActiveSheet.Range("B3").Select

' write output header to sheet
    Cells(7, 4).Formula = "ymax ="
    Cells(8, 4).Formula = "xval ="
    Cells(9, 4).Formula = "rsq ="

' initial values:
    sumdeltay = 0
```

```
    sumbottom = 0
    row = datarow
    rsqprev = 0
    rsq = 1
    ymax0 = ActiveSheet.Range("e4").Value
    xval0 = ActiveSheet.Range("e5").Value

' Check to see if xval is or is not constant
    xvalconst = ActiveSheet.Range("f5").Value

' get sum of y values
    sumy = 0
    Do While row < datarow + nmax
        y = ActiveSheet.Cells(row, 2)
        sumy = sumy + y
        row = row + 1
    Loop
    ybar = sumy / nmax

' optimize ymax values
    ymax1 = ymax0 / 2
    xval = xval0
    If xvalconst = "False" Then
        Call Optimize_Xval(rsq, datarow, nmax, ymax1, xval, ybar, i)
    Else
        Call R_Squared_Value(datarow, nmax, ymax1, xval, ybar, rsq)
    End If
    rsqy1 = rsq

    ymax2 = ymax0
    xval = xval0
    If xvalconst = "False" Then
        Call Optimize_Xval(rsq, datarow, nmax, ymax2, xval, ybar, i)
    Else
        Call R_Squared_Value(datarow, nmax, ymax2, xval, ybar, rsq)
    End If
    rsqy2 = rsq

    ymax3 = ymax0 * 2
    xval = xval0
    If xvalconst = "False" Then
        Call Optimize_Xval(rsq, datarow, nmax, ymax3, xval, ybar, i)
    Else
        Call R_Squared_Value(datarow, nmax, ymax3, xval, ybar, rsq)
    End If
    rsqy3 = rsq

    rsqyprev = 0
    rsqy = rsqy2
    Do While Abs(rsqy - rsqyprev) > 0.000000000001
        xval = xval0
        rsqyprev = rsqy
        If rsqy3 > rsqy2 And rsqy2 > rsqy1 Then
            ymax1 = ymax2
            ymax2 = ymax3
            ymax3 = ymax3 * 2
```

```
    rsqy1 = rsqy2
    rsqy2 = rsqy3
    If xvalconst = "False" Then
        Call Optimize_Xval(rsqy, datarow, nmax, ymax3, xval, _
            ybar, i)
    Else
        Call R_Squared_Value(datarow, nmax, ymax3, xval, _
            ybar, rsqy)
    End If
    rsqy3 = rsqy
ElseIf rsqy3 < rsqy2 And rsqy2 < rsqy1 Then
    ymax3 = ymax2
    ymax2 = ymax1
    ymax1 = ymax1 / 2
    rsqy3 = rsqy2
    rsqy2 = rsqy1
    If xvalconst = "False" Then
        Call Optimize_Xval(rsqy, datarow, nmax, ymax1, xval, _
            ybar, i)
    Else
        Call R_Squared_Value(datarow, nmax, ymax1, xval, _
            ybar, rsqy)
    End If
    rsqy1 = rsqy
Else
    ydiff12 = Abs(ymax1 - ymax2)
    ydiff23 = Abs(ymax2 - ymax3)
    If ydiff12 >= ydiff23 Then
        ymax = (ymax1 + ymax2) / 2
        If xvalconst = "False" Then
            Call Optimize_Xval(rsqy, datarow, nmax, ymax, _
                xval, ybar, i)
        Else
            Call R_Squared_Value(datarow, nmax, ymax, xval, _
                ybar, rsqy)
        End If
        If rsqy > rsqy2 Then
            rsqy3 = rsqy2
            rsqy2 = rsqy
            ymax3 = ymax2
            ymax2 = ymax
        Else
            rsqy1 = rsqy
            ymax1 = ymax
        End If
    Else
        ymax = (ymax2 + ymax3) / 2
        If xvalconst = "False" Then
            Call Optimize_Xval(rsqy, datarow, nmax, ymax, _
                xval, ybar, i)
        Else
            Call R_Squared_Value(datarow, nmax, ymax, xval, _
                ybar, rsqy)
        End If
        If rsqy > rsqy2 Then
            rsqy1 = rsqy2
```

```
                    rsqy2 = rsqy
                    ymax1 = ymax2
                    ymax2 = ymax
                Else
                    rsqy3 = rsqy
                    ymax3 = ymax
                End If
            End If
        End If
    Loop
    ' write output to sheet
    Cells(7, 5).Value = ymax
    Cells(8, 5).Value = xval
    Cells(9, 5).Value = rsqy

End Sub

**********************************************

Sub Optimize_Xval(rsq As Double, datarow As Integer, nmax As Integer, _
                    ymax As Double, xval As Double, ybar As Double, _
                    i As Integer)

    Dim xval1 As Double
    Dim xval2 As Double
    Dim xval3 As Double

    'initialize vairables
    xval1 = xval / 2
    Call R_Squared_Value(datarow, nmax, ymax, xval1, ybar, rsq)
    rsq1 = rsq

    xval2 = xval
    Call R_Squared_Value(datarow, nmax, ymax, xval2, ybar, rsq)
    rsq2 = rsq

    xval3 = xval * 2
    Call R_Squared_Value(datarow, nmax, ymax, xval3, ybar, rsq)
    rsq3 = rsq

    rsqprev = 0
    xvalprev = 0
    rsq = rsq2

    Do While Abs(rsq - rsqprev) > 0.000000000001
        rsqprev = rsq
        xvalprev = xval
        If rsq3 > rsq2 And rsq2 > rsq1 Then
            xval1 = xval2
            xval2 = xval3
            xval3 = xval3 * 2
            rsq1 = rsq2
            rsq2 = rsq3
            Call R_Squared_Value(datarow, nmax, ymax, xval3, ybar, rsq)
            xval = xval3
            rsq3 = rsq
```

```
        ElseIf rsq3 < rsq2 And rsq2 < rsq1 Then
            xval3 = xval2
            xval2 = xval1
            xval1 = xval1 / 2
            rsq3 = rsq2
            rsq2 = rsq1
            Call R_Squared_Value(datarow, nmax, ymax, xval1, ybar, rsq)
            xval = xval1
            rsq1 = rsq
        Else
            xdiff12 = Abs(xval1 - xval2)
            xdiff23 = Abs(xval2 - xval3)
            If xdiff12 >= xdiff23 Then
                xval = (xval1 + xval2) / 2
                Call R_Squared_Value(datarow, nmax, ymax, xval, ybar, _
                    rsq)
                If rsq > rsq2 Then
                    rsq3 = rsq2
                    rsq2 = rsq
                    xval3 = xval2
                    xval2 = xval
                Else
                    rsq1 = rsq
                    xval1 = xval
                End If
            Else
                xval = (xval2 + xval3) / 2
                Call R_Squared_Value(datarow, nmax, ymax, xval, ybar, _
                    rsq)
                If rsq > rsq2 Then
                    rsq1 = rsq2
                    rsq2 = rsq
                    xval1 = xval2
                    xval2 = xval
                Else
                    rsq3 = rsq
                    xval3 = xval
                End If
            End If
        End If
    Loop
End Sub

***********************************************

Sub R_Squared_Value(datarow As Integer, nmax As Integer, a As Double, _
                    b As Double, ybar As Double, rsq As Double)
row = datarow
'this subrouting is based on the equations outlined in Probablility and
'Statistics for Engineers and Scientists by Jay L. Devore, p. 503-506
    SSe = 0
    SSt = 0
    Do While row < datarow + nmax
        x = ActiveSheet.Cells(row, 1)
        y = ActiveSheet.Cells(row, 2)
        'langmuir-type equation for ystar
```

```
            ystar = a * x / (b + x)
        'end equation for ystar
        SSe = (y - ystar) ^ 2 + SSe
        SSt = (y - ybar) ^ 2 + SSt
        row = row + 1
    Loop
    rsq = 1 - SSe / (SSe + SSt)
End Sub
```